

國立台灣大學工學院材料科學與工程學研究所

博士論文

Department of Materials Science and Engineering

College of Engineering

National Taiwan University

Doctoral Thesis

梯度媒體的製作、結構、磁性以及磁記錄特性探討

Study of graded-medium properties of process, structure,
magnetism, and magnetic recording

林奕宏

Yi-Hung Lin

指導教授：郭博成 博士、許仁華 博士

Advisor : Po-Cheng Kuo, Ph.D., Jen-Hwa Hsu, Ph.D.

中華民國 103 年 7 月

July 2014



國立臺灣大學博士學位論文 口試委員會審定書

論文中文題目： 梯度媒體的制作、結構、磁性以及磁記錄特性探討

論文英文題目： Study of graded-medium properties of process, structure, magnetism, and magnetic recording

本論文係林奕宏君 (D97527016) 在國立臺灣大學材料科學與工程學系、所完成之博士學位論文，於民國 103 年 06 月 26 日承下列考試委員審查通過及口試及格，特此證明

口試委員： 郭博成 郭博成
(指導教授)

許仁華 許仁華

陳勝吉 陳勝吉

孫安正 孫安正

蔡佳霖 蔡佳霖

系主任、所長 林招松 林招松 (簽名)

Abstract



Magnetic recording needs to have high remanent magnetization and high coercivity due to the effects of self-demagnetization and stray fields. Accordingly, in the past CoCrPt was used for the material of recording medium. However, because of larger thermal fluctuation and noise, it is hard to further enhance the areal density if the areal density approaches to 1 Tbit/in². *L*₁₀-FePt becomes one of the candidate materials due to the high magnetocrystalline anisotropy constant ($K_u \sim 7 \times 10^7$ erg/cm³), high saturation magnetization (~ 1140 emu/cm³), high anisotropy field (~ 116 kOe), and minimal stable grain size as small as 3 nm. Therefore, FePt is employed as the material of recording media to be studied. Such high K_u materials also makes writing difficulty resulting to develop the technology of heat-assisted magnetic recording (HAMR) in order to solve the problems of large writing field. The other way is to reduce the switching field. In the past, double-layer of exchange spring media have been used as the recording media to reduce the coercivity by a factor of 2. Our studies concentrate on graded media in order to further decrease the coercivity and maintain the thermal stability factor.

Herein, we explore the magnetic behaviors of *L*₁₀-FePt graded films three approaches: gradient-temperature (T_g), composition (C_g) and working pressure (P_g). As a result, $H_{c\perp}$ can be reduced by a factor of 2.6, 2.8, and 3.3 for the C_g -, T_g - and

P_g-L1_0 FePt layers, respectively. Both T_g - and P_g -FePt have the similar reversal behavior. On the other hand, for C_g -FePt, the magnetization increases sharply upon removal of the applied field. This increment in the magnetization is due to the presence of reversible magnetization switching arising from the non-coherent rotation. Therefore, considering to reduce the switching field and magnetic reversal, P_g -FePt film may has the best gradient performance among these three structures.

摘要



磁記錄媒體必須具有很高的殘留磁化 (M_r , remanent magnetization), 矯頑磁場 (H_c) 也要高, 才能減少自我消磁效應 (self-demagnetization) 以及雜散磁場 (stray fields) 的去磁作用。因此, 在過去使用 CoCrPt 基當作記錄媒體的材料, 但其記錄密度在接近 1 Tb/in^2 時, 將難以再提升以克服熱擾動及雜訊變大的問題。 $L1_0$ -FePt 材料由於具有高磁晶異向常數 ($\sim 7 \times 10^7 \text{ erg/cm}^3$)、大的飽和磁化量 (1140 emu/cm^3)、大的異向場 (116 kOe), 以及最小穩定的晶粒尺寸大約只有 3 nm , 所以是個很好的候選材料, 因此本研究採用 FePt 為記錄媒體研究的材料。

在記錄密度不斷提升的同時, 由於必須使用大的 K_u 材料, 也產生了資料越來越難寫入的問題, 熱輔助磁讀技術因此發展出來, 解決寫入場過高的問題。另一個辦法, 則是想辦法降低記錄媒體的翻轉場問題, 在過去的雙層 exchange spring 媒體, 可以大約降低硬磁層 H_c 的 2 倍大小, 為了再進一步降低 H_c 的值, 且不降低熱穩定因子的情況下, 我們採用多層漸變的 exchange spring 結構。

本研究之多層漸變的交互彈簧 (exchange spring) 結構主要有三種: 利用溫度高低、成分變化, 以及壓力變化, 製作出三種不同的多層漸變的交互彈簧結構。結果顯示, 成分漸變的結構將 H_c 降低了 2.6 倍; 溫度漸變將 H_c 降低大約 2.8 倍; 而壓力漸變再進一步將 H_c 降低大約 3.3 倍。溫度與壓力漸變結構具有相似的磁翻轉行為。而成分漸變結構, 在去磁過程, 由於不一致的磁旋轉 (non-coherent rotation) 產生, 會有一個大的可逆翻轉。因此, 考慮降低翻轉場及磁翻轉行為,

壓力漸變為最佳的漸變膜層結構。



Acknowledgement



六年的時間很快地過去了，首先要感謝我的指導教授許仁華及郭博成教授在學術研究上的悉心指導，打破我研究上的一些盲點，使我更容易抓住研究的主軸與方向；除了學術研究上，教授也教導我做人處事的道理，使學生獲益良多。另外要感謝其他的口試委員孫安正、陳勝吉及蔡佳霖教授的建議，使我的論文得以完成。

感謝元智大學孫安正教授及台大物理系盧勁羽技師在 TEM 上無私的幫忙及討論，找到我的論文在材料結構方面的證據。此外，要感謝明新科技大學梅瑞國教授在磁力顯微鏡、VSM 儀器量測上的幫忙外，也會跟我談論人生的大道理，使我不至於迷失方向。

感謝袁輔德學長無私的幫忙，從開始學作實驗、寫文章，到生活瑣事及做人做事道理，大小事全都包辦。另外，感謝實驗室小李在生活上的幫助，也因為有你的幫忙，使我更加能夠與老師配合要處理的事項。感謝實驗室其他成員金來、圓德及 Van-Su，因為實驗上的討論，教學相長互求進步。感謝同學趙國霖及學妹簡瑞芬，因為有你們一起討論，所以資格考才會那麼順利。感謝材料所儀器技術員，同時也是學長及學姊身分的高崇源以及李苑慈，因為有你們的幫忙，所以實驗量測才能那麼順利。

感謝我女友小香菇這麼多年來對我的幫忙，在我的人生最低潮的時候給我加油打氣，在研究方面也幫了我很多，幫忙寫程式分析數據，使我節省了很多處理

數據的時間，尤其在歐傑電子能譜儀及 FORC 的分析部分，妳是我重要的支柱。

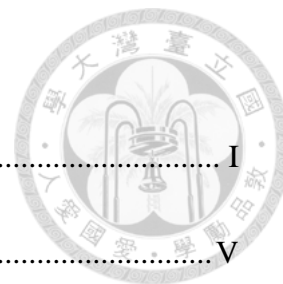
感謝小香菇媽媽黃惠珍阿姨的幫忙，教導我做人處事的道理及工作上應該注意的

事項。感謝小隻廖英君在繪圖軟體上面的指導，使我在發表文章上更加得心應

手。

最後，要感謝從小栽培我的父母親，也因為有你們的幫助及鼓勵，讓我更能夠無憂無慮地專注於學術研究上面，使我能夠順利完成博士班學業。

Contents



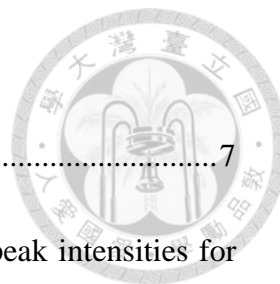
Abstract	I
Acknowledgement	V
Chapter 1	1
Chapter 2	8
2-1 Media Classification	8
2-2 Properties of FePt Perpendicular Anisotropy	9
2-3 Exchange-spring Films	10
2-4 Graded Films	13
Chapter 3	16
3-1 Flow Chart of Experiment	16
3-2 Sample Preparation.....	16
3-2-1 Equipment	16
3-2-2 Substrate Preparation.....	17
3-2-3 Target Selection.....	17
3-3 Fabrication of graded FePt	17
3-3-1 Temperature-graded FePt.....	17
3-3-2 Composition-graded FePt.....	18
3-3-3 Pressure-graded FePt.....	19

3-4 Analysis Technique	20
Chapter 4	24
4-1 Temperature-graded FePt	26
4-2 Composition-graded FePt	33
4-3 Pressure-graded FePt	40
4-4 Comparison of Three Systems.....	48
4-4(a) Structure Analysis	48
4-4(b) Microstructure Analysis.....	49
4-4(c) Magnetism Analysis	49
4-5 Summary.....	51
Chapter 5	96
References	97
Publication List	103



List of Tables

Table. 1-1 Properties of hard magnetic materials.	7
Table 4-1 Calculations for I_{001}^* and I_{002}^* —theoretical integrated peak intensities for a fully ordered of $L1_0$ -FePt films.	54
Table 4-2 Grain size diameter, nucleation field, perpendicular coercivity, and their corresponding FWHM values.	55



List of Figures

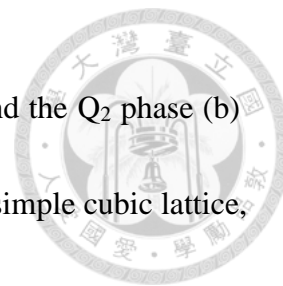


Fig. 2-1 The magnetic structure of $L1_2$ -FePt ₃ in the Q ₁ phase (a) and the Q ₂ phase (b) are shown. The gray spheres represent the Fe atoms, which form a simple cubic lattice, and the white spheres represent Pt atoms.	15
Fig. 3-1 Photograph of ultra-high vacuum deposition system.	21
Fig. 3-2 Schematic of target map.	22
Fig. 3-3 Different types of graded FePt system : experimental group (hard layer + graded layer) (a) and control group (hard layer + soft layer) (b) of temperature-graded FePt ; composition-graded FePt (c) and pressure-graded FePt (d).	23
Fig. 4-1 Atomic scattering factors of Fe (a) and Pt (b) as a function of $\sin\theta/\lambda$	56
Fig. 4-2 XRD patterns for the samples of (a) 5-nm-thick hard layer, graded films with $t_g =$ (b) 5, (c) 10, and (d) 15 nm, and hard/soft films with $t_s =$ (e) 5, (f) 10, and (g) 15 nm. (measured at National Synchrotron Radiation Research Center (NSRRC) beamline 17B in Hsinchu, Tawian)	57
Fig. 4-3 (001)-rocking curves of 5-nm-thick $L1_0$ -FePt hard layer and the FePt(T_g)-graded layers grown at different t_g : 5, 10, and 15 nm (a); and their corresponding FWHM values as a function of t_g (b).	58
Fig. 4-4 SEM images for the samples of hard layer with thickness of (a) 5 and (b) 20 nm, graded films with $t_g =$ (c) 5 and (e) 15 nm, and hard/soft films with $t_s =$ (d) 5 and (f) 15 nm. The corresponding histograms are included in the inset of each figure.	58

Fig. 4-5 In-plane and out-of-plane hysteresis loops for the samples of (a) 5-nm-thick and (b) 20-nm-thick hard layer, graded films with $t_g =$ (c) 5, (e) 10, and (g) 15 nm, and hard/soft films with $t_s =$ (d) 5, (f) 10, and (h) 15 nm.60

Fig. 4-6 $H_{c\perp}/H_{c\perp,hard}$ as a function of T_d for the FePt(P_w)-graded films.61

Fig. 4-7 Perpendicular hysteresis loops and recoil curves (measured by SQUID-VSM) of 5-nm-thick $L1_0$ -FePt (a) and T_g -FePt with $t_g = 5$ nm (b).62

Fig. 4-8 Reversible (a) and irreversible magnetization (b) as a function of the applied reversal field (H_r) for 5-nm-thick $L1_0$ -FePt and T_g -FePt with $t_g = 5$ nm.63

Fig. 4-9 Families of FORC's of T_g -FePt with $t_g = 5$ nm (a) and the corresponding FORC distribution (b).64

Fig. 4-10 MFM images for the samples of hard layer with thickness of (a) 5, (b) 10, and (c) 20 nm, graded films with $t_g =$ (d) 5, (e) 10, and (f) 15 nm, and hard/soft films with $t_s =$ (g) 5, (h) 10, and (i) 15 nm.65

Fig. 4-11 XRD patterns for the samples of hard layer with 5-nm-thick (a) and 10-nm-thick.66

Fig. 4-12 XRD patterns for the samples of graded films with $T_d =$ (a) 300, (b) 350, (c) 400 and (d) 450°C.67

Fig. 4-13 (001)-rocking curves of 5-nm-thick $L1_0$ -FePt hard layer and the FePt(C_g)-graded layers grown at different T_d : 300, 350, 400, and 450°C (a); and their

corresponding FWHM values as a function of T_d (b).68

Fig. 4-14 SEM images for the samples of hard layer with thickness of (a) 5 and (b) 20 nm, graded films with $T_d =$ (c) 300, (d) 350, (e) 400, and (f) 450°C. The corresponding histograms are included in the inset of each figure.....69

Fig. 4-15 In-plane and out-of-plane hysteresis loops for the samples of (a) 5-nm-thick and (b) 10-nm-thick hard layer, graded films with $T_d =$ (c) 300, (d) 350, and (e) 400°C.70

Fig. 4-16 Perpendicular coercivity, normalized to that of a 5nm-thick hard layer, as a function of T_d71

Fig. 4-17 Perpendicular hysteresis loops and recoil curves (measured by SQUID-VSM) of 5-nm-thick $L1_0$ -FePt (a) and C_g -FePt with $T_d = 350^\circ\text{C}$ (b).72

Fig. 4-18 Reversible (a) and irreversible magnetization (b) as a function of the applied reversal field (H_r) for 5-nm-thick $L1_0$ -FePt and C_g -FePt with $T_d = 350^\circ\text{C}$ 73

Fig. 4-19 Families of FORC's of C_g -FePt with $T_d = 350^\circ\text{C}$ (a) and the corresponding FORC distribution (b).74

Fig. 4-20 MFM images for the samples of hard layer with thickness of (a) 5, and (b) 10, graded films with $T_d =$ (c) 300, (d) 350, (e) 400, and (f) 450°C.75

Fig. 4-21 The AES depth profile of graded films with $T_d =$ (a) 300, (b) 350, (c) and 400°C. The vertical lines are the layer boundaries between each layer.76

Fig. 4-22 K_u as a function of P_w for the MgO/FePt films.	77
Fig. 4-23 XRD patterns of 5nm-thick $L1_0$ -FePt hard layer and the FePt(P_g)-graded layers grown at different T_d : 300, 350, and 400°C (a); and their corresponding (001)-rocking curve (b) and FWHM values as a function of T_d (c).	78
Fig. 4-24 SEM images of $L1_0$ -FePt hard layer with two different thicknesses: (a) 5 nm (b) 10 nm and the FePt(P_g)-graded structures grown at different T_d : 300 (c), 350 (d), 400 (e) and 450°C (f). The corresponding histograms are included in the inset of each figure.	79
Fig. 4-25 Cross-sectional TEM images of (a) 5nm $L1_0$ -FePt hard layer, and (b) the magnified image from FePt/MgO interface in Fig. 6(a), the FePt(P_g)-graded films grown at different T_d : (c) 350 and (d) 450°C	80
Fig. 4-26 In-plane and out-of-plane hysteresis loops for the samples of 5-nm thick FePt hard layer (a), and the FePt(P_g)-graded films grown at different T_d : 300 (b), 350 (c), 400°C (d).	81
Fig. 4-27 $H_{c\perp}/H_{c\perp,hard}$ as a function of T_d for the FePt(P_g)-graded films.	82
Fig. 4-28 Perpendicular hysteresis loops and recoil curves (measured by SQUID-VSM) of 5-nm-thick $L1_0$ -FePt (a) and P_g -FePt with $T_d = 350^\circ\text{C}$ (b).	83
Fig. 4-29 Reversible (a) and irreversible magnetization (b) as a function of the applied reversal field (H_r) for 5-nm-thick $L1_0$ -FePt and P_g -FePt with $T_d = 350^\circ\text{C}$	84

Fig. 4-30 Families of FORC's of P_g -FePt with $T_d = 350^\circ\text{C}$ (a) and the corresponding FORC distribution (b).....85

Fig. 4-31 XRD patterns for the samples of (a) 5-nm-thick hard layer, graded films of T_g -FePt with $t_g = 5\text{ nm}$ (b), C_g -FePt deposited at $T_d = 350^\circ\text{C}$ (c), and P_g -FePt deposited at $T_d = 350^\circ\text{C}$ (d).....86

Fig. 4-32 (001)-rocking curves of 5-nm-thick $L1_0$ -FePt hard layer and the T_g -FePt grown at t_g : 5nm, C_g - and P_g -FePt grown at $T_d = 350^\circ\text{C}$ (a); and their corresponding FWHM values as a function of t_g (b).....87

Fig. 4-33 SEM images for the samples of hard layer with thickness of (a) 5 nm, graded films of T_g -FePt with $t_g = 5\text{ nm}$ (b), C_g -FePt deposited at $T_d = 350^\circ\text{C}$ (c), and P_g -FePt deposited at $T_d = 350^\circ\text{C}$ (d). The corresponding histograms are included in the inset of each figure.....88

Fig. 4-34 Grain size distribution of $L1_0$ -FePt: 5nm (a), 10nm (b), 20nm (c); temperature graded FePt: $t_g = 5\text{ nm}$ (d), 10nm (e), 15nm (f); composition graded FePt: $T_d = 300^\circ\text{C}$ (g), 350°C (h); pressure graded FePt: $T_d = 300^\circ\text{C}$ (i), 350°C (j), 400°C (k).....89

Fig. 4-35 Grain size distribution of island-like structure: $L1_0$ -FePt, temperature graded FePt (T_g), composition graded FePt (C_g), and pressure graded FePt (P_g).....90

Fig. 4-36 Out-of-plane hysteresis loops for the $L1_0$ -FePt and three graded FePt

structures, with an insert shows their corresponding in-plane hysteresis loops.91

Fig. 4-37 Perpendicular coercivity as a function of T_d (C_g and P_g).92

Fig. 4-38 Perpendicular hysteresis loops and recoil curves (measured by

SQUID-VSM) of 5-nm-thick $L1_0$ -FePt (a), C_g -FePt (b), T_g -FePt (c), and P_g -FePt (d).

The recoil curves were measured along the demagnetizing portion from $H = -H_{\max}$

to $H = 0$ and back to $H = -H_{\max}$93

Fig. 4-39 Reversible (a) and irreversible magnetization (b) as a function of the applied

reversal field (H_r) for $L1_0$ -FePt, C_g -FePt, T_g -FePt, and P_g -FePt.94

Fig. 4-40 FORC distribution of T_g -FePt (a), C_g -FePt (b), and P_g -FePt (c).95

Chapter 1

Introduction

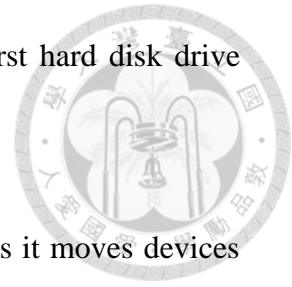


Nowadays, data storage devices are widely employed in consumer electronic products, such as smart phones, digital cameras, computers, and so on. Hard disk drives (HDDs) have been traditionally used in computers every day. They become the main storage device in daily work.

Magnetic recording is to store data on a magnetized medium by using magnetic material and is a form of non-volatile memory. The information is accessed using one or more read/write heads. Its history was first to record data on a wire, then subsequently on a tape and a disk, for the contents such as audio, video, and digital signals [\[1\]](#).

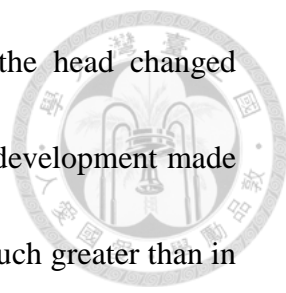
The first magnetic recorder was invented by Valdemar Poulsen in 1898 and publicly demonstrated in Paris Exposition of 1900. Poulsen's device recorded a signal on a wire wrapped around a drum. Magnetic tape was invented for sound recording by Fritz Pfleumer in 1928 in Germany, based on the invention of magnetic wire recording by Valdemar Poulsen in 1898. Pfleumer's invention made use of ferric oxide (Fe_2O_3) powder coating on a long strip of paper. This invention was further developed by the German electronics company AEG and BASF, the manufacturer of recording machines and the manufacturer of the tape respectively [\[2\]](#). However, reading

recorded analog signals had been slow and difficult before the first hard disk drive invented by IBM in 1956.



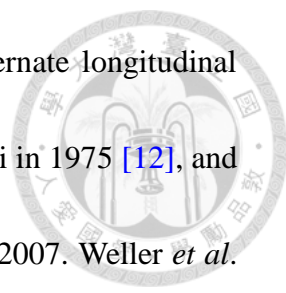
Information is written to and read from the storage medium as it moves devices called read-and-write heads that operate very close to the magnetic surface (often tens of nanometers) with very high velocity. The read-and-write head is used to quickly detect and immediately modify the magnetization of the material under it. Accordingly, the roughness of magnetic surface is very important in writing process. Magnetic head will be crashed or data will be lost if there are some particles on magnetic surface [3].

Recording density is a very important issue for medium. In older HDD designs the regions were oriented horizontally and parallel to the disk surface. However, about in the beginning of 2005, the orientation was changed to perpendicular to allow for closer magnetic domain spacing. For reliable storage of data, the recording material needs to resist self-demagnetization, which occurs when the magnetic domains repel each other. Magnetic domains written too densely together to a weakly magnetizable material will degrade over time due to rotation of the magnetic moment or rotation of more domains to cancel out these forces. The domains rotate sideways to a halfway position that weakens the readability of the domain and relieves the magnetic stresses [4]. IBM has proposed the increased areal density up to 1 GB/in² by using



magnetoresistance (MR) read head; the electrical resistance of the head changed according to the strength of the magnetism from the platter. Later development made use of spintronics; in read heads, the magnetoresistive effect was much greater than in earlier types, and was dubbed "giant" magnetoresistance (GMR). Recording density can further increased to 100 GB/in². Although recording density reached to 100 GB/in², it has much difficult to increase by using longitudinal recording due to the large demagnetizing field and super-paramagnetic effect. To avoid thermal instabilities, a minimal stability ratio of stored magnetic energy, $K_u V$, to thermal energy, $k_B T$, $K_u V / k_B T \cong 50-70$ [5-8], is required. Where k_B , T , K_u , and V are the Boltzmann constant, measuring temperature, anisotropy energy constant, and switching volume, respectively. Films of $L1_0$ -FePt were identified as one of the promising candidates for next-generation media with recording density exceeding 1 Tbit/in², owing to their large magnetocrystalline anisotropy, K_u (5×10^6 J/m³), as shown in Table 1-1 [9]. However, this high K_u material poses writing difficulty because of unfavorable increase in coercivity (H_c). Moreover, the strength of strong inter-grain coupling or the distribution of large grain size increases noise. It is very hard to have properties of low noise, good writability and high thermal stability at the same time. Consequently, it is important to compromised properties.

In order to overcome superparamagnetic effect and further increased areal



density, perpendicular recording is a technology considered to alternate longitudinal recording [10, 11]. Perpendicular recording was invented by Iwasaki in 1975 [12], and first shipped in 2005. This technology was used in many HDDs in 2007. Weller *et al.* have calculated that FePt could be thermally stable, even for grain size as small as 3 nm [13]. Suppose that it is possible to make such small grains and information could be well written on these materials, the areal density that can be achieved with FePt could easily surpass 1 Tbits/in.² [14].

Nowadays, the recording density of commercial HDD with 3.5 inch is 500 Gbits/in² [15]. Given an areal density of 620 Gbits/in², current available 3.5-in hard drives have the maximum capacity of 3TB. Laptop drives, or 2.5-in drives, top out at 750GB or roughly 500 Gbits/in² [16]. In 2012, Seagate has demonstrated the first terabit-per-square-inch hard drive, almost doubling the areal density found in modern hard drives. Initially this will result in 6TB 3.5-inch desktop drives and 2TB 2.5-inch laptop drives, but eventually Seagate is promising up to 60TB and 20TB respectively. To achieve such a huge leap in density, Seagate had to use a technology called heat-assisted magnetic recording (HAMR). In 2013, WD was announced the maximum areal density of about 750 Gbits/in² but HAMR researchers expect to reach 4 Tbits/in². In order to reach the areal density of 1Tbits/in², for square grains, the side length needs to be smaller than 25.4 nm, and for circular grains, the radius needs to be

smaller than 14.43 nm. A variety of different proposals for the other media have been made, with the aim of increasing areal density and reducing noise, e.g. granular recording media and percolated media [17, 18].



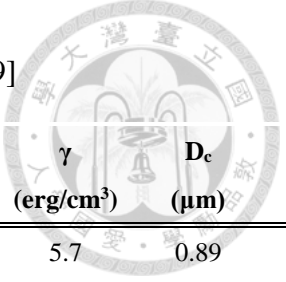
The CoCr alloy was the original media proposed by Iwasaki *et al.* in the late 1970s [19]. Since then, modifications of Co alloys such as CoCrPt, CoCrTa, CoCrNb, CoCrPtNb, and CoCrPtB were used as the recording layer materials for 20 years [20-27]. As the areal density increases beyond 500 or 600 Gbits/in², the recording media based on CoCr could face a thermal instability problem. Therefore, alternative materials or methods of recording schemes are needed to move the magnetic recording industry forward. One such material that has the potential to support high-density perpendicular recording is highly anisotropic FePt.

Films of $L1_0$ -FePt were identified as one of the promising candidates for next-generation media with recording density exceeding 1 Tbit/in², due to their large magnetocrystalline anisotropy, K_u . However, this high K_u material poses writing difficulty because of unfavorable increase in coercivity (H_c). Decreasing the H_c values without compromising the thermal stability of FePt films has been considered as one of the major challenges for recording media. During the recent years, these issues have been addressed and resolved by generating exchange-spring media and graded-media structures of $L1_0$ -FePt films. In consequence, in this research we

propose graded $L1_0$ -FePt(001) films processed by gradient temperature, composition, and working pressures.



Table. 1-1 Properties of hard magnetic materials. [9]



alloy system	material	K_u (10^7erg/cm^3)	M_s (emu/cm^3)	H_k (kOe)	T_c (K)	δw (\AA)	γ (erg/cm^3)	D_c (μm)	D_p (nm)
Co-alloys	CoPtCr	0.2	298	13.7	--	222	5.7	0.89	10.4
	Co	0.45	1400	6.4	1404	148	8.5	0.06	8.0
	Co ₃ Pt	2.0	1100	36	--	70	18	0.21	4.8
L1₀ Phase	FePd	1.8	1100	33	760	75	17	0.20	5.0
	FePt	6.6-10	1140	116	750	39	32	0.34	3.3-2.8
	CoPt	4.9	800	123	840	45	28	0.61	3.6
	MnAl	1.7	560	69	650	77	16	0.71	5.1
Rare-earth	Fe ₁₄ Nd ₂ B	4.6	1270	73	585	46	27	0.23	3.7
Transition metals	SmCo ₅	11-20	910	240-400	1000	22-30	42-57	0.71-0.96	2.7-2.2

- Anisotropy field: $H_k = 2K_u/M_s$
- Domain wall width: $\delta_w = \pi (A/K_u)^{1/2}$
- Domain wall energy: $\gamma_w \cong 4 (A/K_u)^{1/2}$
- Single particle domain size: $D_c = 1.4 \gamma_w / M_s^2$
- Exchange couple constant: $A = 10^{-6} \text{ erg/cm}$
- Minimal stable grain size: $D_p = (60k_B T/K_u)^{1/3}$ ($\tau = 10 \text{ years}$)

Chapter 2

Background



2-1 Media Classification

In order to achieve a narrower bit boundary and high recording density, it is essential to reduce the grain size and to reduce the exchange and magnetostatic interaction between the grains. For longitudinal recording, it is hard to reach 100 Gbit/in². However, it is easy for perpendicular recording to accomplish such density due to the lower demagnetization field [28].

In order to increase the areal density, small grain size is a necessary requirement. However, grain size cannot decrease any more to resist the thermal fluctuation, data will be erased due to superparamagnetic effect. As shown in Table 1-1, films of *L*₁₀-FePt were identified as one of the promising candidates for next-generation media due to the stable grain size as small as 2.8-3.3 nm. As forementioned in chapter 1, signal-to-noise ratio (SNR), thermal stability, and writability is the trilemma of magnetic recording. As the result, it is necessary to select the compromising properties. The expense of using high *K*_u material is the increased coercivity (*H*_c). Consequently, reducing the switching field becomes one of the important topic. Several solutions have been accomplished by different methods.

a. Tilted recording media [14]

Suppose the anisotropy easy axis is tilted with respect to the applied field direction, then the effective writing field need to switch the magnetization would be lower. When easy axis tilts 45° from the film direction, switching field is the lowest condition.

b. Heat assisted magnetic recording (HAMR) media [\[29\]](#)

HAMR is a technology that magnetically records data on high-stability media using laser thermal assistance to first heat the material at Curie temperature. Under Curie temperature, the coercivity of media material would be reduced obviously.

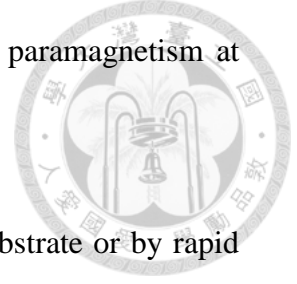
c. Exchange spring media

As discussed earlier, writability will be a serious problem for media with high anisotropy. To overcome this problem, exchange-couple composite of double layer and multilayer graded media was proposed and discussed in sections 2-3 and 2-4. Both in this two media, a soft magnetic grain and a hard magnetic grain are coupled to each other.

2-2 Properties of FePt Perpendicular Anisotropy

The equilibrium phases of Fe-Pt are rather complex. There are three different order phase in Fe-Pt system: $L1_0$ -FePt (face-centered tetragonal structure, fct), $L1_2$ -Fe₃Pt (face-centered cubic, fcc), and $L1_2$ -FePt₃, as shown in [Fig. 2-1 \[31\]](#). $L1_0$ -FePt and $L1_2$ -Fe₃Pt is ferromagnetic material at room temperature; $L1_2$ -FePt₃ is

antiferromagnetism below Néel temperature ($T_N = 160\text{K}$), and is paramagnetism at room temperature.



Perpendicular anisotropy can enhance by using MgO(100) substrate or by rapid thermal annealing. This difference can be explained as followings. For the first method, large lattice mismatch between FePt and MgO enhanced the FePt(001) texture. For the second method, films of FePt generate tensile stress along film direction, which result in the enlarged a-axis and compressive c-axis. Consequently, it is to promote the order parameter and perpendicular anisotropy at the same time.

2-3 Exchange-spring Films

The exchange-spring concept was firstly proposed by E. F. Kneller and R. Hawing in 1991 while the purpose was to enhance the product value of (BH) [32]. Combining the properties of hard and soft magnetic material, the purpose is to decrease the switching field. For applications, hard material provides high coercivity and soft material provides high magnetization.

Victora and Shen proposed exchange-couple composite media in 2005. Coupling with hard and soft magnetic layer reduces the switching field during the writing process. The switching mechanism is explained as followings [33, 34]. At a large field, all the magnetic moments are directed toward the saturation magnetization. When the field is decreased/increased to the nucleation field of the top soft layer, small reverse

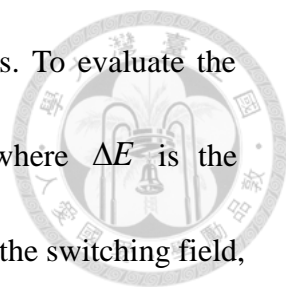
domains are nucleated. Subsequently, the magnetization reversal in the graded part is induced by the propagation of anti-parallel domain. So the magnetic moments of softest layer start to depart from the easy axis with reduction in applied field. The switching of the upper part of the soft layer occurs at the applied field close to the soft layer anisotropy field. The domain wall is then pinned near the hard/soft interface with a pinned field (H_p). As the field is further increased the domain wall in the soft layer is compressed and it penetrates more and more into the hard layer. Further increasing the applied field leads in the domain wall suddenly depinning from the hard/soft interface and immediately propagating through the entire hard layer [35].

Generally speaking, high thermal stability factor ($K_u V^*/k_B T$) is requirement for magnetic grain to bear the thermal fluctuation. Eventually, large grains also have large thermal stability as described as the following equation:

$$\tau = \frac{1}{c} \exp\left(\frac{K_u V^*}{k_B T}\right) \quad (2-1)$$

Where τ , K_u , V^* , k_B , $K_u V^*$, $k_B T$ are the relaxation time, anisotropy constant, switching volume, Boltzmann constant (1.38×10^{-16} erg/K), energy barrier, and thermal energy, respectively. It is superparamagnetism as $K_u V^*/k_B T = 1$; $\tau = 1$ minute, 7.5 years, 109 years as $K_u V^*/k_B T = 25, 40, 60$, respectively. Generally speaking, the required value of $K_u V^*/k_B T$ is at least 50 [5-8].

For comparison of ECC media and conventional media, decreasing the switching

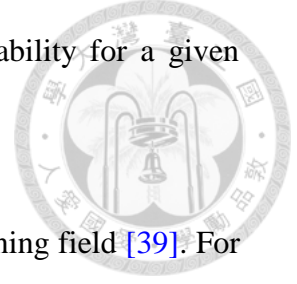


field and maintaining its thermal stability is one of the key points. To evaluate the merit, a gain factor was defined as $\xi = 2\Delta E / (M_s \cdot H_{sw} \cdot V)$, where ΔE is the thermal energy barrier, M_s is the saturation magnetization, H_{sw} is the switching field, and V is the activation volume. For conventional media, ξ is supposed to be 1, and for ECC media, ξ should be larger than 1, because the ECC media is more switchable than the conventional media with the same thermal stability. According to the two-spin model, the limit of the ξ for bilayer ECC media is 2. For graded media, ξ may further increase up to 4 [36].

If experimentally the ratio of the exchange in the softer layer to the exchange in the harder layer can be increased, the performance of exchange spring media can be improved. According to Ref. 37, a reduction of the exchange constant in the hard magnetic layer leads to a further reduction of the coercive field. Again, this accompanied by a decrease in thermal stability, since the maximum possible energy barrier is given by the domain wall energy. However, care has to be taken that larger values of the exchange constant in the soft magnetic layer require larger layer thicknesses because a significant reduction of the coercive field will only be possible if a full domain wall can be formed within the soft magnetic layer [38].

Micromagnetic simulation that takes into account both coercivity and thermal stability has shown that the magnetization in the softer layer should be similar to the

magnetization in the hard layer in order to maximize thermal stability for a given coercivity (or write field) [38].



The coercivity of bilayer ECC media is determined by the pinning field [39]. For zero anisotropy in the soft layer, the coercive field is reduced by a factor of 4 compared to the coercive field of the hard layer alone. For higher values of the anisotropy in the softer layer the pinning field can even decreased further [38]. The pinning field can be written as

$$H_p = \frac{1}{4} \times \frac{2(K_{hard} - K_{soft})}{J_{hard}}, \quad ,$$

(2-2)

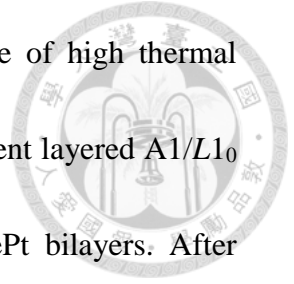
where K_{hard} and K_{soft} are the magnetocrystalline anisotropy parameter of the hard layer and soft layer, respectively, and J_{hard} is the magnetic polarization of the hard layer.

The optimal value (obtaining the lowest coercive field) of the anisotropy in the soft layer is obtained if the nucleation field equals the pinning field. This is the case for $K_{soft} = (1/5)K_{hard}$ [40, 41].

2-4 Graded Films

Suppose the hard layer does not reverse completely due to the large interfacial pinning field, the additional step appears in the hysteresis loop. In contrast, graded films can remove the step, effectively reduce the coercivity and optimize the magnetic reversal behavior by smoothing the vertical motion of the domain wall from the

surface (low K_u) to the hard layer, which results in maintainable of high thermal stability [39]. V. Alexandrakis et al. proposed the structurally gradient layered A1/L1₀ films by heat treatment of magnetron sputter deposited CoPt/FePt bilayers. After annealing, diffusion creates a gradient structure along the film plane normal direction. When the thickness of soft layer is increased to 120 nm, $H_{c\perp}$ decreases from 4.3 to 0.8 kOe [42].



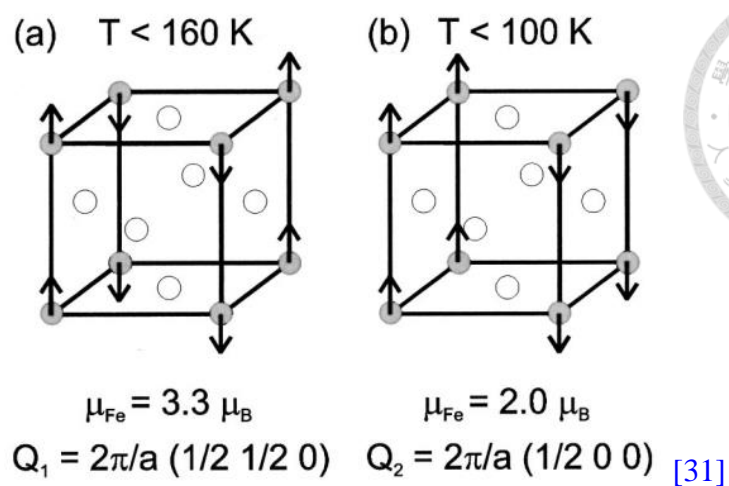


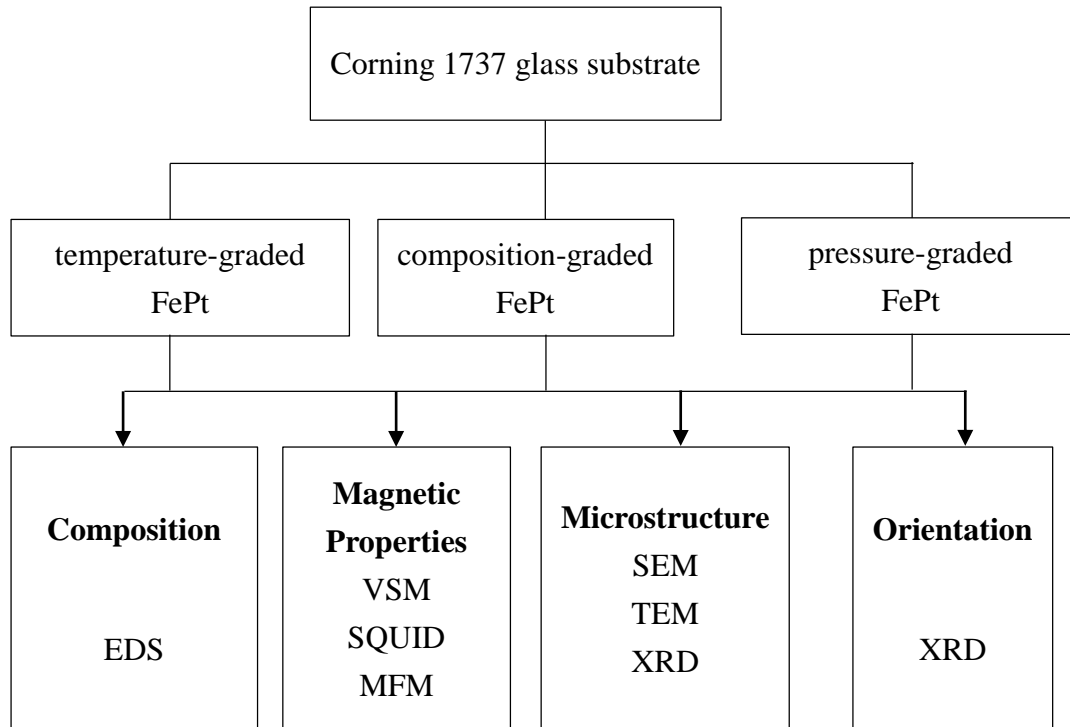
Fig. 2-1 The magnetic structure of $L1_2\text{-FePt}_3$ in the Q_1 phase (a) and the Q_2 phase (b) are shown. The gray spheres represent the Fe atoms, which form a simple cubic lattice, and the white spheres represent Pt atoms [31].

Chapter 3

Experimental Techniques and Methods



3-1 Flow Chart of Experiment



3-2 Sample Preparation

3-2-1 Equipment

Our sputtering machine is ultra-high vacuum multilayer sputter system and was made by ULVAC Technologies, Inc. The machine has two isolated chambers: main- and loading-chamber. There are 8 guns, 2 dc- and 1 rf-power supply on main-chamber. Samples are put in loading-chamber until 5×10^{-7} Torr. Sequentially, we load samples into the main chamber with a mechanical arm and then start to deposit films until 5×10^{-8} Torr. During deposition processing, the maximum dc bias and substrate temperature is $\pm 800V$ and $650^{\circ}C$, respectively. The maximum annealed temperature

in loading-chamber is 450°C. In addition to these functions, we can also use high purity ion to bombard on film surface or to anneal with magnetic field. The sputtering machine and target map was drawn in [Fig.3-1](#) and [3-2](#), respectively.



3-2-2 Substrate Preparation

Substrate is 1737 corning glass for which size is 6.8 mm × 6.8 mm × 0.7 mm. It is very important to clean substrates before using it. First, substrates should be immersed in acetone and cleaned by ultrasonic vibrations. Subsequently, substrates are stored in alcohol. Before sputtering, it is very important to make sure that there are no particles on substrate.

3-2-3 Target Selection

The composition of Fe and Pt targets are 99.99% and MgO is 99.7% for which diameter and thick are 3-inch and 3-mm, respectively.

3-3 Fabrication of graded FePt

3-3-1 Temperature-graded FePt

MgO film were prepared by radio-frequency sputtering in the ultrahigh vacuum system with 5 mTorr of Argon working pressure (Deposition rate of MgO is 0.1914 nm/min). The MgO underlayer with 10-nm thick was firstly deposited on Corning 1737 glass substrate at room temperature (RT) and followed by a post annealing at high temperatures (550°C).

Sequentially, all FePt films were deposited by conventional dc magnetron sputtering with 10 mTorr of Argon working pressure (Deposition rate of FePt is 0.4790 nm/min). Two series of samples were prepared. The statement can be explained as follows.

1. Experimental Group (hard layer + graded layer)

The films consisted of a hard magnetic layer and a graded portion. The hard magnetic layer with a constant thickness of 5 nm, was deposited at T_d of 550°C. The graded layer comprised five FePt layers that were deposited at descending T_d values of 450°C, 350°C, 250°C, 150°C, and RT. The thickness of each layer was set to 1, 2, and 3 nm, yielding a total thickness of the graded portion (t_g) of 5, 10, and 15 nm, respectively. The film structure was drawn in Fig.3-3 (a).

2. Control Group (hard layer + soft layer)

The films consisted of the same hard layer as the aforementioned, and a soft layer of disordered A1 FePt that was deposited at RT. The thicknesses of the soft layer (t_s) were 5, 10, and 15 nm, equal to t_g . The film structure was drawn in Fig.3-3 (b).

3-3-2 Composition-graded FePt

FePt thin films were deposited by radio frequency rotational magnetron co-sputtering. (Deposition rate of FePt is 0.4790 nm/min). The base pressure was

below 5×10^{-8} Torr and the working pressure was kept at 10 mTorr. A MgO underlayer with thickness of 10 nm was firstly deposited on Corning 1737 glass substrate at room temperature (RT), followed by a post annealing at 550°C to induce (001) texture of $L1_0$ -FePt (Deposition rate of MgO is 0.1914 nm/min). The FePt graded film comprises three layers with different Fe compositions; they were FePt (5 nm), $\text{Fe}_{63}\text{Pt}_{37}$ (2 nm) (Deposition rate is 0.4380 nm/min), and $\text{Fe}_{73}\text{Pt}_{27}$ (3 nm) (Deposition rate is 0.5355 nm/min). A FePt layer, the hard layer with high K_u , was deposited on MgO underlayer at 550°C . Then the $\text{Fe}_{63}\text{Pt}_{37}$ and $\text{Fe}_{73}\text{Pt}_{27}$ were sequentially deposited at temperature (T_d) between 300 and 450°C to develop (001) texture and form magnetic anisotropy gradation arising from compositional gradient by interdiffusion. The film structure was drawn in [Fig.3-3 \(c\)](#).

3-3-3 Pressure-graded FePt

The graded $L1_0$ -FePt (001) magnetic films were prepared in a ultra-high vacuum (UHV) magnetron sputtering system. Prior to deposit FePt layer, an underlayer of 10nm-thick MgO initially was grown on glass substrate at room temperature (RT) and post-annealed at 550°C to induce (001)-texture in the FePt hard layer. (Deposition rate of MgO and $L1_0$ -FePt is 0.1914 and 0.4790 nm/min, respectively.) Then a 5-nm- thick FePt hard layer was deposited and subsequently five 1-nm thick FePt layers were grown sequentially with $P_w = 30, 20, 10, 7$ and 3 mTorr. (Deposition rate of FePt with

$P_w = 30, 20, 10, 7$ and 3 mTorr is $0.2507, 0.3213, 0.4048, 0.3797, 0.3778$ nm/min, respectively.) The FePt(P_w)-graded films were fabricated by varying the deposition temperatures, $T_d = 300, 350, 400$ and 450°C . The film structure was drawn in [Fig.3-3](#) (d).

3-4 Analysis Technique

The crystal structure was examined by x-ray diffractometer (XRD) with $\text{Cu-K}\alpha$ radiation; while the surface and cross-section morphology was investigated by scanning electron microscopy (SEM) and transmission electron microscopy (TEM), respectively. The magnetic properties of 5-nm-thick $L1_0$ -FePt hard layer and FePt(P_w)-graded structures were analyzed by vibrating sample magnetometer (VSM) at RT.



Fig. 3-1 Photograph of ultra-high vacuum deposition system.

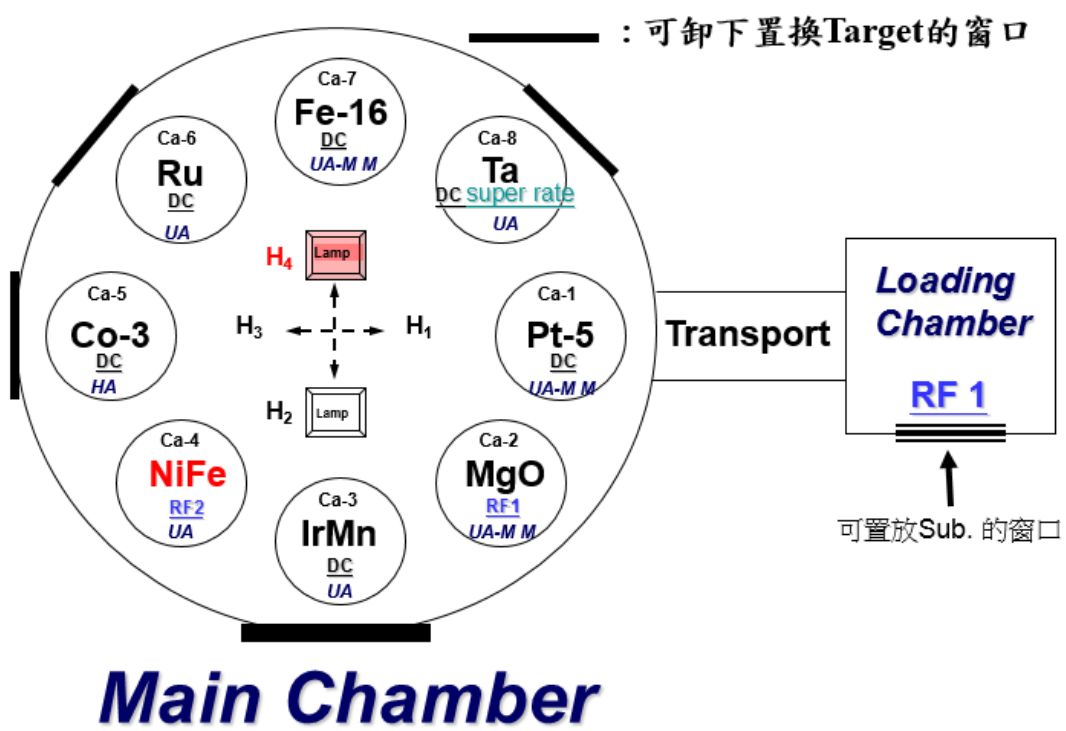


Fig. 3-2 Schematic of target map.

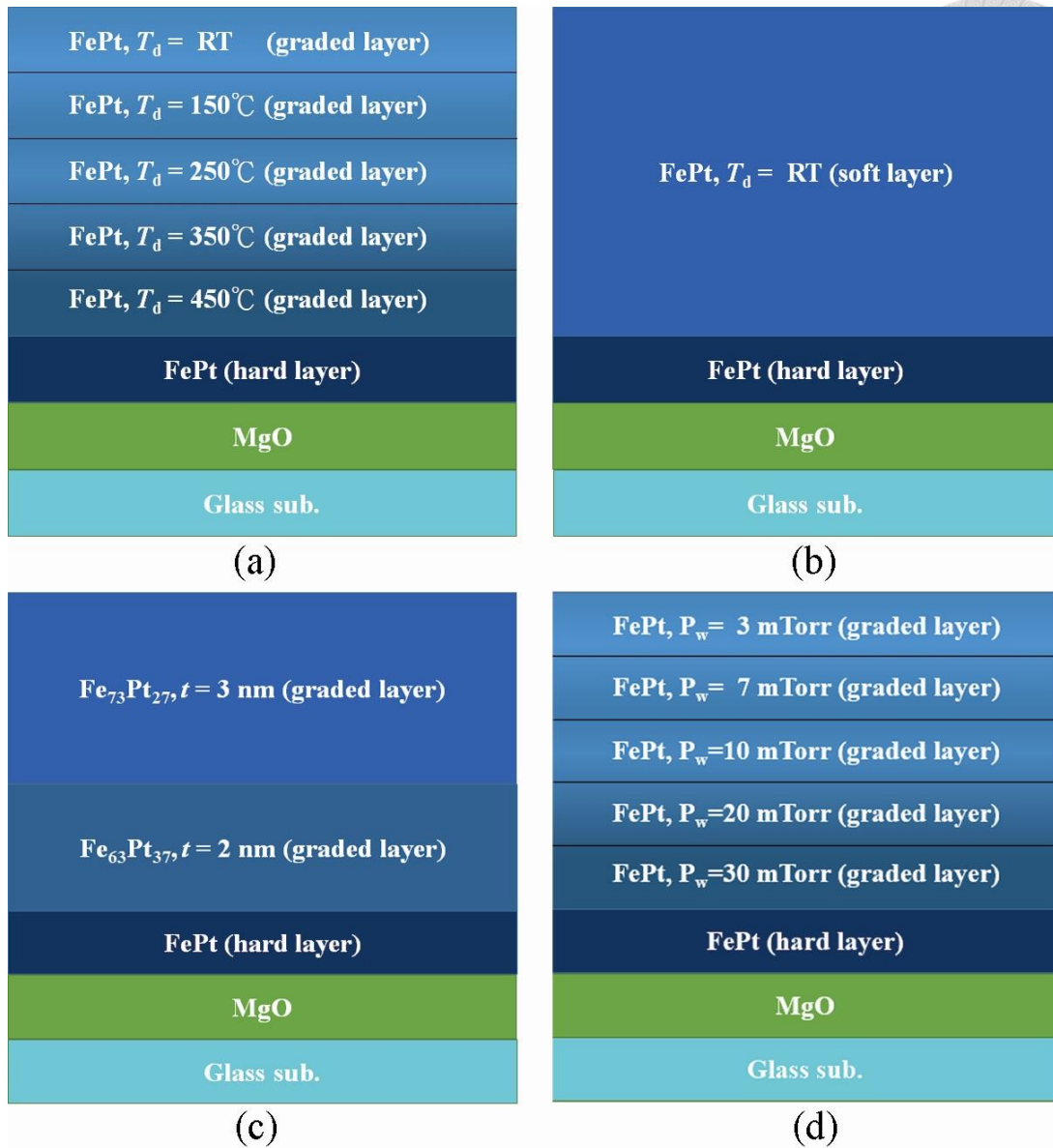


Fig. 3-3 Different types of graded FePt system : experimental group (hard layer + graded layer) (a) and control group (hard layer + soft layer) (b) of temperature-graded FePt ; composition-graded FePt (c) and pressure-graded FePt (d).

Chapter 4

Results and Discussion



The order parameter (S) of $L1_0$ -FePt is the crucial property which controls the intrinsic magnetic properties of films, particularly the magnetic anisotropy. The order parameter has been defined as [43]

$$S = \left(\frac{I_s}{I_f} \times \frac{I_f^*}{I_s^*} \right)^{\frac{1}{2}} = \left(\frac{I_{001}}{I_{002}} \times \frac{I_{002}^*}{I_{001}^*} \right)^{\frac{1}{2}} \quad (4-1)$$

where s refer to the superlattice peaks and f refers to the fundamental peaks. I_s^* and I_f^* are the theoretical integrated peak intensities for a fully ordered $L1_0$ -FePt film, while I_s and I_f are the integrated peak intensity from the experimental results for a partially ordered film. Suppose $S = 1$ represents that $L1_0$ -FePt is fully ordered. For our calculations, we chose $L1_0$ -(001) superlattice and $L1_0$ -(002) fundamental peak to calculate the order parameter in order to prove that our $L1_0$ -FePt films are highly textured. The theoretical fully ordered peak intensity for $L1_0$ -FePt from X-ray diffraction is given by [43]

$$\frac{I_{002}^*}{I_{001}^*} = \frac{(F^2 \times mLPDA)_{002}}{(F^2 \times mLPDA)_{001}} \quad (4-2)$$

where F is the structure factor, m is the multiplicity factor ($m = 2$ for both $L1_0$ -(001) and $L1_0$ -(002)), L is the Lorentz factor ($\frac{1}{4 \sin^2 \theta \cos \theta}$), P is the polarization factor ($\frac{1 + \cos^2 2\theta}{2}$), D is the temperature factor (e^{-2M} where $M = \left(\frac{\sin \theta}{\lambda} \right)^2$), and A is the

absorption factor. For $L1_0$ -FePt structure, suppose the Fe atoms occupy the (0 0 0) and (1/2 1/2 0) lattice sites and the Pt atoms occupy the (1/2 0 1/2) and (0 1/2 1/2) lattice sites, the structure factor of $L1_0$ -(001) and $L1_0$ -(002) peak can be calculate as [43]

$$F_{hkl} = f_{Fe}(1 + e^{\pi i(h+k)}) + f_{Pt}(e^{\pi i(k+l)} + e^{\pi i(l+h)}) \quad (4-3)$$

where f_{Fe} and f_{Pt} are the atomic scattering factors of Fe and Pt which are shown in Fig. 4-1 [43]. The absorption correction factor (A) is an angular (θ) dependent function given by [43]

$$A = 1 - \exp\left(\frac{-2\mu t}{\sin \theta}\right) \quad (4-4)$$

where t is the film thickness, θ is diffraction angle of x-ray, and μ is the average of mass absorption coefficient calculated as [43]

$$\mu = \left\{ \left(\frac{\mu}{\rho}\right)_{Fe} \chi_{Fe} + \left(\frac{\mu}{\rho}\right)_{Pt} \chi_{Pt} \right\} \rho_{FePt} \quad (4-5)$$

where $\left(\frac{\mu}{\rho}\right)_{Fe}$ and $\left(\frac{\mu}{\rho}\right)_{Pt}$ are the mass absorption coefficient of Fe and Pt, χ_{Fe} and χ_{Pt} are the weight fraction of Fe and Pt, and ρ_{FePt} is the density of FePt. The order parameter (S) can be determined by combining the Eqs. (4-1)-(4-4) and showing the values as seen in Table 4-1.

The potential of $L1_0$ -FePt films can be fully harnessed in recording media by significantly reducing their high coercivity without sacrificing magnetocrystalline anisotropy (K_u). Firstly, the $L1_0$ -FePt intensity of (001) is necessary to examine by XRD. Secondly, island-like morphology is need to check with SEM. If the texture

changes from (001) to (111) or (002) to (200), then K_u will get smaller, resulting degraded perpendicular anisotropy.

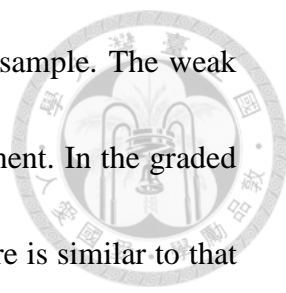


4-1 Temperature-graded FePt

Two series of samples are prepared by different film structures and explained as followings. They were T_g -FePt films with experimental group (hard layer + graded layer) and control group (hard layer + soft layer) as shown in Fig. 3-3 (a) and (b) respectively.

The experimental group films consist of a hard magnetic layer and a graded portion. The hard magnetic layer with a constant thickness of 5 nm, similar to that of the commercial magnetic recording medium, deposited at T_d of 550°C. The graded layer comprised five FePt layers that were deposited at descending T_d values of 450, 350, 250, 150°C, and RT. The thickness of each layer was set to 1, 2, and 3 nm, yielding a total thickness of the graded portion (t_g) of 5, 10, and 15 nm, respectively. The control group films consisted of the same hard layer as the graded films, and a soft layer of disordered A1 FePt that was deposited at RT. The thicknesses of the soft layer (t_s) were 5, 10, and 15 nm, equal to t_g .

Figures 4-2(a)-2(g) present XRD patterns of the hard layer, exchange-spring films of experimental and control group. In Fig. 4-2(a), strong (001) and (002) peaks reveal the formation of a highly ordered $L1_0$ phase with a (001) preferred orientation,

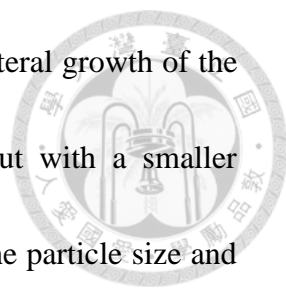


induced by the MgO(002) underlayer in the 5nm-thick hard layer sample. The weak (111) and (200) peaks reveal a small amount of misaligned component. In the graded films with $t_g = 5$, as shown in Fig. 4-2(b), the extent of (001)-texture is similar to that of the hard layer. When $t_g = 10$ nm [Fig. 4-2(c)], the intensity of (001) and (002) peaks increases, revealing that the graded layer grows mainly along [001] following the growth of the hard layer. The increase in the amount of the (200) component suggests that the c -axis orientation of the misaligned grains in the graded part of the film is mainly in-plane. The intensity of (001) and (200) is much lower for the graded film with $t_g = 15$ nm, as shown in Fig. 4-2(d). This result is attributed to the lateral growth of the grains, as revealed in Fig. 4-2, which results in tilting of the c -axis away from film normal to the plane. Unlike in experimental group films, the (001) texture is degraded in the control group samples, even at the smallest t_s of 5 nm [Fig. 4-2(e)]. As t_s increases, the (111) peak grows. In the sample with $t_s = 15$ nm, the preferred orientation is (111), as shown in Fig. 4-2(g). Although the surface morphology of the hard/soft samples is similar to that of the hard bottom layer, the disordered FePt soft layer does not exhibit the (001) texture, because the low deposition temperature (RT) suppresses diffusion, leading to the (111)-texture, which is the most stable atomic arrangement for fcc metal films.

The alignment of crystal axes was studied using the rocking curves of $L1_0$ (001)

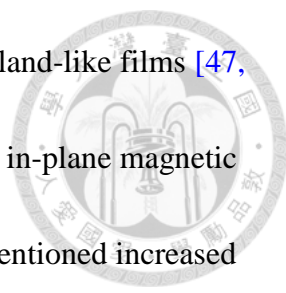
peak as shown in Fig. 4-3(a). The experimental data are shown in Fig. 4-3(b) and the full width at half maximum (FWHM) is obtained by fitting Gaussian function and the results are plotted as a function of T_d in Fig. 4-3(b). For comparison, the value of FWHM for the single 5-nm-thick $L1_0$ FePt is also included in the figure. It is noted that the value of FWHM increase substantially from 3.1 to 4.97° as t_g is increased from 5 to 15 nm. The increasing values of FWHM reflect a degraded (001)-texture with the deposition of graded layers at elevating t_g .

Figure 4-4 displays SEM images of the hard layers, exchange-spring films of experimental and control group with various thicknesses. The 5nm-thick hard layer exhibited an island-like morphology with grain size of 16 ± 7 nm and average inter-granular distance of 10 nm, respectively [Fig. 4-4(a)]. As the thickness of the hard layer increased to 20 nm, the size of the island gradually increased to about 97 ± 33 nm and the separation between grains increased to 15-20 nm, as presented in Fig. 4-4(b). Interestingly, the deposition of graded and soft layers seemed not to affect particle size. The morphology of the exchange-spring films of experimental and control group with $t_g = t_s = 5$ nm [Figs. 4-4(c) and 1(d)] is similar to that of the island structure of the 5nm-thick hard layer and both of its grain size is 15 ± 5 nm, although with a slightly smaller particle separation. Different surface morphologies were observed when t_g and t_s were increased to 15 nm. The particles were connected to



each other, forming a network in the graded film, because of the lateral growth of the islands; the hard/soft sample maintained a particulate surface but with a smaller separation, as displayed in Figs. 4-4(e) and 1(f). The retention of the particle size and the reduced separation between particles in the graded and hard/soft films suggest a *ledge-type* microstructure [44], where the graded or soft layer has a larger horizontal length than the underlying hard magnetic islands. This ledge structure, proposed by Lomakin *et al.* [45], allows for a drastic reduction of the switching field and precessional magnetic reversal, enhancing the writability of a patterning media [45, 46].

Figure 4-5 plots in-plane and out-of-plane hysteresis loops for the hard layer, exchange-spring films of experimental and control group. The hard layer samples with thicknesses of 5 and 20 nm have a large perpendicular coercivity ($H_{c\perp}$) of 17.5 and 14.3 kOe, respectively, as presented in Figs. 4-5(a) and 3(b). The maximum applied magnetic field of 2 T is not sufficient to saturate the films, causing asymmetric hysteresis especially in the 5nm-thick sample. The experimental group films have smaller $H_{c\perp}$. As t_g is increased from 5 to 15 nm, $H_{c\perp}$ declines from 12.5 to 8.2 kOe. The sample with $t_g = 5$ nm has a linear demagnetization curve beyond the nucleation point, indicated by the arrow in Fig. 4-5(c), suggesting that the coupling between the hard and graded layers is strong so that the magnetization switches



coherently. The curve has a small slope, typical of (001)-textured island-like films [47, 48], and indicative of independent magnetic reversal. The increased in-plane magnetic component in the film with $t_g = 10$ nm is consistent with the aforementioned increased intensity of the (200) peak. The increased t_g and in-plane magnetic component smooth the demagnetization curve, as indicated in Fig. 4-5(e). The film with $t_g = 15$ nm [Fig. 4-5(g)] has a different reversal path. First, spontaneous demagnetization occurs at around 1 T (-1 T) in the descending (ascending) region of the hysteresis loop before the removal of the applied field. This phenomenon may be caused by tilting of the magnetization in the top of the graded part where K_u is quite small. Second, the reversal that is induced by the formation and propagation of anti-parallel domain in the graded part takes place in a field of 0 to ± 8 kOe. Similar behavior has been identified in FePt (111)-textured films with K_u gradation [49]. Lastly, the hard layer switches in high fields. This reversal mechanism effectively reduces $H_{c\perp}$ by a factor of 2.2. However, the control group films also exhibit a significant drop in $H_{c\perp}$, but the magnetic properties and reversal mechanism differ from those in the graded samples of experimental group. Figure 4-5(d) shows a low squareness ratio of 0.6 and a large in-plane magnetic component for the sample with $t_s = 5$ nm. The magnetic moments near the surface of the soft layer tilt toward the in-plane direction because of the weak coupling force from the bottom hard layer, resulting in a reversible change in

magnetization in the first (third) quadrant. When t_s increases to 10 and 15 nm, the films become in-plane magnetic anisotropic, as shown in Figs. 4-5(f) and 3(h), where the shape anisotropy dominates in the most part of the soft layer.

Figure 4-6 plots the dependence of the perpendicular coercivity ($H_{c\perp}$) as a function of t_g . The value is normalized to the coercivity of 5nm-thick hard layer. The $H_{c\perp}$ declines from 17.5 kOe for the 5nm-thick hard layer to 8.2 kOe for the graded films with $t_g = 15$ nm. It is noted that $H_{c\perp}$ drops drastically by a factor of 2.1 as graded layer thickness $t_g = 15$ nm. $H_{c\perp}$ value tends decrease gradually with increase of t_g .

Figure 4-7 shows the perpendicular hysteresis loops and recoil curves of 5-nm-thick $L1_0$ -FePt hard layer and T_g -FePt ($t_g = 5$ nm). Fig. 4-8 reveals the reversible and irreversible magnetization as a function of the applied reversal field (H_r) for $L1_0$ -FePt and T_g -FePt. This quantity was defined as [50, 51]

$$M_{rev} = M_d(H) - M(H) \quad (4-6)$$

$$M_{irr} = M_r - M_d(H) \quad (4-7)$$

where M_r is the remanent magnetization of major loop, $M_d(H)$ is the remanent magnetization obtained after removing the applied field from H_r . $M(H)$ is the magnetization obtained at H_r . In the case of $L1_0$ -FePt, upon removal of the applied field (H_r) during demagnetization process, only slightly increased magnetization can

be found, indicating the switching mechanism is dominated by irreversible switching.

On the other hand, for T_g-FePt, the magnetization increases sharply upon removal of the applied field. This increment in the magnetization is due to the presence of reversible magnetization switching.

First-order reversal curve (FORC) measurements are employed in order to provide a detailed analysis of the reversal mechanisms and the induced anisotropy gradient. The FORC curves are follow the procedure: After positive saturation the applied field is reduced to a given reversal field, H_r . From this reversal field the magnetization is measured back towards positive saturation thereby tracing out a single FORC. This process is repeated for a series of decreasing reversal fields. The FORC distribution is then defined as a mixed second order derivative of normalized magnetization:

$$\rho(H, H_r) \equiv -\frac{1}{2} \frac{\partial^2 M(H, H_r) / M_s}{\partial H \partial H_r} \quad (4-8)$$

which is then plotted against (H, H_r) coordinates on a contour map. For a given reversal field (H_r), the magnetization is measured for increasing applied field (H), and therefore $H \geq H_r$ by design. Families of FORCs and the corresponding FORC distribution are shown in Fig. 4-9. A single and highly localized peak along with a pair of negative-positive tails was observed in the FORC distribution, suggesting the

existence of both soft and hard phase.

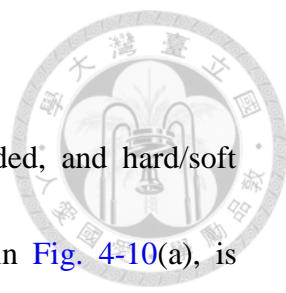


Figure 4-10 presents MFM images of the hard layer, graded, and hard/soft samples. The domain size of the 5nm-thick hard layer, shown in Fig. 4-10(a), is around 50 nm, which exceeds the observed island size of 15-25 nm, confirming the interaction domain structure. The contrast is weak because the film is thin. As the thickness of the hard layer is increased from 10 to 20 nm, the growth of the island results an increase in the domain size from 80-100 to 150-200 nm, respectively [Figs. 4-10(b) and 4(c)]. The graded films with $t_g = 5$ and 10 nm [Figs. 4-10(d) and 4(e)] have similar domain sizes, which are slightly larger than that of the 5nm-thick hard layer but smaller than that of the 10nm-thick hard layer, revealing that the domain size is controlled by the hard layer via strong exchange coupling. Larger domains appear in the film with $t_g = 15$ nm, but their average size is still smaller than that of the 20nm-thick hard layer. The hard/soft samples - even including the thinnest sample with $t_s = 5$ nm - yield a rather weak image contrast. The weakened contrast reflects weak magnetic flux normal to the film plane, possibly caused by the interconnection of grains in the soft layer, which facilitates the tilting of magnetization to in-plane. The domain size of the hard/soft samples is larger than that in the graded films of the same thickness and increases with t_s as shown in Figs. 4-10(g)-(i).

4-2 Composition-graded FePt

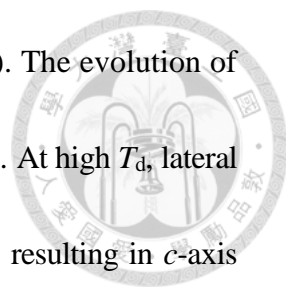
In this section, the $\text{Fe}_{73}\text{Pt}_{27}/\text{Fe}_{63}\text{Pt}_{37}/L1_0\text{-FePt}(001)$ trilayer was proposed to realize the perpendicular graded behavior. First, a hard layer of FePt with a nominal thickness of 5 nm was deposited onto a (001)-texture MgO at 550°C. Afterwards, $\text{Fe}_{63}\text{Pt}_{37}$ and $\text{Fe}_{73}\text{Pt}_{27}$ layers with different K_u were deposited sequentially at temperature (T_d) between 300 and 450°C to develop (001) texture and form magnetic anisotropy gradation arising from compositional gradient by interdiffusion.

Figures 4-11 and 4-12 present the XRD patterns of the hard layer with 5 and 10 nm in thickness and graded films, respectively. In Fig. 4-11(a), strong (001) and (002) peaks are observed in both samples, confirming the formation of highly ordered $L1_0$ phase with a (001) preferred orientation. In 10 nm-thick hard layer, weak (111) and (200) peaks appear, which indicates a small amount of misaligned grains. In the graded film with $T_d = 300^\circ\text{C}$, the intensities of (001) and (002) peaks are weaker as compared to those of the single hard layer sample, suggesting the misalignment of the graded layer due to the low processing temperature. When T_d is increased to 350 and 400°C, as shown in Figs. 4-12(b) and (c), the intensities of (001) and (002) peaks become much stronger, indicating good alignment of the graded layer. As T_d reaches 450°C, both (001) and (002) peaks disappear and a small (111) peak emerges, as shown in Fig. 4-12(d).

The alignment of crystal axes was studied using the rocking curves of $L1_0$ (001)

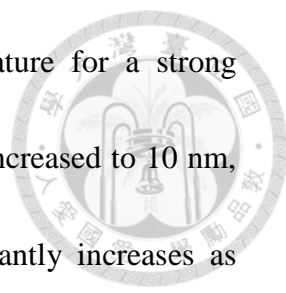
peak as shown in Fig. 4-13(a). The experimental data are shown in Fig. 4-13(b) and the full width at half maximum (FWHM) is obtained by fitting Gaussian function and the results are plotted as a function of T_d in Fig. 4-13(b). For comparison, the value of FWHM for the single 5-nm-thick $L1_0$ FePt is also included in the figure. It is noted that the value of FWHM increase substantially from 3.1 to 4.69° as T_d is increased from 350 to 450°C . The increasing values of FWHM reflect a degraded (001)-texture with the deposition of graded layers at elevating T_d .

Figure 4-14 shows the SEM images of the hard layer with 5 and 10 nm in thickness and graded films. Both 5nm and 10nm-thick hard layers exhibit an island-type morphology [Figs 4-14(a) and (b)]. The size of the grains for the 5nm-thick film is 16 ± 7 nm and the average separation of the particles is around 6 to 10 nm. As the thickness of the hard layer increases to 10 nm, the size of the islands is gradually enlarged to 38 ± 16 nm and the separation between the grains increases to 6-13 nm, as revealed in Fig. 4-14(b). The SEM images indicate that the surface morphology at $T_d = 300^\circ\text{C}$ is almost identical to the single hard layer sample as shown in Fig. 4-14(c). This result confirms that the graded layer is stacked directly on the hard FePt $L1_0$ island grains. When T_d is increased to 350°C [Fig. 4-14(d)], a slight increase in the average island-type particle size accompanied with a reduction in grain separation is observed. The islands start to coarsen and interconnect forming a



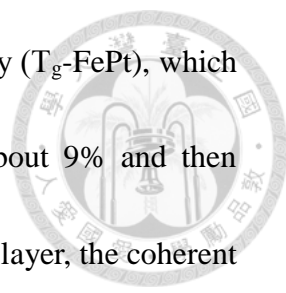
network structure at $T_d \geq 400^\circ\text{C}$, as indicated in Fig. 4-14(e) and (f). The evolution of surface morphology may be explained by the change in film texture. At high T_d , lateral growth of the grains leads to texture reorientation of the FePt grains, resulting in c -axis incline from the film plane normal. On the other hand, since the morphology of hard layer is fixed, the reduced separation between the grains in the graded films ($T_d \geq 400^\circ\text{C}$) suggest a *ledge-type* microstructure [49], where the graded layers have a larger horizontal length than the underlying hard magnetic islands. This ledge structure, proposed by Lomakin *et al.* [52], allows for a drastic reduction of the switching field and precessional magnetic reversal, could largely enhance the writability of a patterning media [52, 53]. It can be concluded that the morphology of the graded films in this work is essentially determined by deposition temperature T_d : a lower T_d ($\leq 400^\circ\text{C}$) will have the graded films to exhibit island-type structure while higher T_d ($> 400^\circ\text{C}$) changes the graded films into ledge-type and even network-type. Similar surface morphology evolution was found in our previous investigation. Nevertheless, change in surface morphology is caused by the increase in film thickness [54].

The in-plane and out-of-plane hysteresis loops for the 5- and 10nm-thick hard and graded samples are plotted in Figs 4-15. Both types of films exhibit magnetically single-phase reversal behavior. A 5nm-thick hard layer shows a large perpendicular coercivity ($H_{c\perp}$) of 20.0 kOe, high squareness ratio (S) of 0.89, and small in-plane



component in the loop as shown in Fig. 4-15(a), a typical feature for a strong (001)-textured FePt film. When the thickness of the hard layer is increased to 10 nm, $H_{c\perp}$ decreases to 15.6 kOe and the in-plane component significantly increases as revealed in Fig. 4-15(b), which corresponds to the degraded (001)-texture as observed in Fig. 4-11(b). Significant reduction in $H_{c\perp}$ is observed in all the graded films and the selected results are shown in Figs. 4-15(c) and (d) for $T_d = 300$ and 400°C , respectively. The relatively small in-plane hysteresis loops and unchanged anisotropy field manifest by the presence of good PMA. The obtained values of $H_{c\perp}$ are 7.2 kOe and 9.1 kOe for $T_d = 300$ and 400°C respectively. The graded films have smaller S in the range of 0.65 to 0.75, implying the tilting of the magnetic moment near the surface of the film. This reversible change in magnetization in the first (third) quadrant is due to the weak coupling between the bottom hard layer and the topmost part of the graded layer where the magnetic anisotropy is the smallest. The film with $T_d = 300^\circ\text{C}$ shows the most obvious tilting behavior ($S = 0.65$), causing the reversal behavior analogous to the exchange-spring films. In the film with $T_d = 350$ and 400°C , S increases to around 0.75, suggesting the enhancement of K_u in the Fe-rich graded layer.

Figure 4-16 plots the dependence of the perpendicular coercivity ($H_{c\perp}$) as a function of T_d . The value is normalized to the coercivity of 5nm-thick hard layer. Notably, $H_{c\perp}$ drops drastically by a factor of 2.8 after a graded layer is deposited at

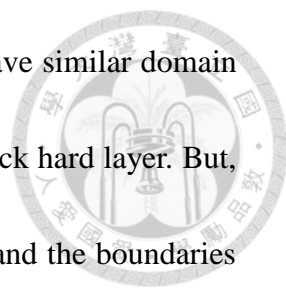


300°C. This reduction factor is larger than that in our previous study (T_g-FePt), which is 2.1 [54]. With further increase in T_d , $H_{c\perp}$ slightly rises by about 9% and then declines again. This variation can be explained as follows. For hard layer, the coherent rotation of the highly ordered $L1_0$ single-domain island particles produces large H_c . At $T_d = 300^\circ\text{C}$, the temperature is not high enough to enable the graded layer follow the (001) texture of the underneath hard layer to grow and trigger the interdiffusion between the hard and graded layers. The PMA of the Fe-rich layer is thus small; the difference in K_u values across the interface of the hard and graded layers is large, leading to magnetization reversal behavior similar to that of an exchange-spring film. When T_d is increased to 350 and 400°C, the formation of strong (001) texture (as confirmed in Fig. 4-12(b) and (c)) and onset of interdiffusion increase the magnetization alignment and create K_u gradation along the depth by forming gradient of Fe concentration. However, the competition between the improved (001) texture and the formation of graded K_u results in a slight increase in $H_{c\perp}$. As T_d is further raised to 450°C, extensive diffusion causes lateral growth of the grain, forming network-type morphology and large amount of misaligned grains. Most importantly, the intensive diffusion along depth changes the binary composition of the hard layer, seriously degrading the PMA of the hard layer, resulting in a low S of 0.6 and decreasing $H_{c\perp}$ (7.7 kOe) at 450°C.

Figure 4-17 shows the perpendicular hysteresis loops and recoil curves of 5-nm-thick $L1_0$ -FePt hard layer and C_g -FePt ($T_d = 350^\circ\text{C}$). Fig. 4-18 reveals the reversible and irreversible magnetization as a function of the applied reversal field (H_r) for $L1_0$ -FePt and C_g -FePt. In the case of $L1_0$ -FePt, upon removal of the applied field (H_r) during demagnetization process, only slightly increased magnetization can be found, indicating the switching mechanism is dominated by irreversible switching. On the other hand, for C_g -FePt, the magnetization increases sharply upon removal of the applied field. This increment in the magnetization is due to the presence of reversible magnetization switching.

Families of FORCs and the corresponding FORC distribution are shown in Fig. 4-19. A single and highly localized peak along with a pair of negative-positive tails was observed in the FORC distribution, suggesting the existence of both soft and hard phase.

Figures 4-20 illustrates MFM images of the hard layer and graded samples. The domain size of the 5nm-thick hard layer, as shown in Fig. 4-20(a), is around 100 to 140 nm, which exceeds the observed island size of 25-50 nm, suggesting the interaction domain structure. The contrast is relatively weak because of the small thickness. As the thickness of the hard layer is increased to 10 nm, the domain size slightly increases to 100-170 nm [Figs. 4-20(b)], which could be related to the growth

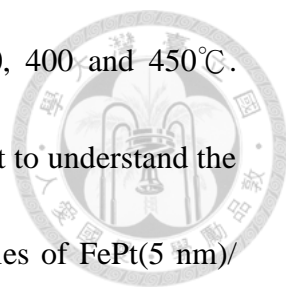


of the island-type grains. All the graded films [Figs. 4-20(c)-(f)] have similar domain pattern and the average domain size is close to that of the 10nm-thick hard layer. But, the contrast of the images of the graded samples is a little weaker and the boundaries of domains are broader. These features are closely related to the fact that the film has K_u gradation along the depth direction. And the tilt of the surface moment reduces the magnetic contrast and the reduced PMA near surface broadens the domain wall width. Even so, compared with the domain images of the graded films prepared by other methods, sharper contrasts are observed for the graded films herein, indicating improved PMA and better crystal alignment in this type of graded structure.

Figure 4-21 shows the depth profile of Auger electron spectroscopy (AES) of the C_g -FePt samples with $T_d = 300, 350$ and 400°C . It clearly reveals that the existing Fe composition gradient as $T_d \leq 350^\circ\text{C}$. However, the great amount of Mg and O in FePt degrades the gradient performance due to the extensive diffusion.

4-3 Pressure-graded FePt

A 5 nm-thick FePt hard layer was initially deposited on glass substrates and then graded- FePt layers with each individual layer thickness of 1 nm were grown by following a graded-working pressure (P_w) sequence of 30, 20, 10, 7 and 3 mTorr. An under layer of 10-nm thick MgO grown at room temperature and post-annealed at 550°C was used to induce (001)-texture in FePt layer. The P_w -graded FePt layers were



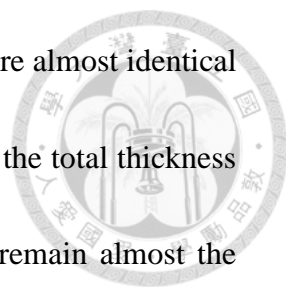
fabricated with different deposition temperatures, T_d of 300, 350, 400 and 450°C. Prior to discuss the performance of P_w -graded layers, it is important to understand the effect of P_w -sequence on the K_u variation. For this purpose, a series of FePt(5 nm)/MgO(10 nm)/glass samples were deposited at 550°C with $P_w = 3, 10, 20$ and 30 mTorr and the results are presented in Fig. 4-22. It clearly indicates that in our studied range of P_w higher P_w results in larger K_u –indicating that K_u can be gradually controlled by varying P_w from 3 to 30 mTorr. Magnetic gradient has been also achieved in Co/Pd pressure-graded system [55]. The observed graded magnetic structure is believed due to a decrease in saturation magnetization for regions deposited at progressive higher working pressure. However, a different origin causes the dependence of K_u on the working pressure in our studied system. The increase of K_u is attributed to the improved chemical ordering S_{ord} with higher working pressure P_w [56, 57].

Figure 4-23(a) reveals the XRD patterns of 5-nm thick $L1_0$ -FePt and the FePt(P_w)-graded structures. It can be seen that the $L1_0$ (001) texture can be enhanced by MgO(200). The graded films at $T_d < 400^\circ\text{C}$ have strong (001) and (002) peaks – indicating the presence of highly ordered $L1_0$ phase. However, the width of $L1_0$ (002) peak increased along with increasing (200) peak at $T_d \geq 400^\circ\text{C}$. The increase in (200)-texture is accompanied with the lateral growth of FePt grains, the SEM images

will be shown in Fig. 4-24(e) and (f).

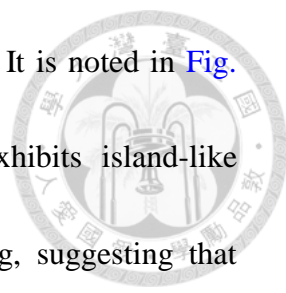
The alignment of crystal axes was studied using the rocking curves of $L1_0$ (001) peak. The experimental data are shown in Fig. 4-23(b) and the full width at half maximum (FWHM) is obtained by fitting Gaussian function and the results are plotted as a function of T_d in Fig. 4-23(c). For comparison, the value of FWHM for the single 5-nm-thick $L1_0$ FePt is also included in the figure. It is noted that the value of FWHM increase substantially from 3.1 to 3.9° as T_d is increased from 300 to 400°C and then level off with further increasing T_d . Only a small difference is found between those of the graded layers deposited at 300°C and a single 5-nm-thick $L1_0$ FePt layer. The increasing values of FWHM reflect a degraded (001)-texture with the deposition of graded layers at elevating T_d .

Figures 4-24(a) – (f) depict the SEM morphologies along with histograms showing grain-size distribution for the 5-nm- and 10-nm-thick $L1_0$ -FePt hard layers and the FePt(P_w)-graded structures processed at $T_d = 300 - 450^\circ\text{C}$, respectively. The 5-nm-thick FePt hard layer shows an island-like morphology with grain size of 16 ± 7 nm and average inter-granular distance of 10 nm, respectively (Fig. 4-24(a)). In contrast, for the 10-nm-thick FePt hard layer, both the grain size (38 ± 16 nm) and inter-granular distance (10-15 nm) were considerably increased (Fig. 4-24(b)). However, the FePt(P_w)-graded films follow the morphology of 5-nm-thick hard layer



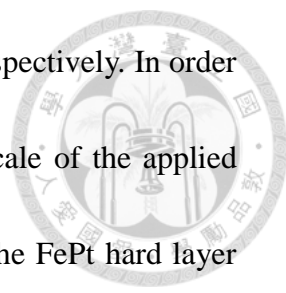
until $T_d \geq 400^\circ\text{C}$ (Figs. 4-24(c) - (d)). The size and its distribution are almost identical to those of 5-nm-thick FePt hard layer. It is worthy of mention that the total thickness of the FePt(P_w)-graded/FePt(5 nm) is 10 nm, but the grain sizes remain almost the same as that of only a 5nm-thick FePt hard layer. Furthermore, magnetic domains of island-type graded layer also follow their underneath $L1_0$ -FePt hard layer [54, 58] (figures not shown here). As $T_d \geq 400^\circ\text{C}$, the grains tend to connect with each other and become ledge- [44, 59] or even maze-like [60] morphology (Figs. 4-24(e) and (f)), wherein the graded films have a larger horizontal length than the underneath hard magnetic island structure. Additionally, a different size distribution is observed.

Figures 4-25(a)-(d) represents the typical cross-sectional TEM images of 5-nm-thick FePt hard layer and the FePt(P_w)-graded films grown at $T_d = 350$ and 450°C , respectively. As shown in Fig. 4-25(a), the interface of FePt/MgO is very smooth and FePt layer has distinct island structure with the lateral size of 15 nm, which is consistent with the SEM image (Fig. 4-24(a)). The magnified image of the dash-square region in Fig. 4-25(a) is displayed in Fig. 4-25(b). A good epitaxial growth initiating from the MgO layer and FePt grains grown on MgO with well-developed (001)-texture are observed. The planar spacing of FePt is found to be 0.37 nm, which is in good agreement with the value of 0.37 obtained from XRD data. Also, the #43-1359 PDF data file gives 0.371 nm, close to our value. This result



further confirms that the FePt layer with the $L1_0$ phase is formed. It is noted in Fig. 4-25(c) that the graded layers grown at $T_d = 350^\circ\text{C}$ also exhibits island-like morphology with (001)-texture and 0.37 nm-thick planar spacing, suggesting that graded FePt layers are epitaxially grown along the (001) orientation of 5-nm-thick $L1_0$ -FePt hard layer. However, the interfaces between each graded layers in P_g -FePt film are difficult to identify, due to similar compositions in each P_g -FePt graded layer. Nevertheless, the top graded layers, 2 nm from the film surface and deposited at lower working pressures (3 and 7 mTorr), do not show clear layer structure. It implies that the reduction of ordering parameter occur with decreasing Argon pressure during film deposition thus causing the decline of K_u . Further increasing deposition temperature to $T_d = 450^\circ\text{C}$ (Fig. 4-25(d)) the grains tend to connect with each other, which confirms that the ledge-type morphology has a larger horizontal length than the underneath hard magnetic island structure. The top 2-nm region is no longer separated from the lower 3-nm region. But, the whole graded layers are distributed in random orientations with different values of planar spacing between 0.33 and 0.37 nm. Intensive and extensive interdiffusion along the film plane normal direction at higher deposition temperatures produces large amount of defects and lattice strain causing the worse performance of graded layer.

Both in-plane and out-of-plane hysteresis loops for the 5nm-thick FePt hard layer



and the FePt(P_w)-graded films are illustrated in Figs 4-26(a)-(d), respectively. In order to demonstrate the coercivity reduction of the graded films, the scale of the applied field in Fig. 4-26(a) is different from those in Figs. 4-26(b)-(d). The FePt hard layer exhibits a large $H_{c\perp}$ of 20.0 kOe and high perpendicular anisotropy field of > 70.0 kOe with a small in-plane magnetic component –which is a typical feature of $L1_0$ -FePt with strong (001) texture. The graded samples deposited at $T_d = 300$ and 350 °C show a significant decrease in $H_{c\perp}$ from 20.0 to 5.1 kOe and both the films exhibit a similar magnetization reversal behavior (Fig. 4-26(b) and (c)), but quite different from that of a bare FePt hard layer. At a large field, all the magnetic moments are directed toward the saturation magnetization. When the field is decreased to the nucleation field (denoted by H_n in Fig. 4-26(b)) of the top soft layer, small reverse domains are nucleated. Subsequently, the magnetization reversal in the graded part is induced by the propagation of anti-parallel domain. So the magnetic moments of softest layer start to depart from the easy axis with reduction in applied field [39]. The switching of the upper part of the soft layer occurs at the applied field close to the soft layer anisotropy field [35]. The domain wall is then pinned near the hard/soft interface with a pinned field (H_p) [35]. As the field is further increased the domain wall in the soft layer is compressed and it penetrates more and more into the hard layer [35]. Once the applied field reaches 13.4 kOe the domain wall depins from

the hard/soft interface and propagates immediately through the entire hard layer [35].

With further increasing at $T_d \geq 400^\circ\text{C}$, a large in-plane component appears accompanied by an enhancement in in-plane H_{cl} as shown in Fig. 4-26(d).

Figure 4-27 shows the dependence of the $H_{c\perp}$ as a function of T_d for the FePt(P_w)-graded structures. The $H_{c\perp}$ values are normalized with respect to $H_{c\perp}$ of 5-nm thick FePt hard layer. It can be noticed that the $H_{c\perp}$ drastically drop by a factor of 3.9 for the FePt(P_w)-graded layer deposited at $T_d \leq 350^\circ\text{C}$ and these values tend increase gradually with further increase of T_d . The decreasing and increasing trends with respect to T_d can be explained as follows. When $T_d \leq 350^\circ\text{C}$, the formation of perpendicular graded structure leads to reduce $H_{c\perp}$ significantly (Fig. 4-26(b) and (c)). Besides, this film also exhibit minimal in-plane component. The diffusion process starts to occur when $T_d \geq 400^\circ\text{C}$. As discussed previously the fct FePt (001) texture is destroyed and the graded behavior is degraded. When T_d is further raised to 450°C , extensive diffusion causes lateral growth of the grain, forming network-type morphology and large amount of misaligned grains leading to worse performance of graded behavior. Additionally, the substantial reduction of $H_{c\perp}$ does not lead to the degradation of the thermal stability in our graded films prepared by gradient working pressure method. According to Sharrock [61], the dynamic coercivity $H_c(t)$ as function of measuring time can be expressed by the following equation

$$H_c(t) = H_0 \left\{ 1 - \left[\frac{k_B T}{K_u V^*} \ln \frac{f_0 t}{\ln 2} \right]^{1/n} \right\} \quad (4-9)$$

where k_B , T , K_u , V^* , f_0 and n are the Boltzmann constant, measuring temperature, anisotropy energy constant, switching volume, attempt frequency and parameter n , respectively. Parameter n depends on the magnetization orientation with respect to the applied field and is normally taken to be 1.5. Performing the moment-decay measurements [62], the thermal stability factor ($K_u V^*/k_B T$) can be determined by fitting (4-9). The $K_u V^*/k_B T$ value of 71 is obtained for the film with graded layers deposited at 300 °C, which satisfies the requirement that the thermal stability of the recording medium should be in the range of 50-70 to keep the media noise within acceptable bounds [5, 7, 63]. Furthermore, even T_d is increased up to 400°C, the thermal stability factor only drops to 61.

Figure 4-28 shows the perpendicular hysteresis loops and recoil curves of 5-nm-thick $L1_0$ -FePt hard layer and P_g -FePt ($T_d = 350^\circ\text{C}$). Fig. 4-29 reveals the reversible and irreversible magnetization as a function of the applied reversal field (H_r) for $L1_0$ -FePt and P_g -FePt. In the case of $L1_0$ -FePt, upon removal of the applied field (H_r) during demagnetization process, only slightly increased magnetization can be found, indicating the switching mechanism is dominated by irreversible switching. On the other hand, for P_g -FePt, the magnetization increases sharply upon removal of the applied field. This increment in the magnetization is due to the presence of reversible

magnetization switching.

Families of FORCs and the corresponding FORC distribution are shown in Fig. 4-30. A single and highly localized peak along with a pair of negative-positive tails was observed in the FORC distribution, suggesting the existence of both soft and hard phase. This is the typical case for soft-hard coupled layers reported in the graded media [49].

4-4 Comparison of Three Systems

All the three graded structures were essentially grown onto a 5-nm thick FePt hard layer, supported with 10-nm thick MgO underlayer. A temperature sequence of 450, 350, 250, 150 °C and RT; while a pressure sequence of 30, 20, 10, 7 and 3 mTorr with each layer of thickness of 1-nm were followed for T_g- and P_g-FePt films. In the case of C_g-FePt, layers with different Fe compositions: Fe₆₃Pt₃₇ (2 nm) and Fe₇₃Pt₂₇ (3 nm) were considered for graded structures.

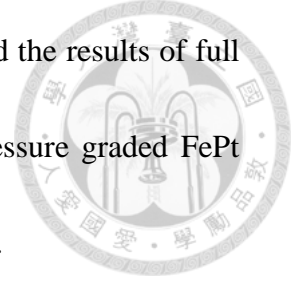
4-4(a) Structure Analysis

1. XRD Pattern and Texture Orientation

For comparison, Fig. 4-31 shows the XRD patterns of different gradient systems. All of the three gradient systems display the strong (001) and (002) peaks, which indices the formation of a highly ordered *L*1₀ phase.

Figure 4-32 displays the alignment of crystal axes using the rocking curves of

$L1_0$ (001) peak. The experimental data are shown in Fig. 32 (a) and the results of full width at half maximum (FWHM) are plotted for comparison. Pressure graded FePt shows the best (001) alignment among these three gradient systems.



4-4(b) Microstructure Analysis

1. SEM Morphology

Figure 4-33 shows the SEM morphology and its grain size distribution. It is easy to find that grain size and separating distance are almost the same between different gradient systems. However, the island-grain-size-distribution of C_g -FePt films is the lowest one comparing to the other two gradient systems as shown in Fig. 4-34.

Island-like morphology is achieved and maintained as $t_g < 15$ nm in T_g -FePt and $T_d \leq 350^\circ\text{C}$ in both C_g - and P_g -FePt systems as shown in Fig. 4-35. The particles were connected to each other until $t_g = 15$ nm in T_g -FePt and $T_d > 350^\circ\text{C}$ in both C_g - and P_g -FePt systems. It suggests a *ledge-type* microstructure, where the graded layer has a larger horizontal length than the underlying hard magnetic islands.

2. Cross-sectional TEM

Related discussion was described in section 4-3.

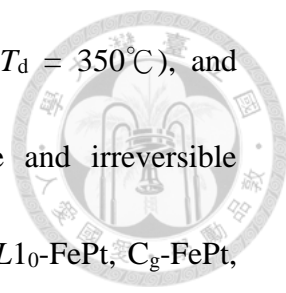
4-4(c) Magnetism Analysis

Magnetic study reveals a significant reduction in $H_{c\perp}$ values with respect to $L1_0$ -FePt hard layer as shown in Fig. 4-36. The $H_{c\perp}$ declines from 20 kOe for the

5nm-thick hard layer to 7.2 kOe for the graded films with $t_g = 5$ nm in temperature graded films. Notably, H_c drops by a factor of 2.8 and maintains high magnetocrystalline anisotropy constant (K_u). Similarly, $H_{c\perp}$ declines to 7.8 and 6.1 kOe in composition and pressure graded films, respectively. The H_c value drops drastically by a factor of 2.6 and 3.3, however it also maintains high K_u .

Figure 4-37 shows the dependence of the perpendicular coercivity as a function of graded films thickness (t_g) and deposited temperature (T_d) in different gradient systems. This variation can be explained as follows. It is noted that the $H_{c\perp}$ value decrease substantially with t_g in temperature graded films. Mainly, the $H_{c\perp}$ value drops drastically as $T_d \leq 350^\circ\text{C}$ both in composition and pressure graded films. When T_d is increased to 350 and 400°C , the formation of strong (001) texture and onset of interdiffusion increase the magnetization alignment and create K_u gradation along the depth. However, the competition between the improved (001) texture and the formation of graded K_u results in a slight increase in $H_{c\perp}$. As $T_d > 450^\circ\text{C}$, extensive diffusion causes lateral growth of the grain, forming network-type morphology and large amount of misaligned grains. Most importantly, the intensive diffusion along depth changes the binary composition of the hard layer, seriously degrading the PMA of the hard layer.

Figure 4-38 shows the perpendicular hysteresis loops and recoil curves of



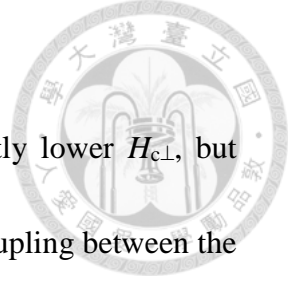
5-nm-thick $L1_0$ -FePt hard layer, T_g -FePt ($t_g = 5$ nm), C_g -FePt ($T_d = 350^\circ\text{C}$), and P_g -FePt ($T_d = 350^\circ\text{C}$) films. Fig. 4-39 reveals the reversible and irreversible magnetization as a function of the applied reversal field (H_r) for $L1_0$ -FePt, C_g -FePt, T_g -FePt, and P_g -FePt. In the case of $L1_0$ -FePt, upon removal of the applied field (H_r) during demagnetization process, only slightly increased magnetization can be found, indicating the switching mechanism is dominated by irreversible switching. Both T_g - and P_g -FePt have the similar reversal behavior. On the other hand, for C_g -FePt, the magnetization increases sharply upon removal of the applied field (Fig. 4-39(a)). This increment in the magnetization is due to the presence of reversible magnetization switching arising from the non-coherent rotation [64].

The contour maps of FORC distribution are shown in Fig. 4-40. All of them have a single and highly localized peak along with a pair of negative-positive tails in the FORC distribution, suggesting the existence of both soft and hard phase. But only P_g -FePt is the typical graded-media due to the highly coupled reversal of soft and hard phases.

4-5 Summary

In Section 4-1:

1. This study examined the structure and magnetic properties of FePt (001) island-like films on glass substrates when the films were coated with a graded



layer and a disordered FePt soft layer.

2. Both graded and exchange-spring films have a significantly lower $H_{c\perp}$, but only graded samples retain strong PMA due to the strong coupling between the layers.
3. The $H_{c\perp}$ declines from 20 kOe for the 5nm-thick hard layer to 7.2 kOe for the graded films with $t_g = 5$ nm. The graded film also exhibits magnetic reversal path that is similar to that prediction for graded media.
4. The domain structure provides further evidence of the coupling configuration of the films.
5. The results of our study confirm that a graded structure can effectively reduce the switching field and ensure sufficient PMA of a hard layer with island-like morphology, in agreement with theoretical studies.

In Section 4-2:

1. Island-like morphology is achieved after the introduction of compositional-variation graded layer.
2. The introduction of compositional gradient is found to produce gradation of magnetic anisotropy.
3. The coercivity can be significantly reduced to 2.6 times without significant sacrifice of anisotropy field.

In Section 4-3:

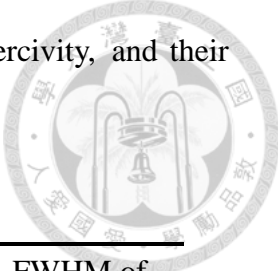


1. Island-like morphology is achieved and maintained after the introduction of pressure-graded layer as $T_d \leq 350^\circ\text{C}$.
2. The pressure-graded films are found to also exhibit the graded media behavior.
3. The coercivity can be significantly reduced to 3.3 times without significant sacrifice of anisotropy field.
4. The result of FORC measurements clearly indicate the highly coupled reversal of soft and hard phases.

Table 4-1 Calculations for I_{001}^* and I_{002}^* —theoretical integrated peak intensities for a fully ordered of $L1_0$ -FePt films.

	001	002
$2\theta (^{\circ})$	23.83	48.38
f_{Fe}	21.61	16.74
f_{Pt}	69.47	58.73
F^2	9162.32	22782.88
Lorentz factor	5.994	1.6323
Polarization factor	0.9184	0.7206
M	0.0179	0.0706
Temperature factor	0.9648	0.8683
$(\frac{\mu}{\rho})_{\text{Fe}}$ (cm^2/g)	304.4	
$(\frac{\mu}{\rho})_{\text{Pt}}$ (cm^2/g)	198.2	
χ_{Fe} (%)	25.92	
χ_{Pt} (%)	74.08	
ρ_{FePt} (g/cm^3)	15.49	
μ_{FePt} (cm^{-1})	3344.75	
Absorption factor	0.0161	0.0081
Intensity	2501.19	730.13
Order parameter	0.91	

Table 4-2 Grain size diameter, nucleation field, perpendicular coercivity, and their corresponding FWHM values.



Sample type	Condition	Grain diameter (nm)	H_n (kOe)	$H_{c\perp}$ (kOe)	FWHM of (001)-rocking curve ($^\circ$)
Hard layer	5 nm	9-23	X	20.0	3.1
T_g	$t_g = 5$ nm	10-20	+29.8	7.2	4.19
C_g	$T_d = 350^\circ\text{C}$	14-22	+29.4	7.8	4.24
P_g	$T_d = 350^\circ\text{C}$	12-24	+33.6	6.1	3.3

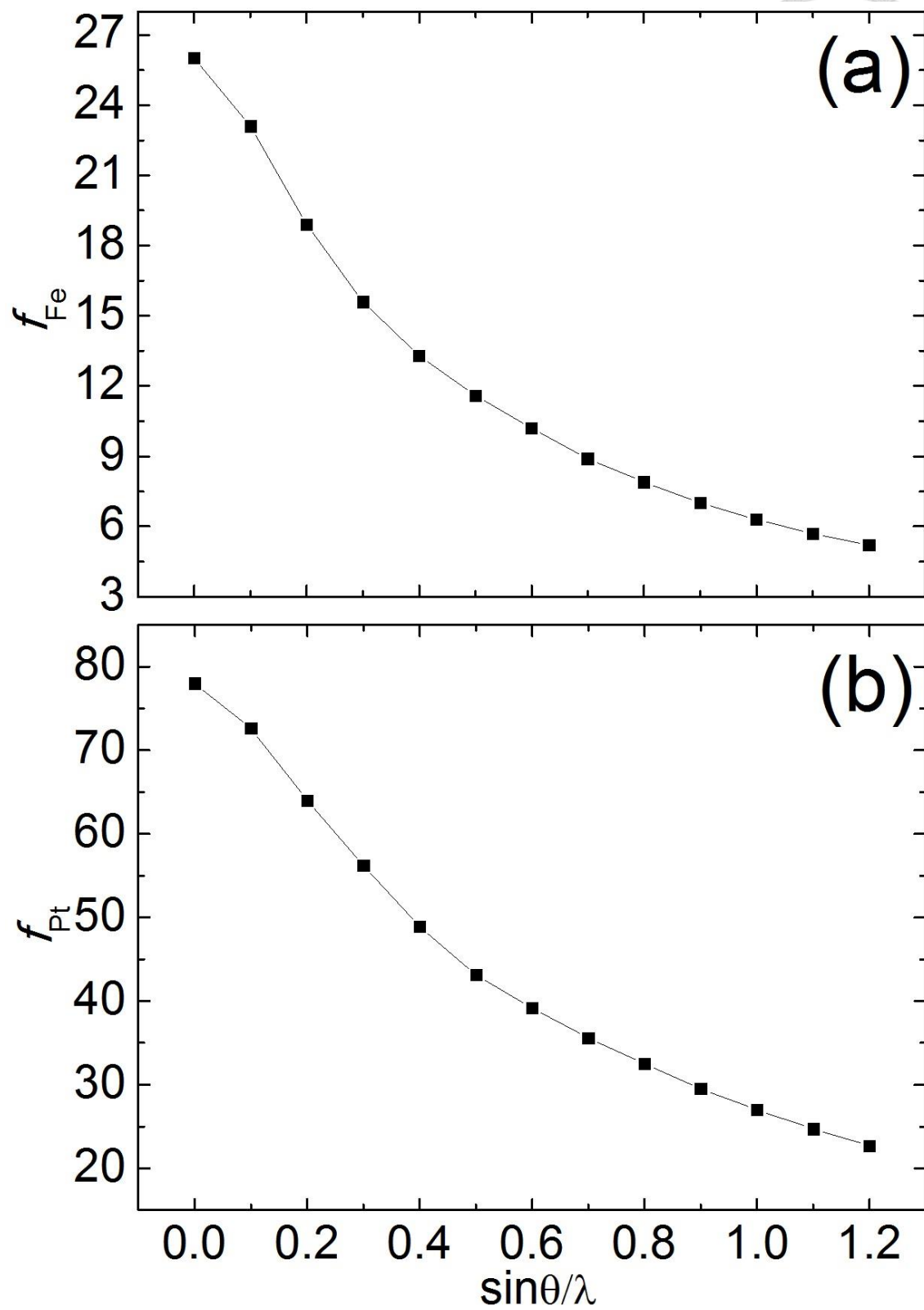


Fig. 4-1 Atomic scattering factors of Fe (a) and Pt (b) as a function of $\sin\theta/\lambda$.

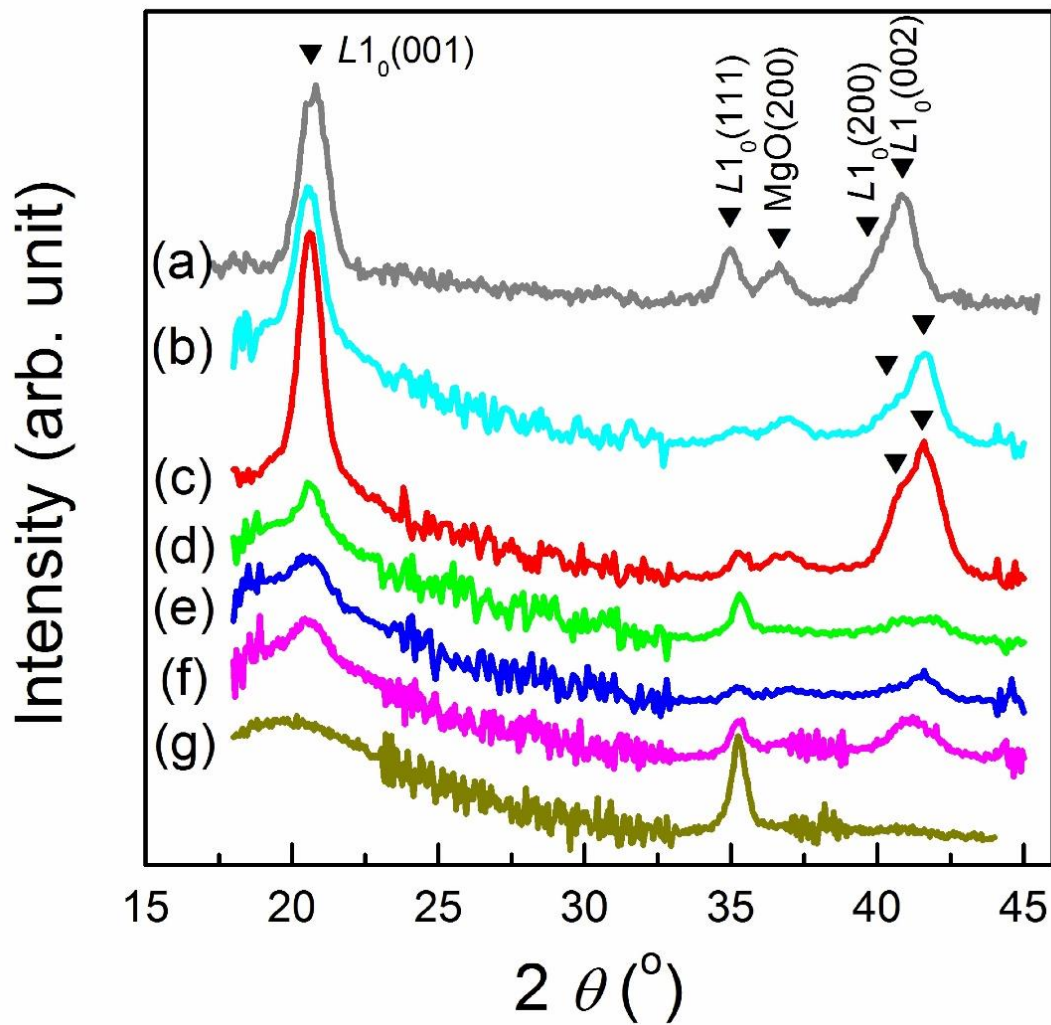


Fig. 4-2 XRD patterns for the samples of (a) 5-nm-thick hard layer, graded films with $t_g =$ (b) 5, (c) 10, and (d) 15 nm, and hard/soft films with $t_s =$ (e) 5, (f) 10, and (g) 15 nm. (measured at National Synchrotron Radiation Research Center (NSRRC) beamline 17B in Hsinchu, Tawian)

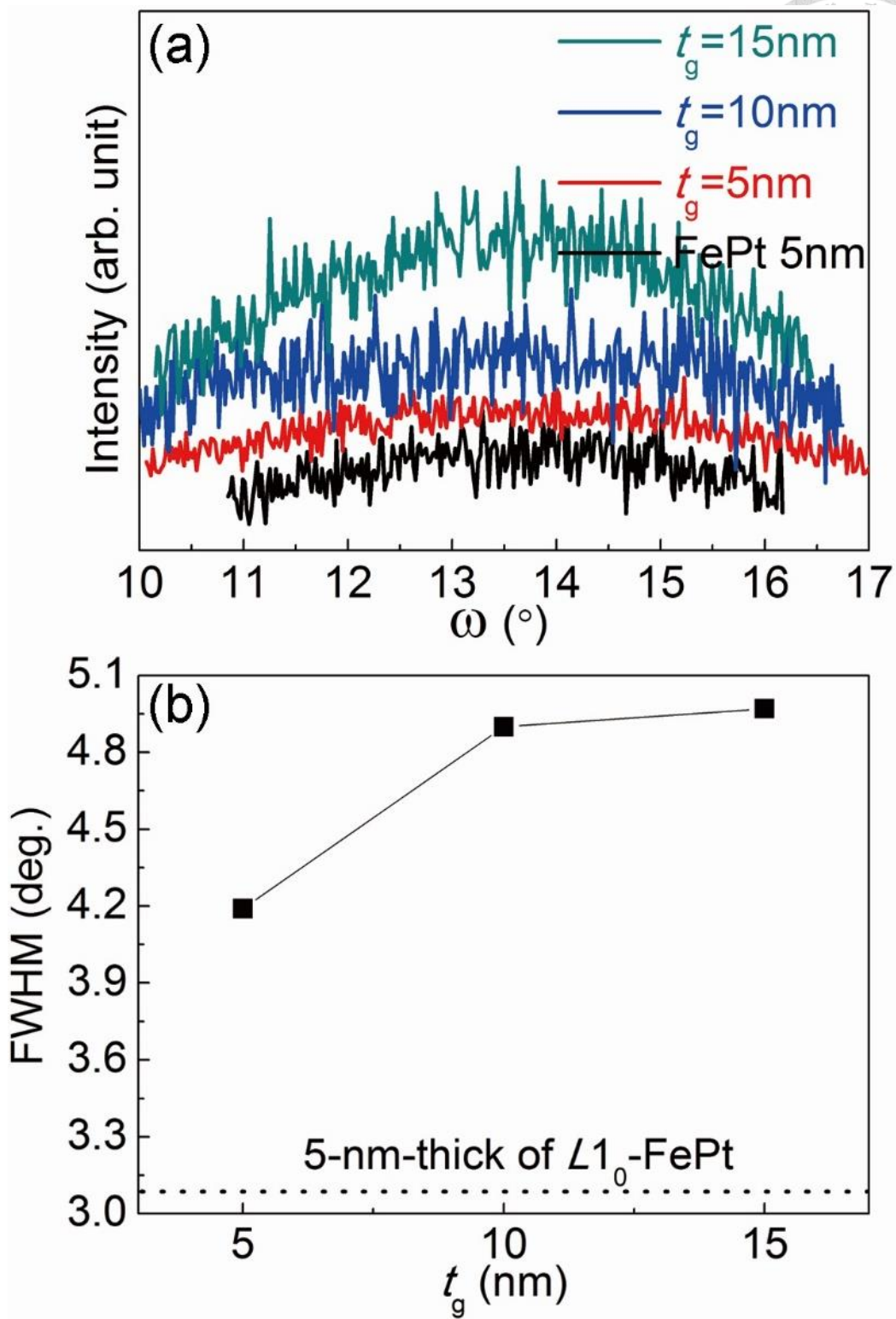


Fig. 4-3 (001)-rocking curves of 5-nm-thick $L1_0$ -FePt hard layer and the FePt(T_g)-graded layers grown at different t_g : 5, 10, and 15 nm (a); and their corresponding FWHM values as a function of t_g (b).

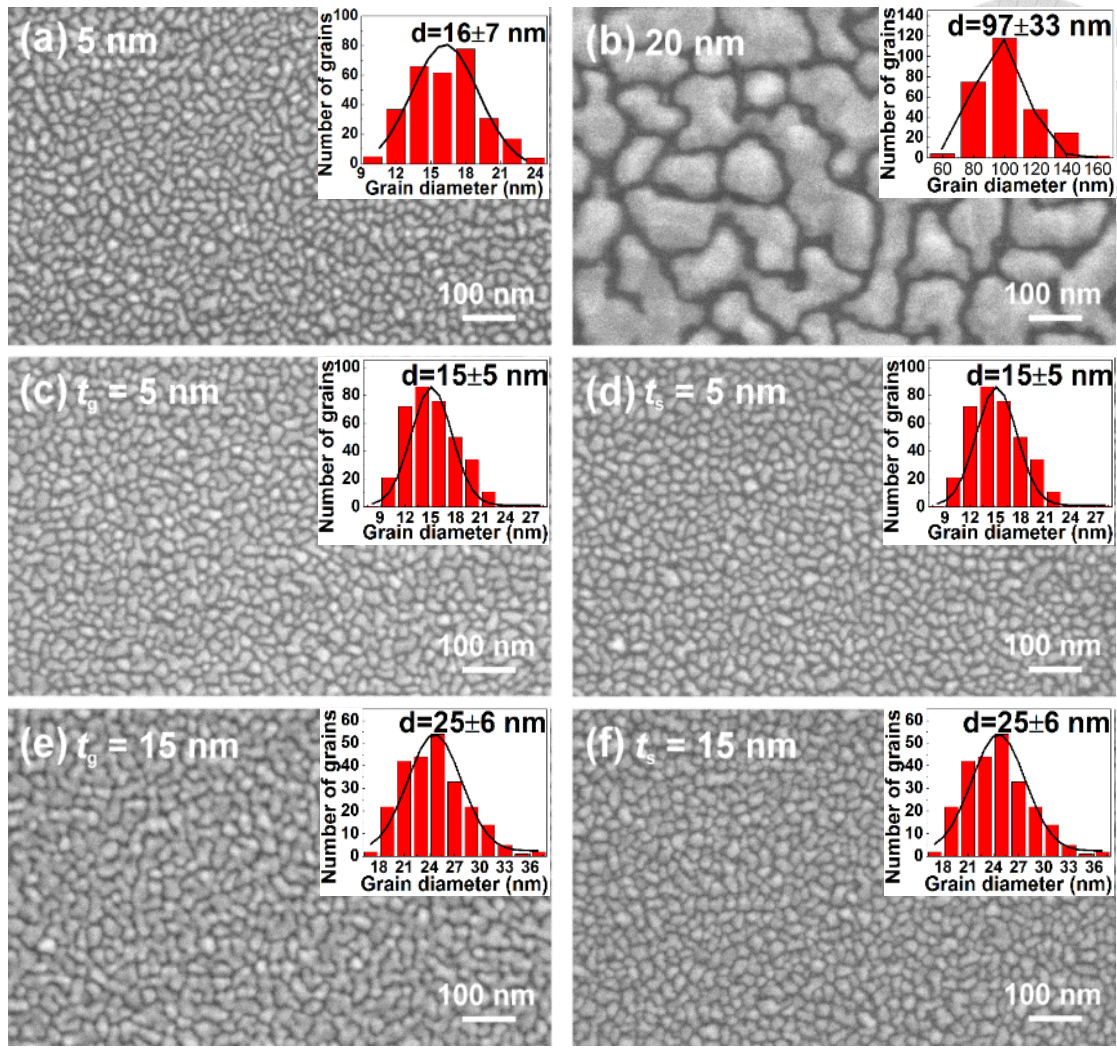


Fig. 4-4 SEM images for the samples of hard layer with thickness of (a) 5 and (b) 20 nm, graded films with t_g = (c) 5 and (e) 15 nm, and hard/soft films with t_s = (d) 5 and (f) 15 nm. The corresponding histograms are included in the inset of each figure.

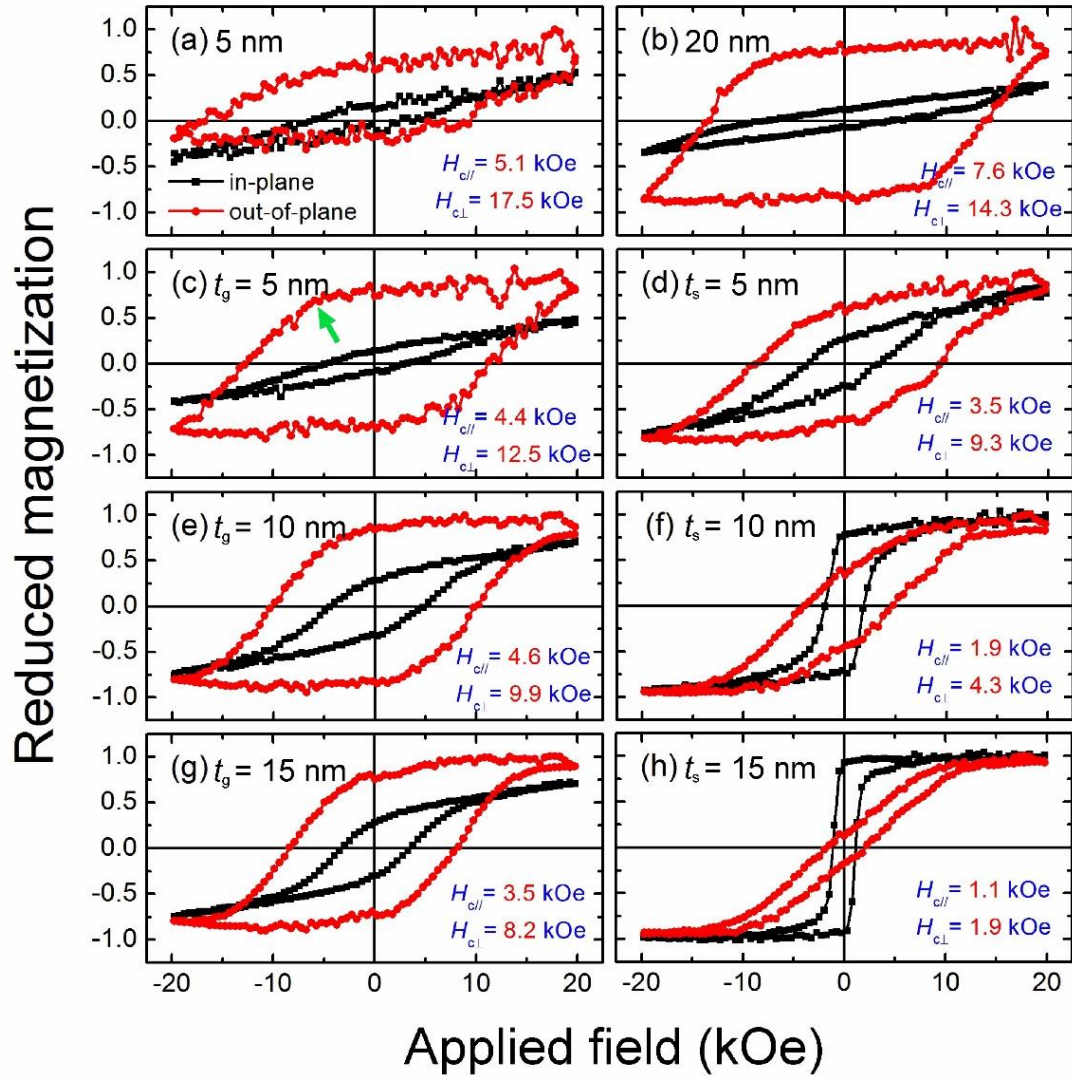


Fig. 4-5 In-plane and out-of-plane hysteresis loops for the samples of (a) 5-nm-thick and (b) 20-nm-thick hard layer, graded films with t_g = (c) 5, (e) 10, and (g) 15 nm, and hard/soft films with t_s = (d) 5, (f) 10, and (h) 15 nm.

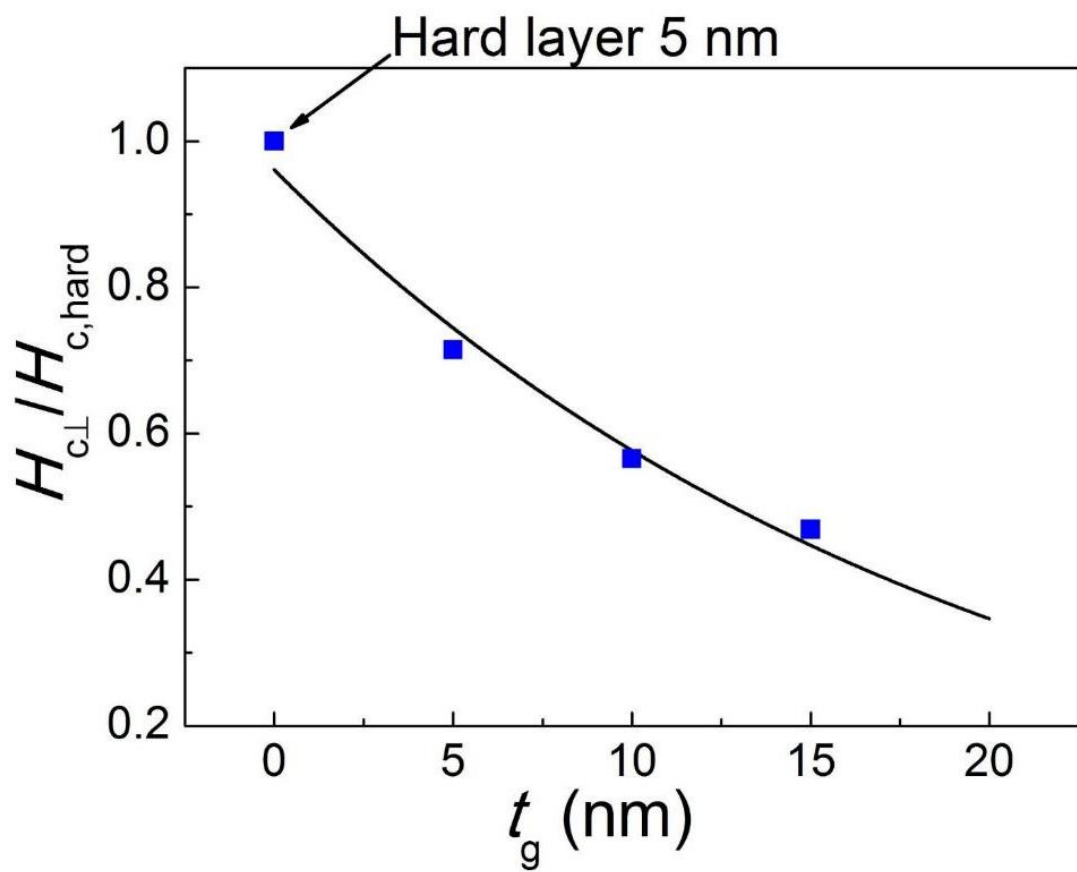


Fig. 4-6 $H_{c\perp}/H_{c\perp,hard}$ as a function of T_d for the FePt(P_w)-graded films.

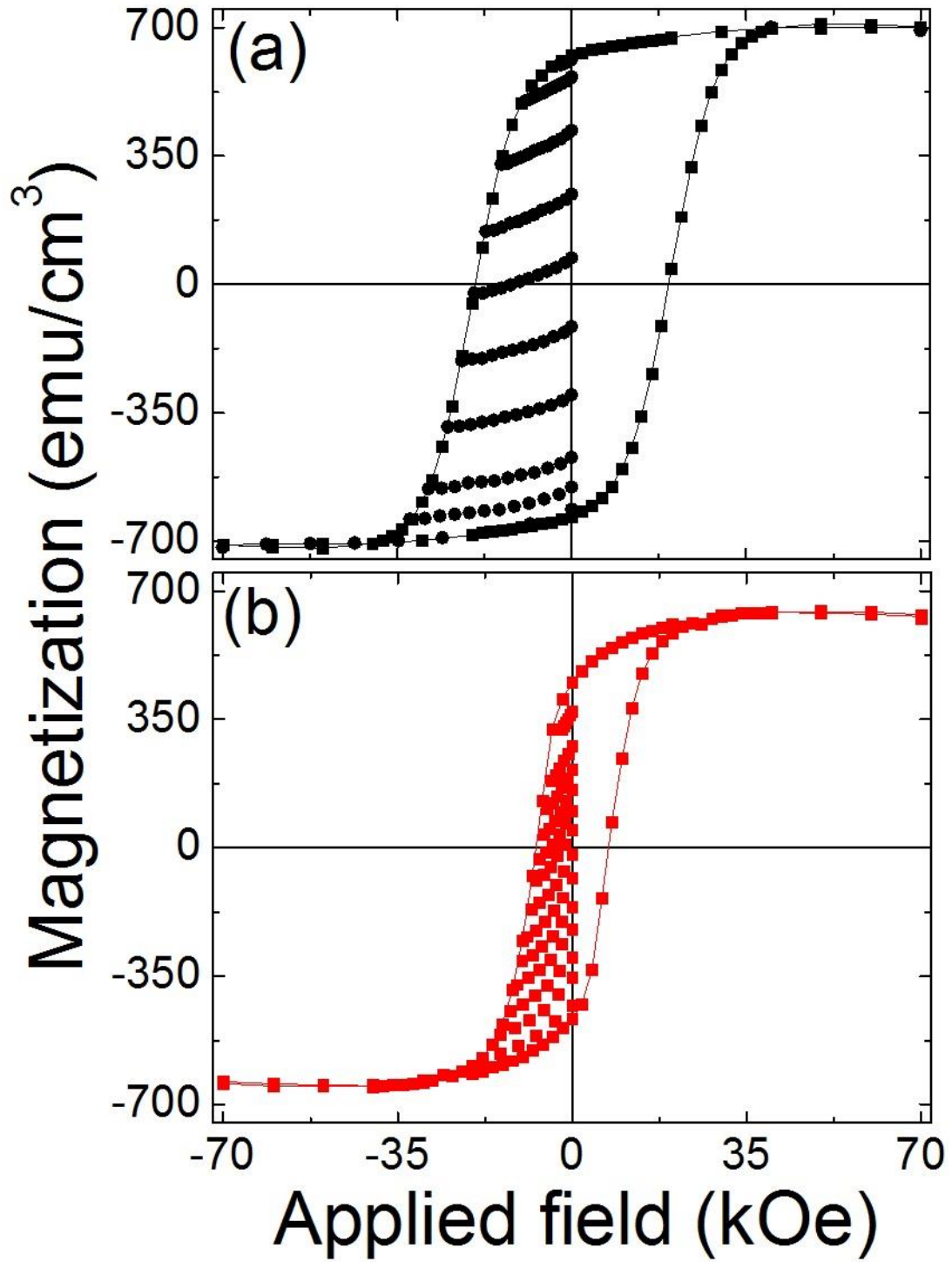


Fig. 4-7 Perpendicular hysteresis loops and recoil curves (measured by SQUID-VSM) of 5-nm-thick $L1_0$ -FePt (a) and T_g -FePt with $t_g = 5$ nm (b).

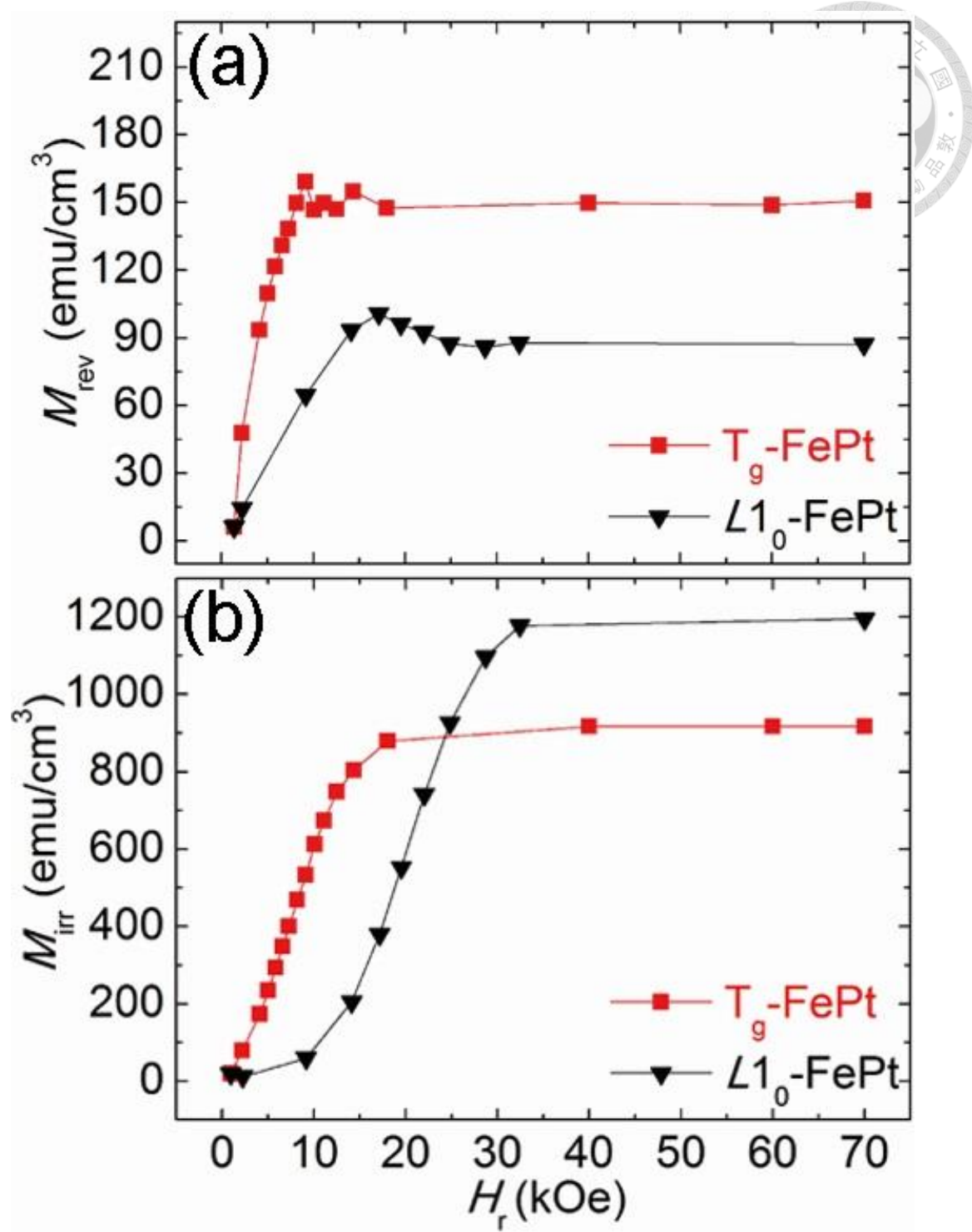


Fig. 4-8 Reversible (a) and irreversible magnetization (b) as a function of the applied reversal field (H_r) for 5-nm-thick $L1_0$ -FePt and T_g -FePt with $t_g = 5$ nm.

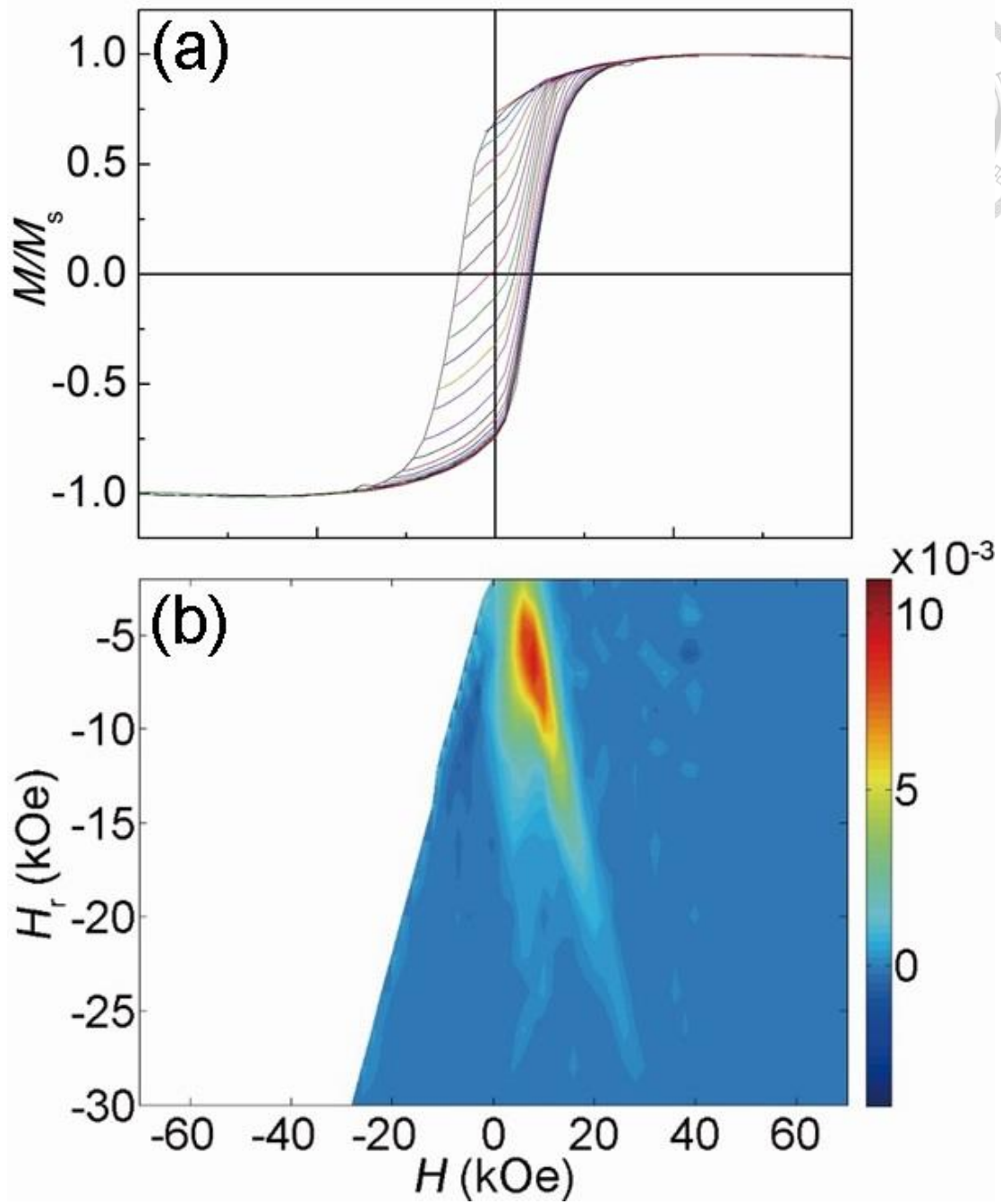


Fig. 4-9 Families of FORC's of T_g -FePt with $t_g = 5\text{nm}$ (a) and the corresponding FORC distribution (b).

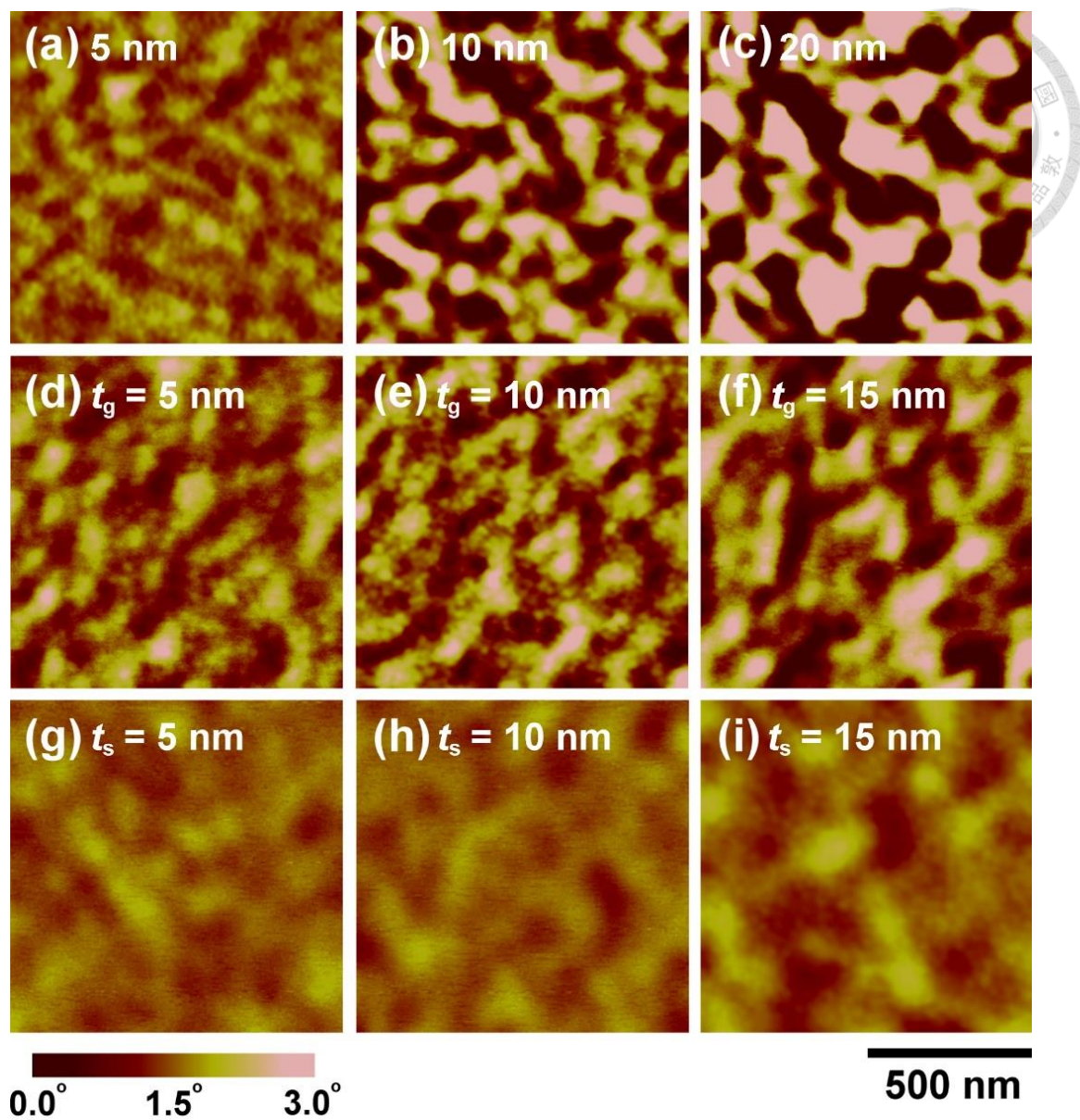


Fig. 4-10 MFM images for the samples of hard layer with thickness of (a) 5, (b) 10, and (c) 20 nm, graded films with $t_g =$ (d) 5, (e) 10, and (f) 15 nm, and hard/soft films with $t_s =$ (g) 5, (h) 10, and (i) 15 nm.

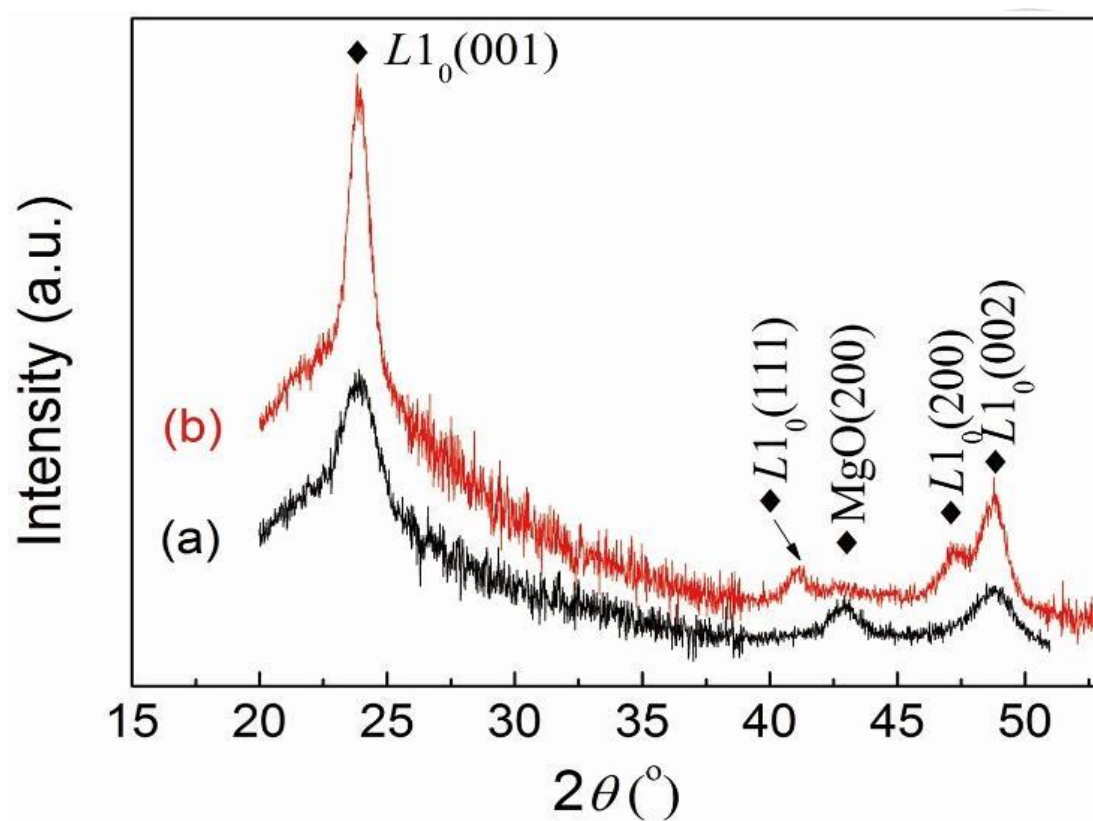


Fig. 4-11 XRD patterns for the samples of hard layer with 5-nm-thick (a) and 10-nm-thick.

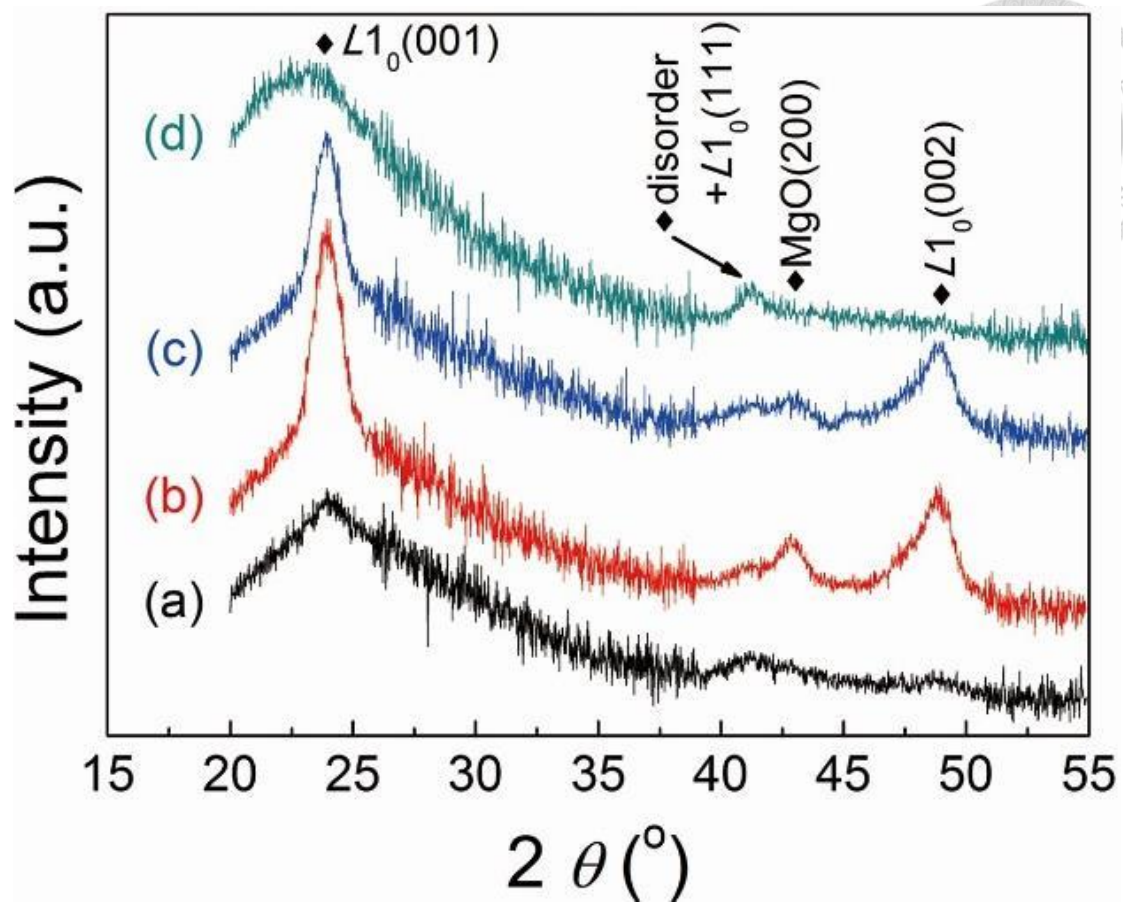


Fig. 4-12 XRD patterns for the samples of graded films with $T_d =$ (a) 300, (b) 350, (c) 400 and (d) 450°C.

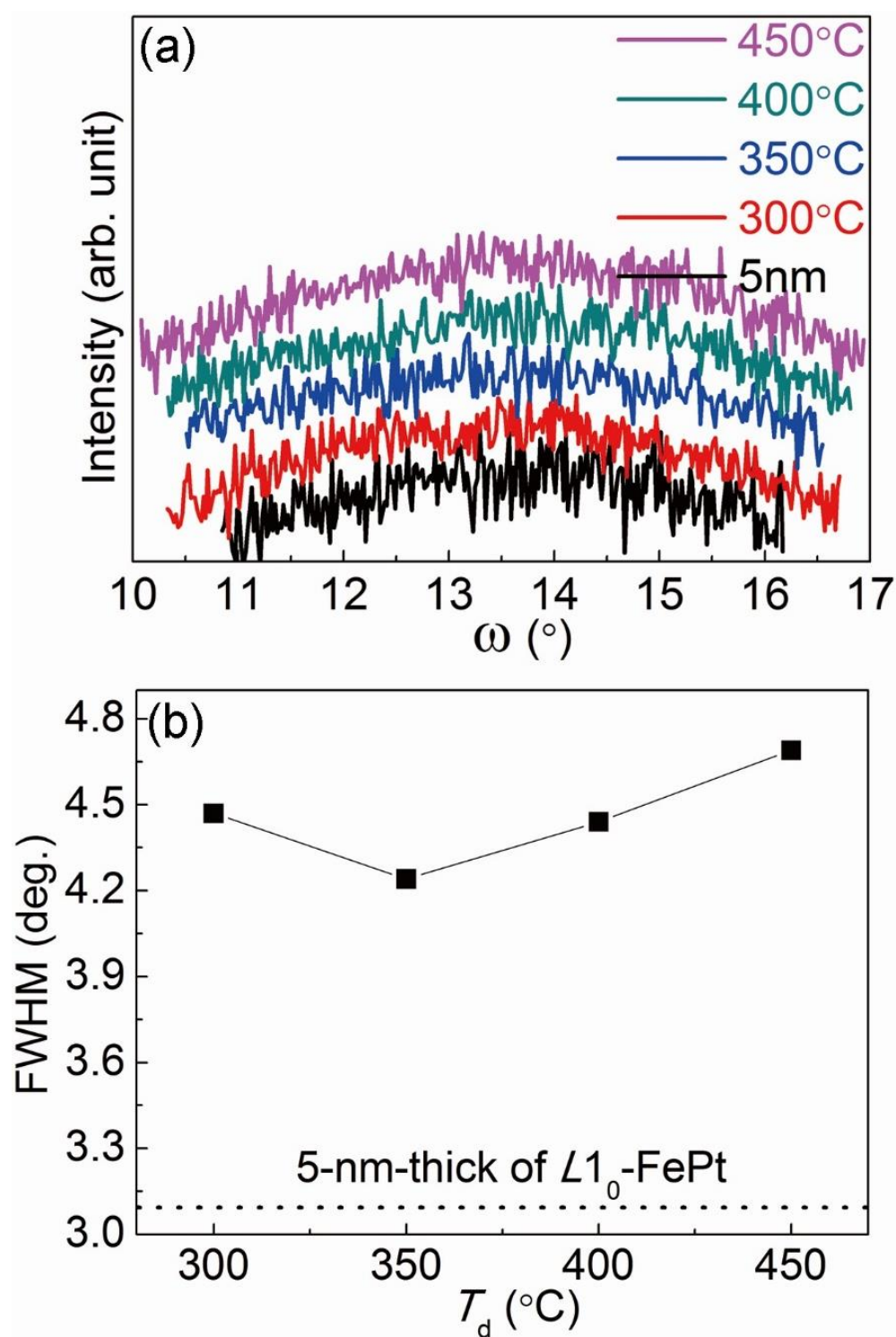


Fig. 4-13 (001)-rocking curves of 5-nm-thick $L1_0$ -FePt hard layer and the FePt(C_g)-graded layers grown at different T_d : 300, 350, 400, and 450°C (a); and their corresponding FWHM values as a function of T_d (b).

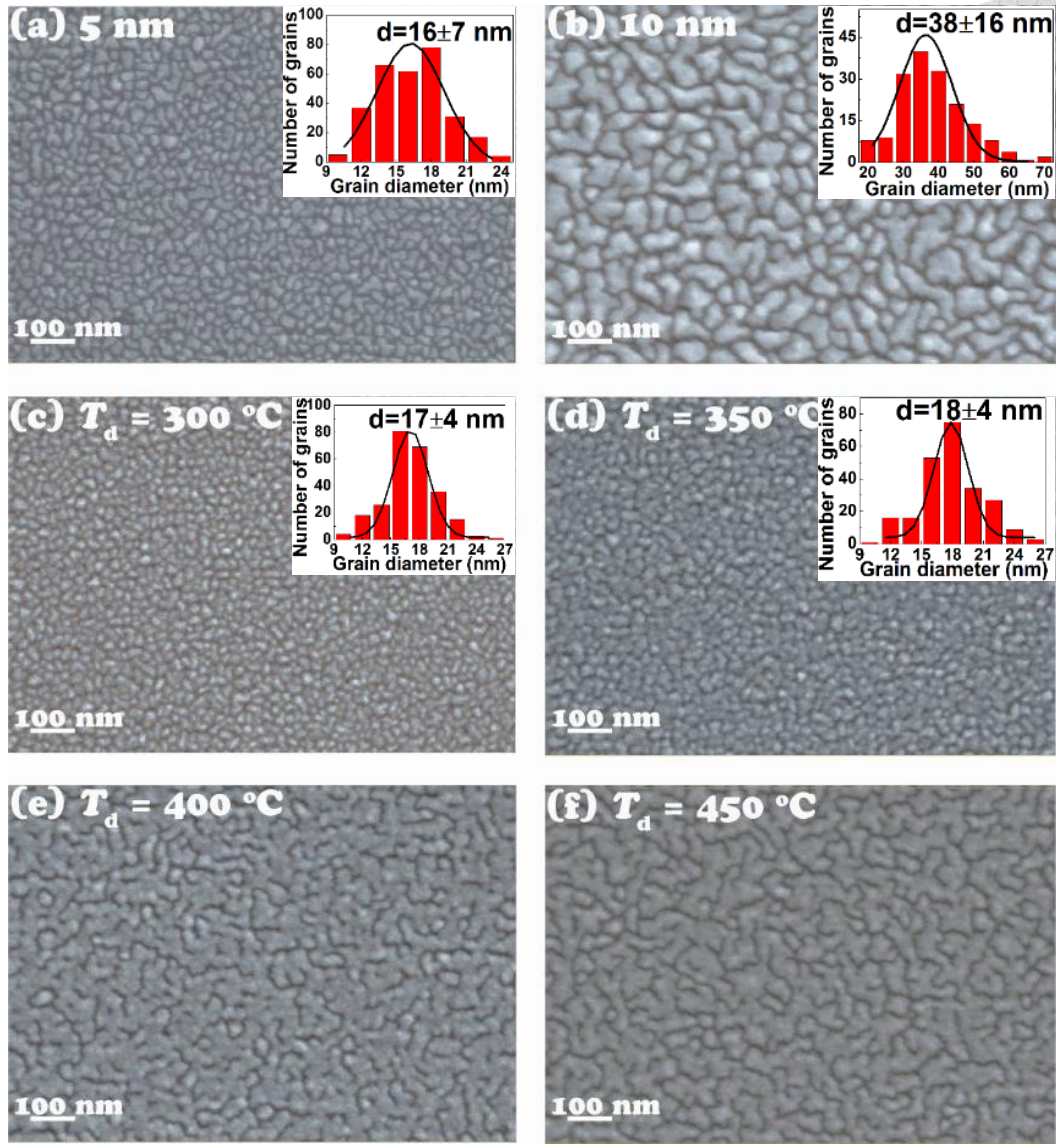


Fig. 4-14 SEM images for the samples of hard layer with thickness of (a) 5 and (b) 20 nm, graded films with $T_d =$ (c) 300, (d) 350, (e) 400, and (f) 450°C. The corresponding histograms are included in the inset of each figure.

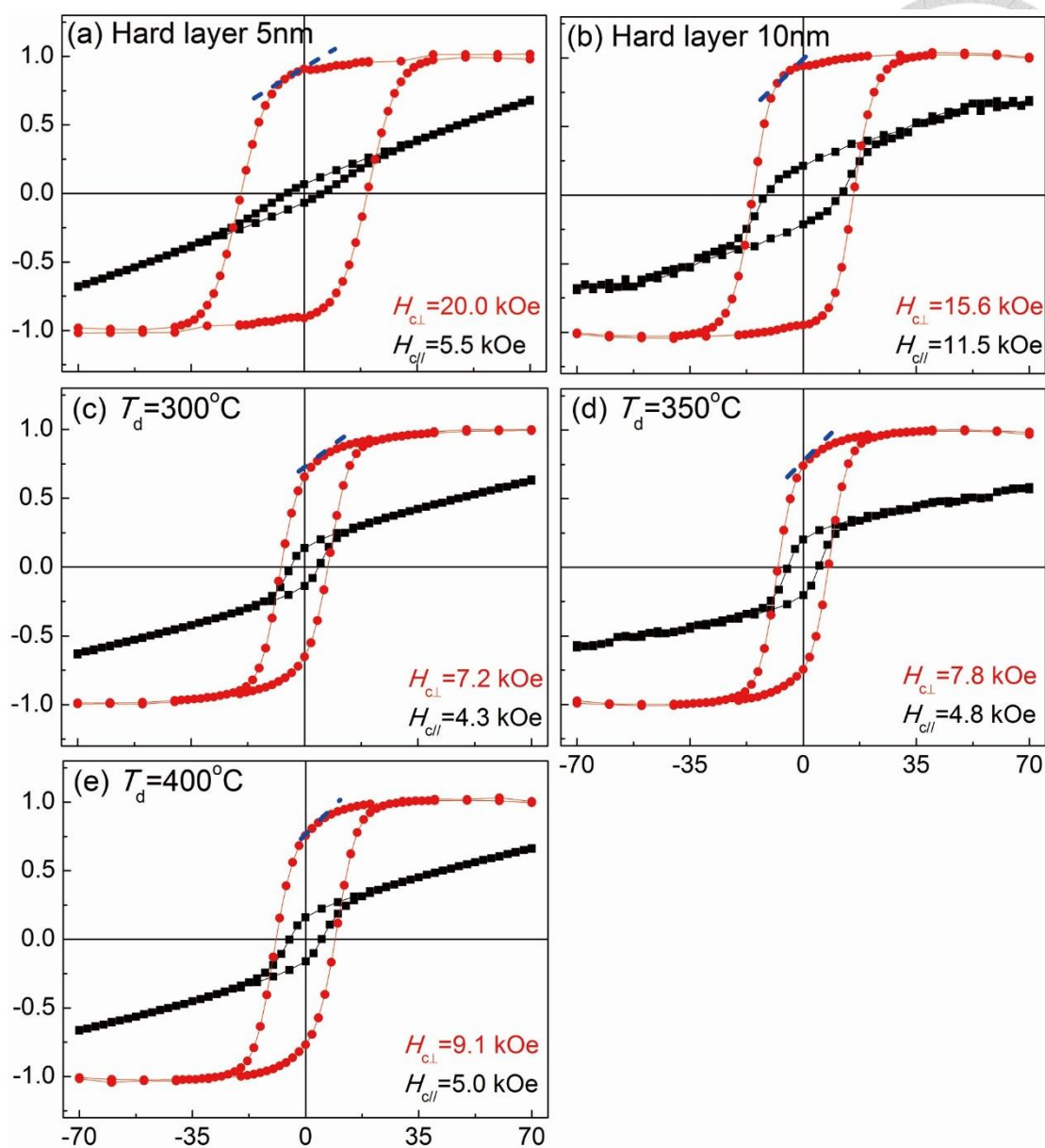


Fig. 4-15 In-plane and out-of-plane hysteresis loops for the samples of (a) 5-nm-thick and (b) 10-nm-thick hard layer, graded films with $T_d =$ (c) 300, (d) 350, and (e) 400°C.

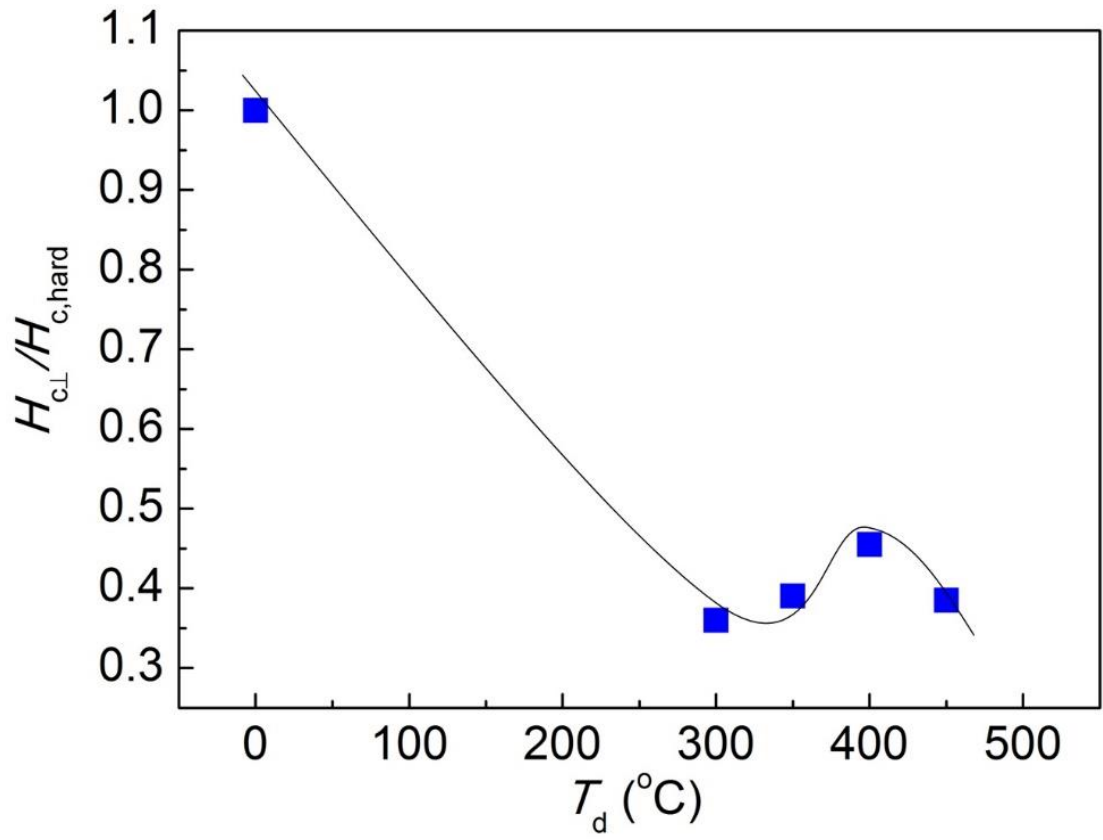


Fig. 4-16 Perpendicular coercivity, normalized to that of a 5nm-thick hard layer, as a function of T_d .

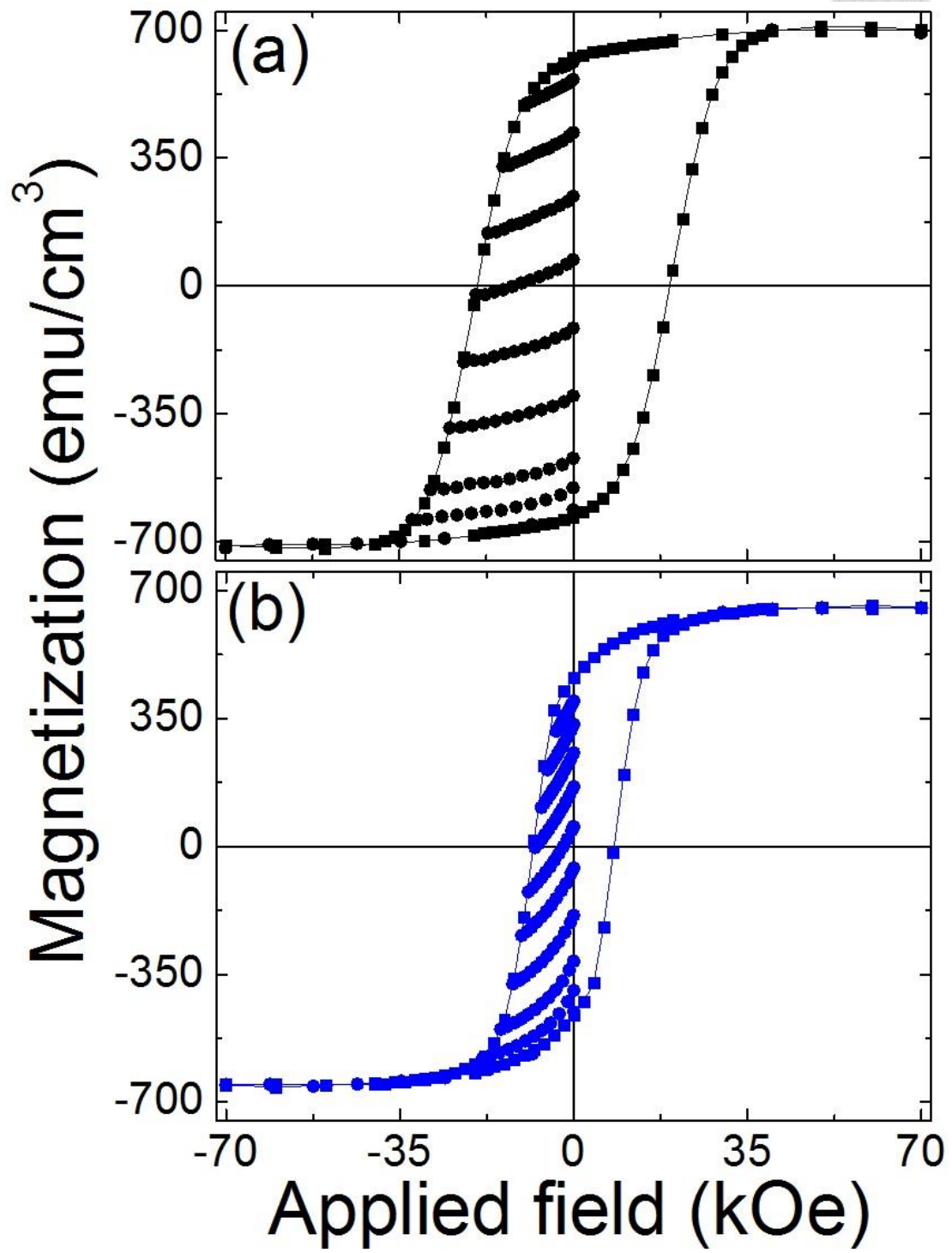


Fig. 4-17 Perpendicular hysteresis loops and recoil curves (measured by SQUID-VSM) of 5-nm-thick $L1_0$ -FePt (a) and C_g -FePt with $T_d = 350^\circ\text{C}$ (b).

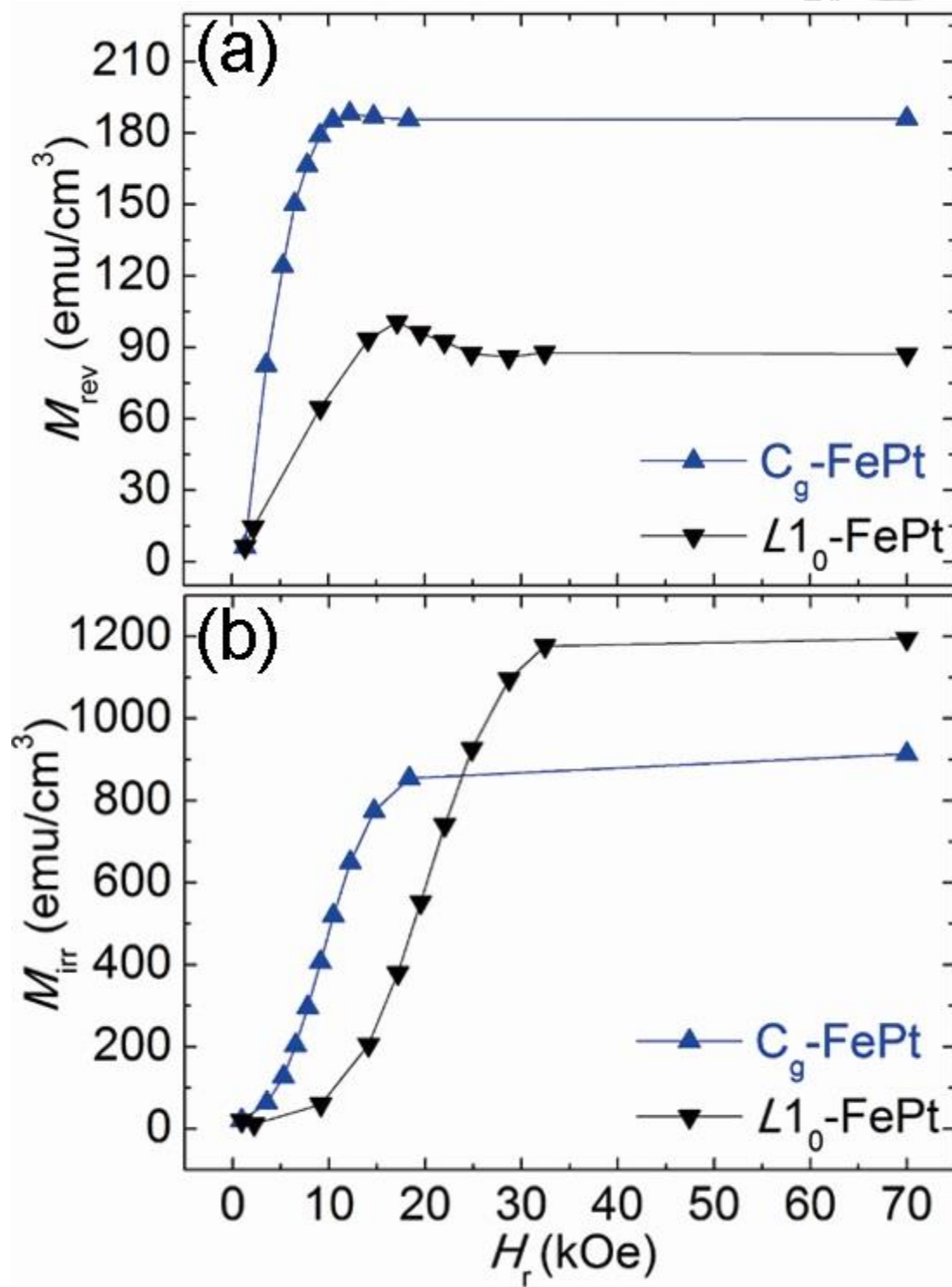


Fig. 4-18 Reversible (a) and irreversible magnetization (b) as a function of the applied reversal field (H_r) for 5-nm-thick $L1_0$ -FePt and C_g -FePt with $T_d = 350^\circ\text{C}$.

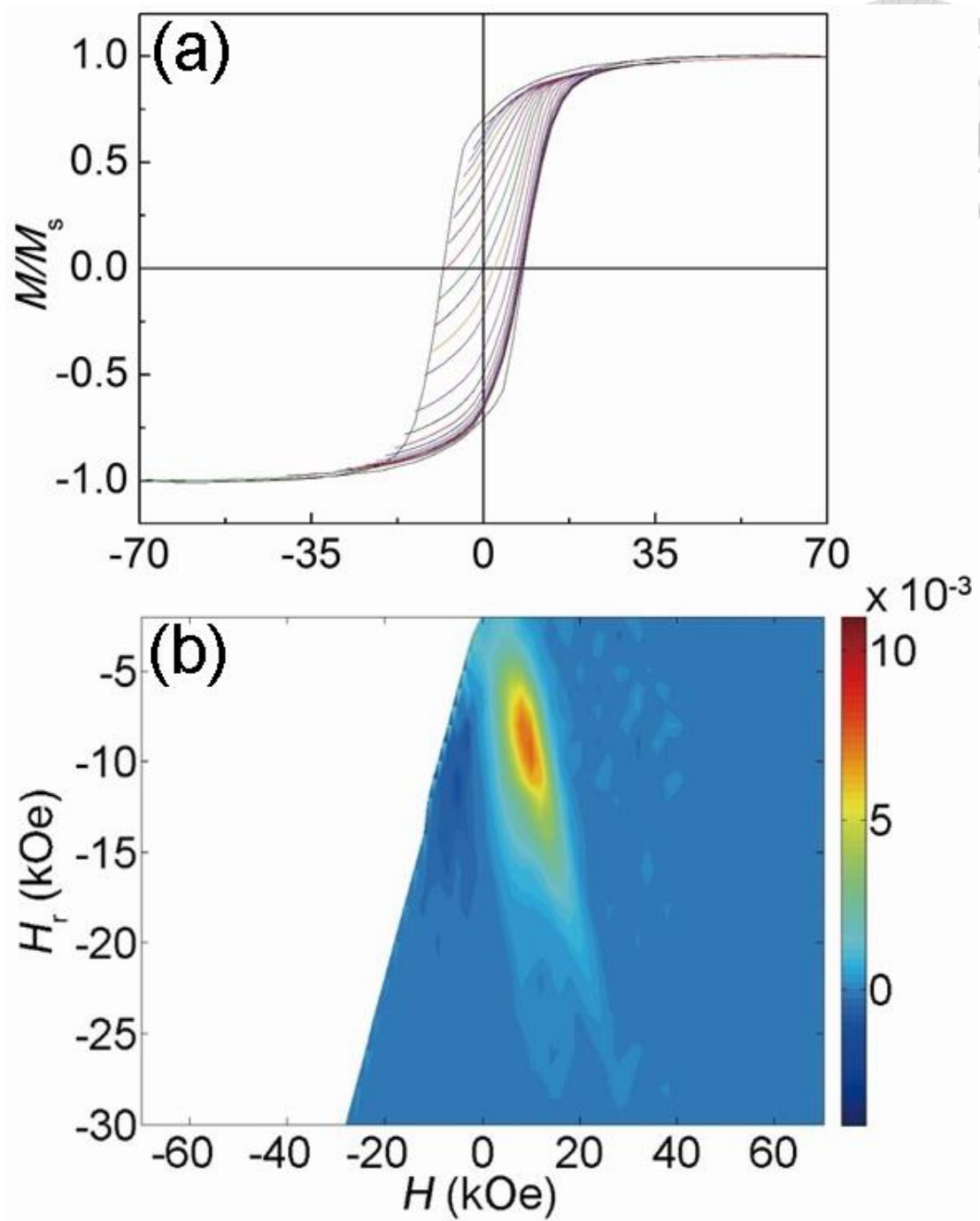


Fig. 4-19 Families of FORC's of C_g-FePt with $T_d = 350^\circ\text{C}$ (a) and the corresponding FORC distribution (b).

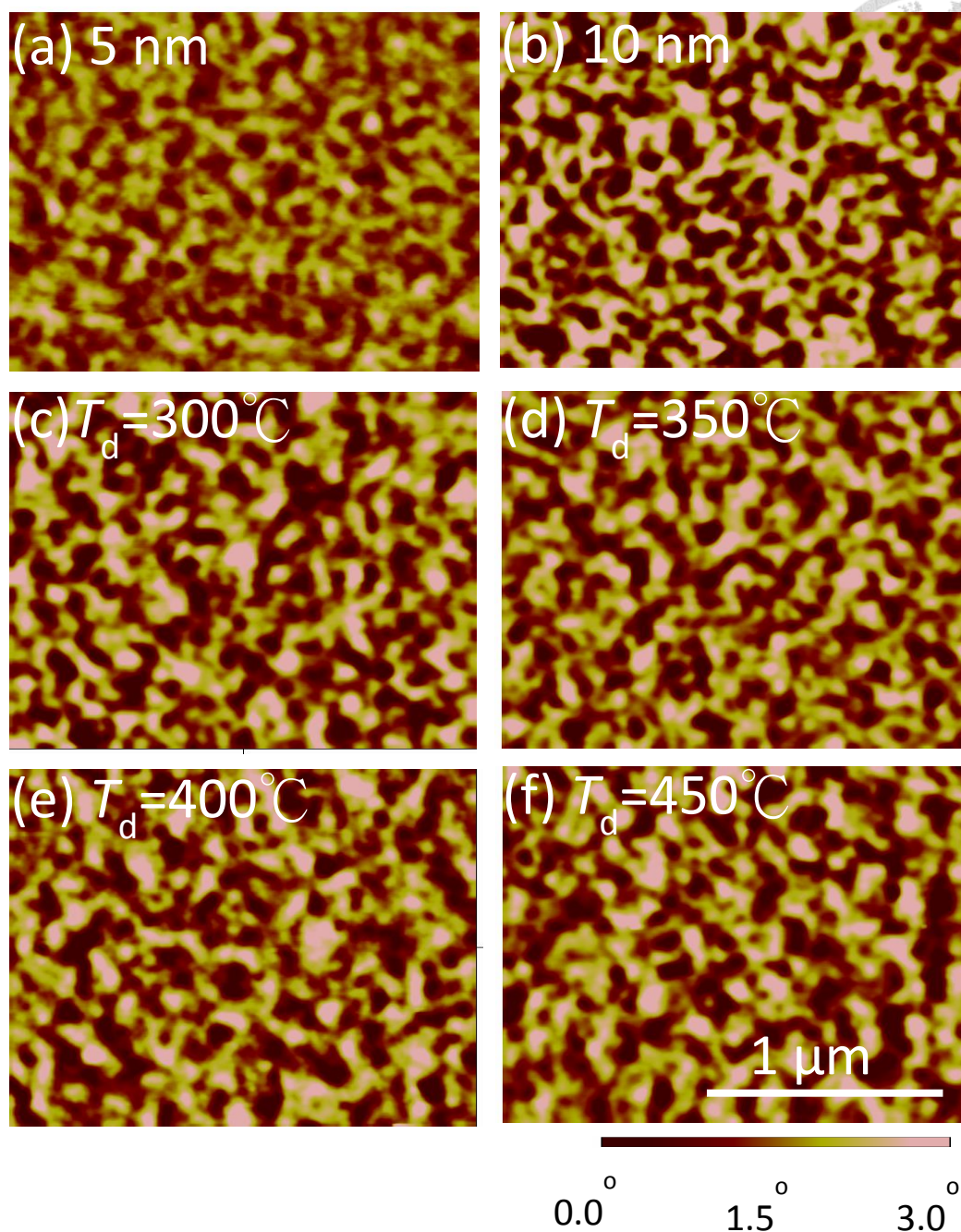


Fig. 4-20 MFM images for the samples of hard layer with thickness of (a) 5, and (b) 10, graded films with T_d = (c) 300, (d) 350, (e) 400, and (f) 450°C.

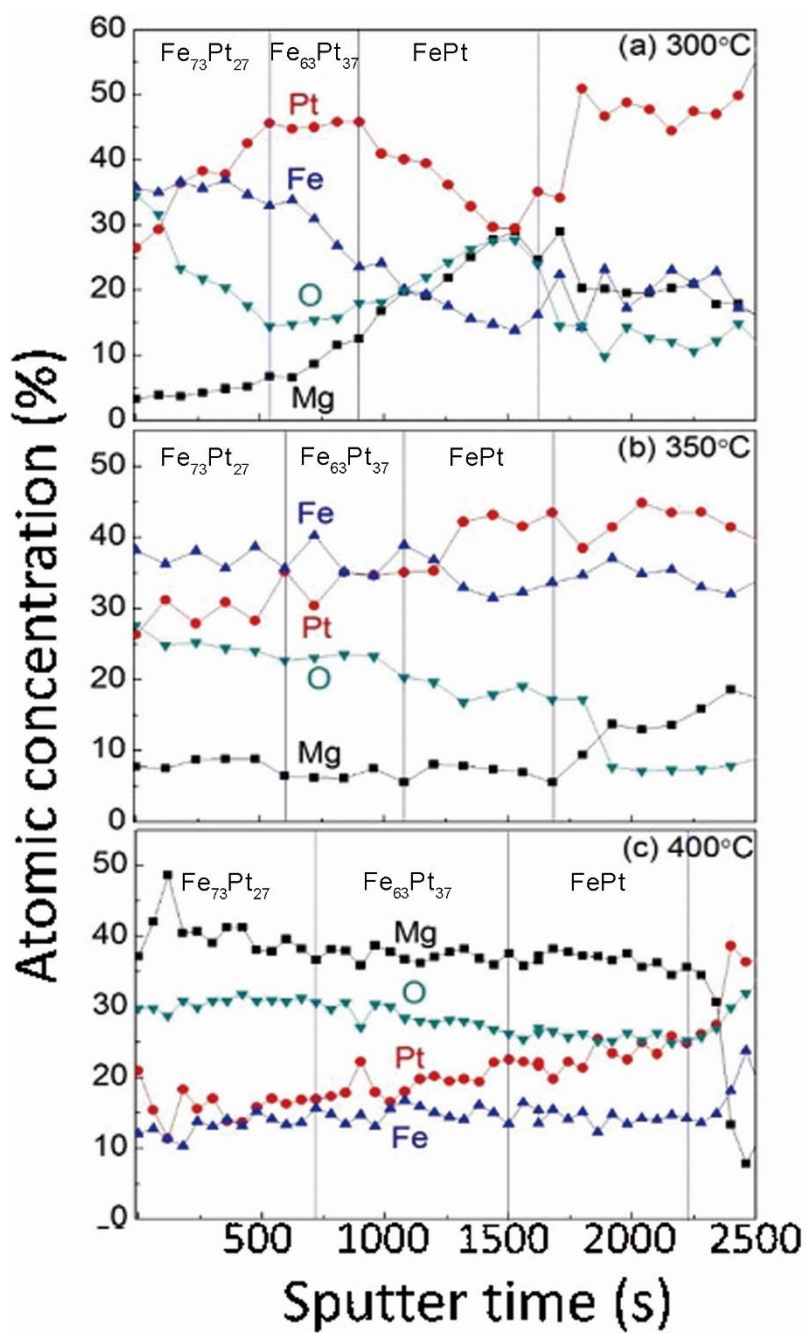


Fig. 4-21 The AES depth profile of graded films with $T_d =$ (a) 300, (b) 350, (c) and 400°C. The vertical lines are the layer boundaries between each layer.

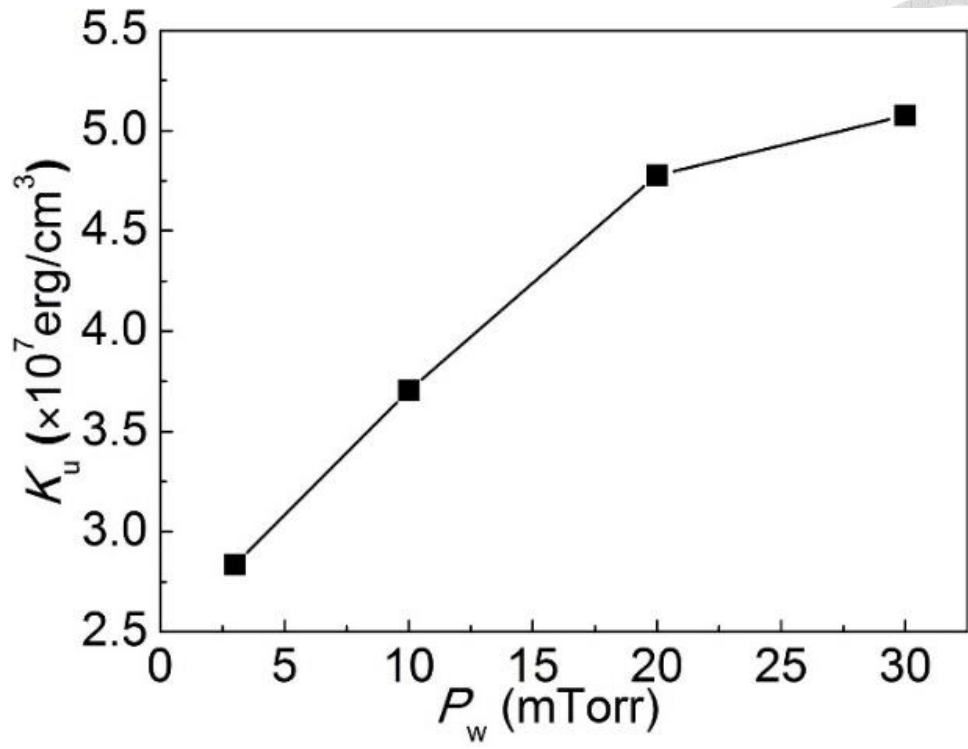


Fig. 4-22 K_u as a function of P_w for the MgO/FePt films.

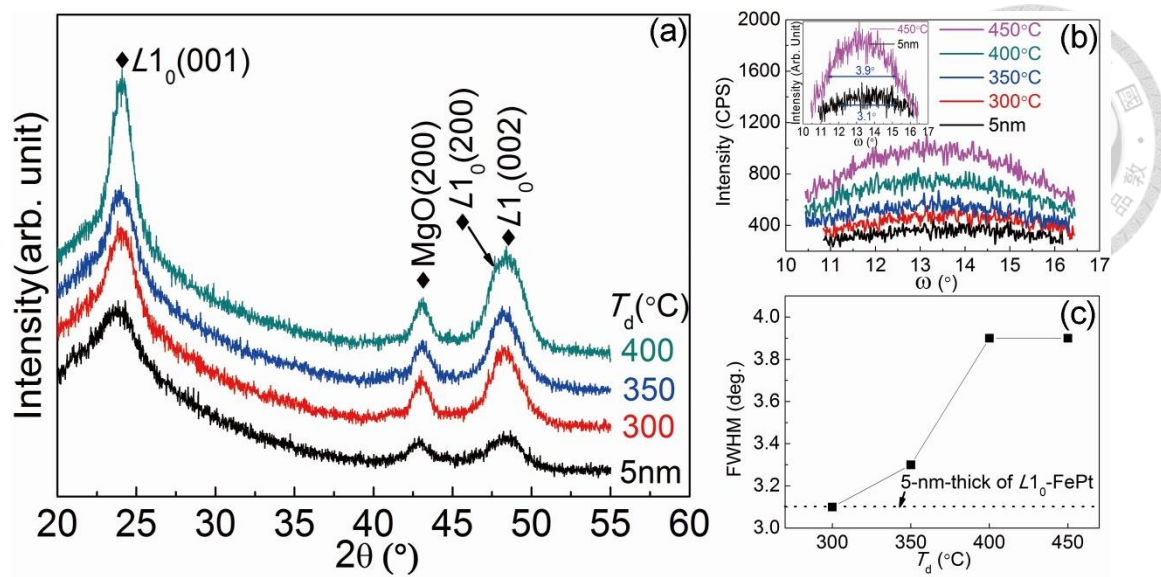


Fig. 4-23 XRD patterns of 5nm-thick $L1_0$ -FePt hard layer and the FePt(P_g)-graded layers grown at different T_d : 300, 350, and 400°C (a); and their corresponding (001)-rocking curve (b) and FWHM values as a function of T_d (c).

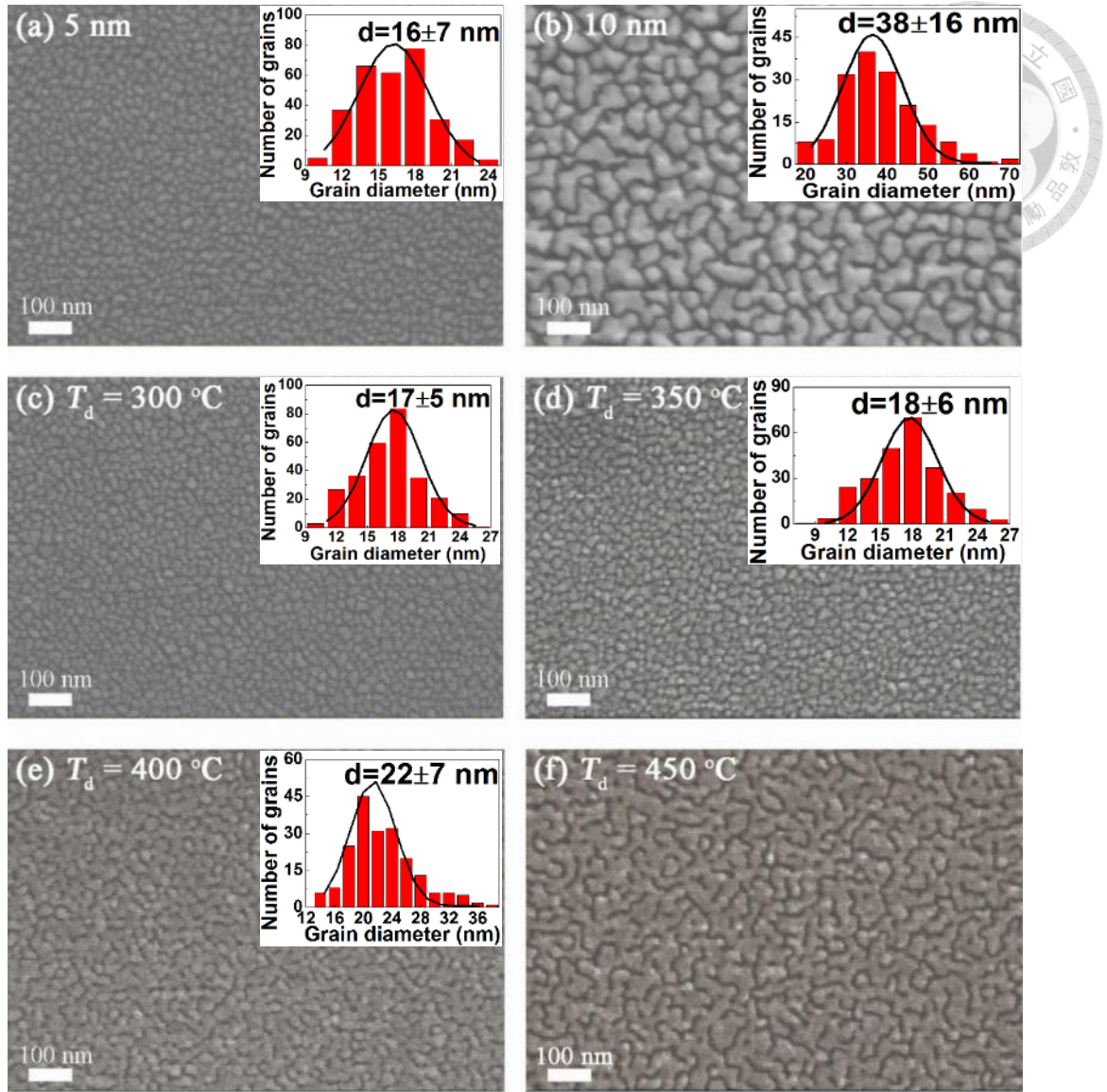


Fig. 4-24 SEM images of $L1_0$ -FePt hard layer with two different thicknesses: (a) 5 nm (b) 10 nm and the FePt(P_g)-graded structures grown at different T_d : 300 (c), 350 (d), 400 (e) and 450°C (f). The corresponding histograms are included in the inset of each figure.

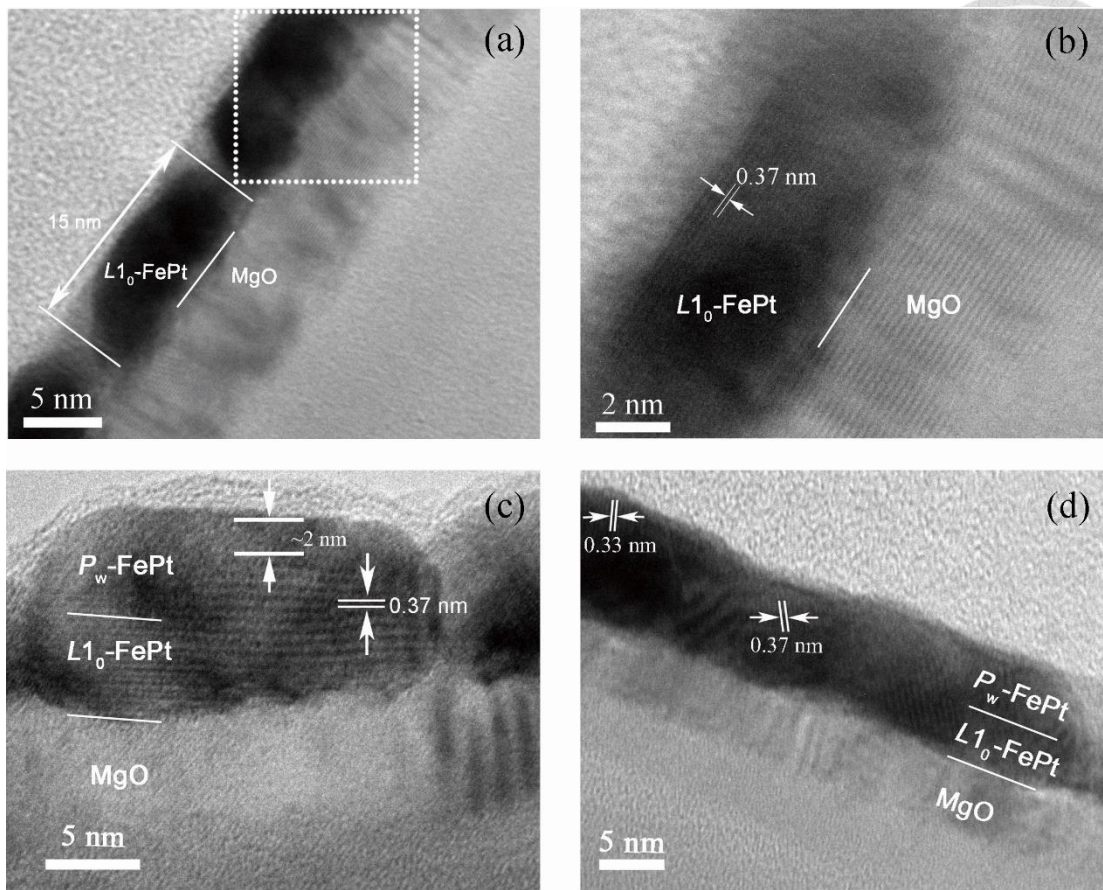


Fig. 4-25 Cross-sectional TEM images of (a) 5nm $L1_0$ -FePt hard layer, and (b) the magnified image from FePt/MgO interface in Fig. 6(a), the FePt(P_g)-graded films grown at different T_d : (c) 350 and (d) 450°C .

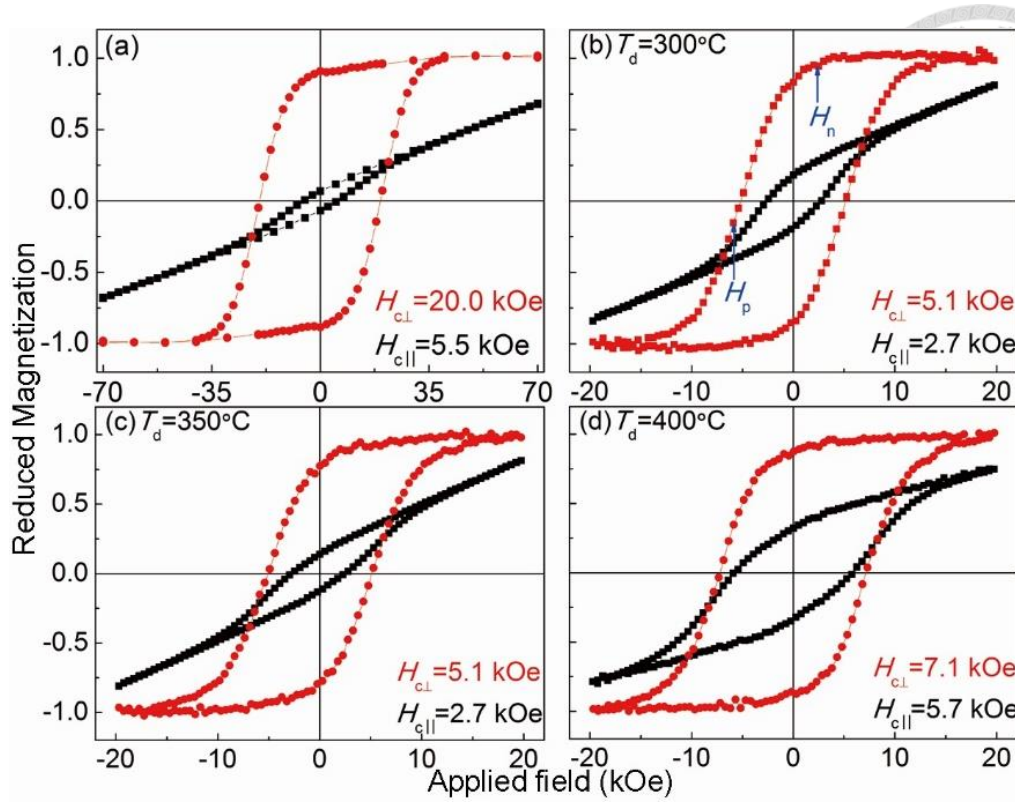


Fig. 4-26 In-plane and out-of-plane hysteresis loops for the samples of 5-nm thick FePt hard layer (a), and the FePt(P_g)-graded films grown at different T_d : 300 (b), 350 (c), 400°C (d).

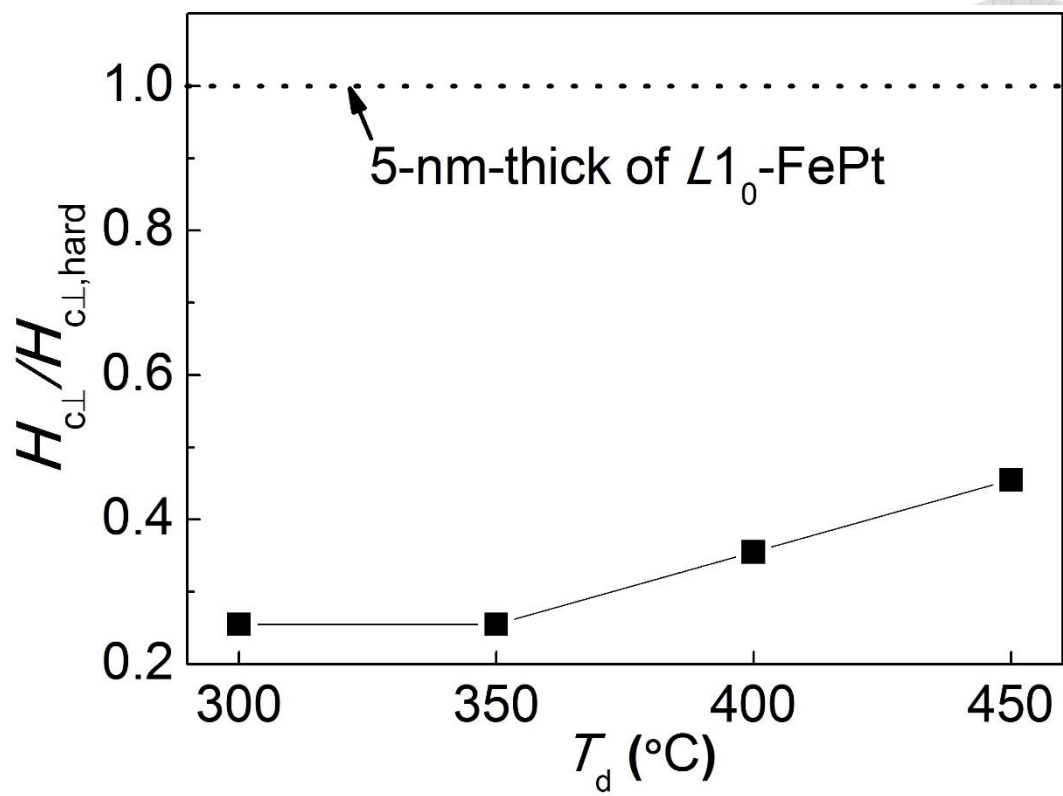


Fig. 4-27 $H_{c\perp}/H_{c\perp,hard}$ as a function of T_d for the FePt(P_g)-graded films.

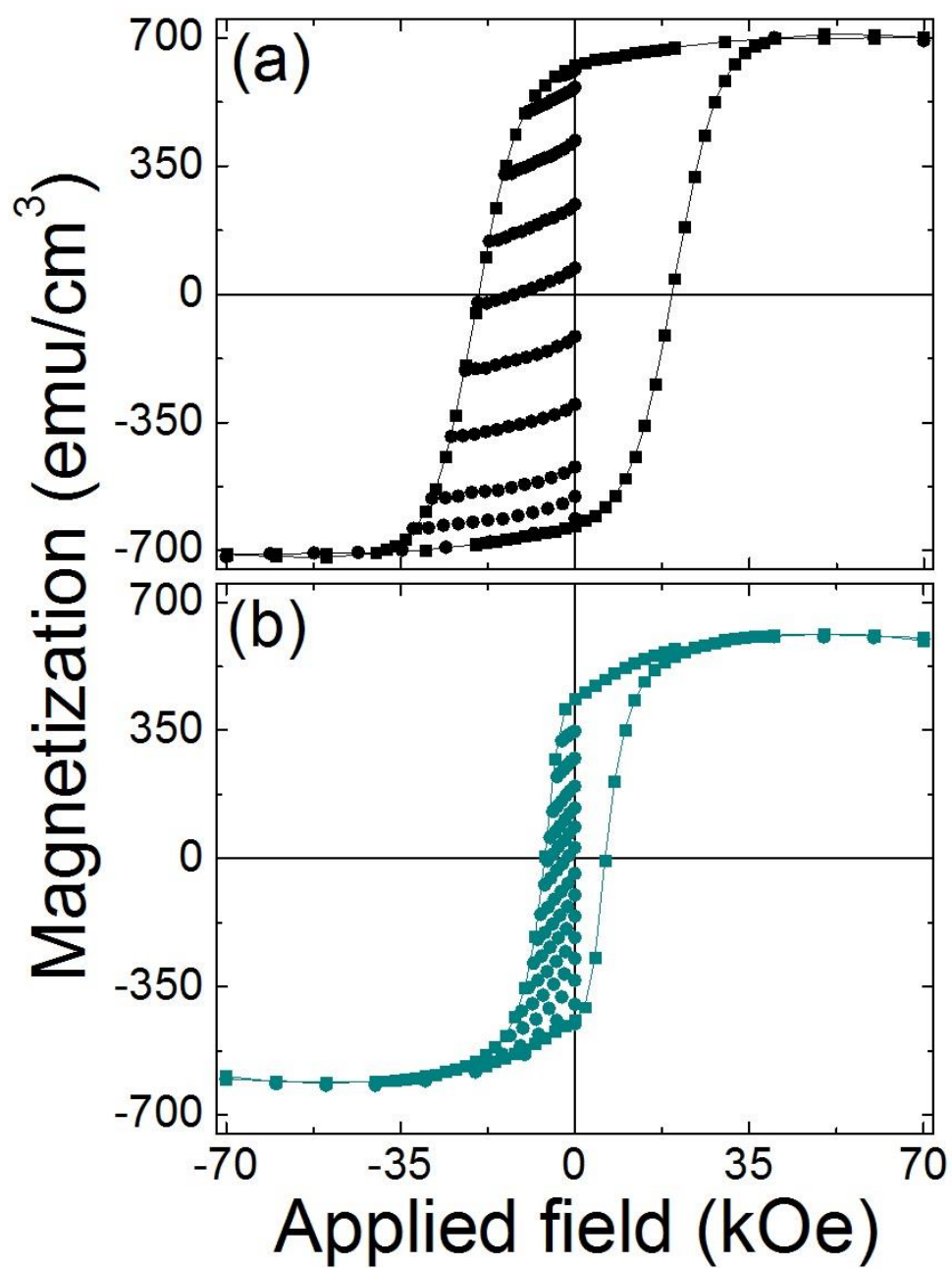


Fig. 4-28 Perpendicular hysteresis loops and recoil curves (measured by SQUID-VSM) of 5-nm-thick L_{10} -FePt (a) and P_g -FePt with $T_d = 350^\circ\text{C}$ (b).

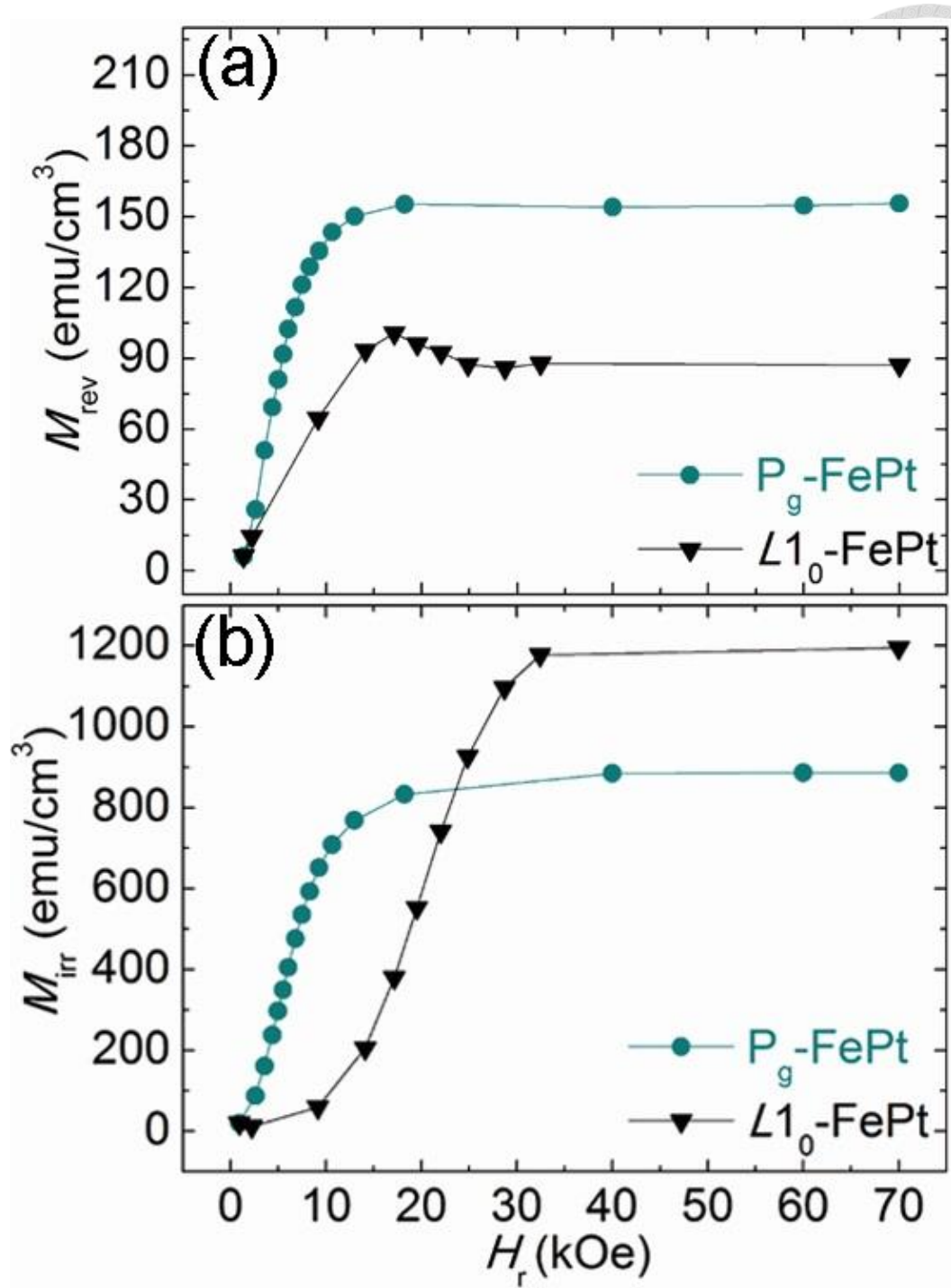


Fig. 4-29 Reversible (a) and irreversible magnetization (b) as a function of the applied reversal field (H_r) for 5-nm-thick $L1_0$ -FePt and P_g -FePt with $T_d = 350^\circ\text{C}$.

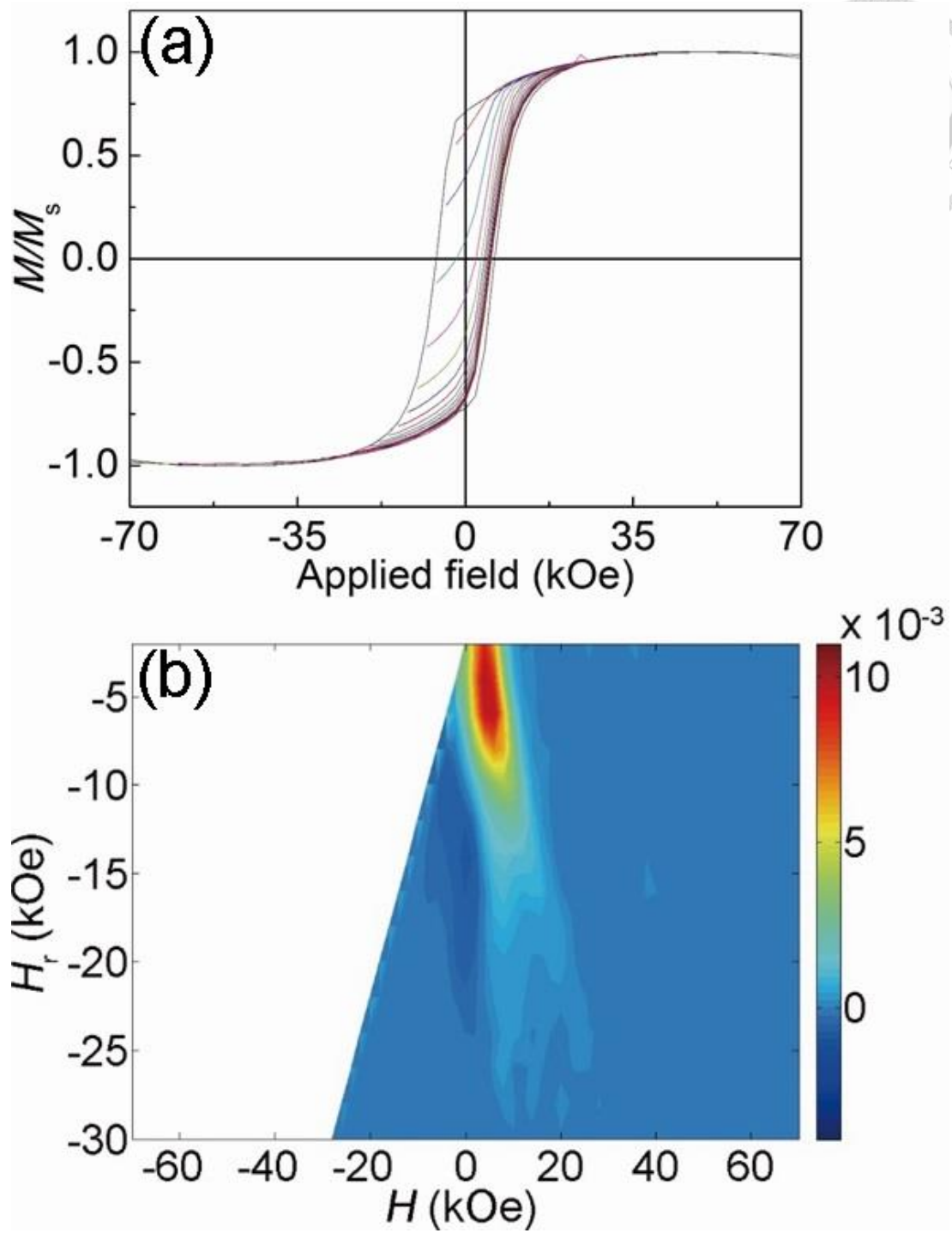


Fig. 4-30 Families of FORC's of P_g -FePt with $T_d = 350^\circ\text{C}$ (a) and the corresponding FORC distribution (b).

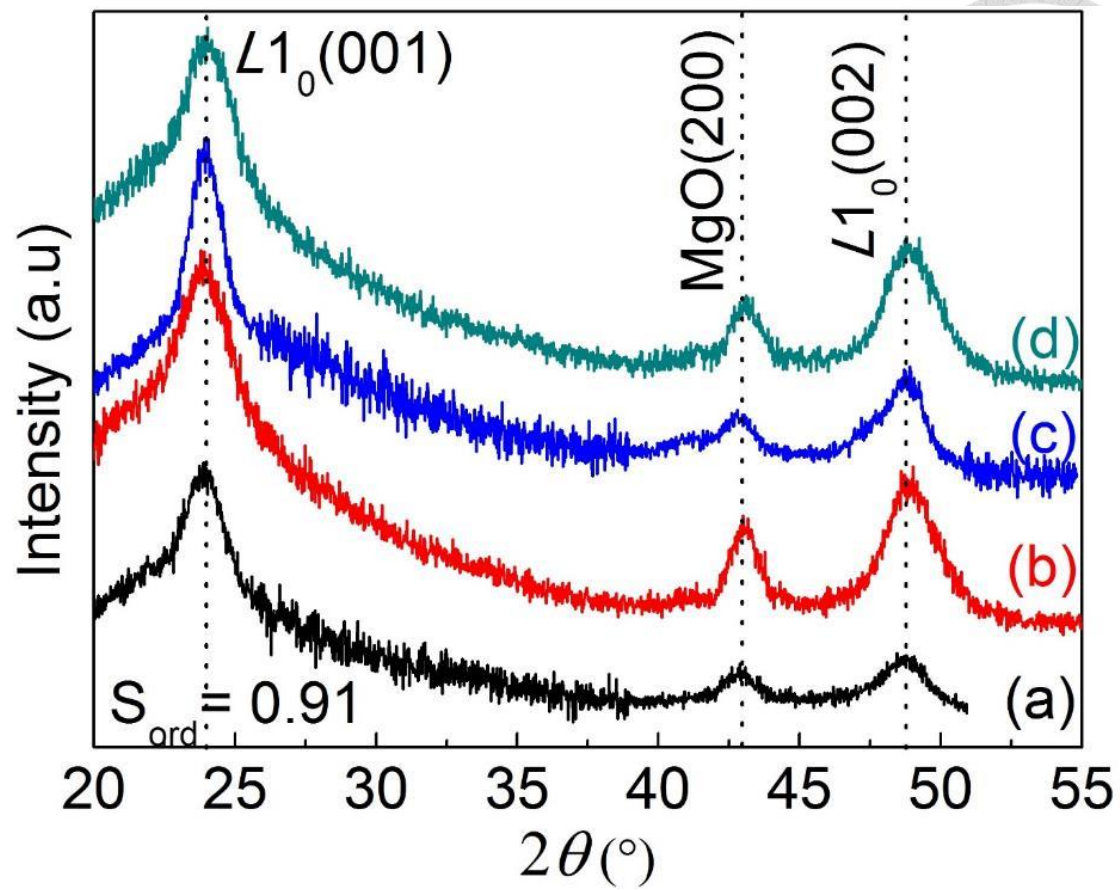


Fig. 4-31 XRD patterns for the samples of (a) 5-nm-thick hard layer, graded films of T_g -FePt with $t_g = 5$ nm (b), C_g -FePt deposited at $T_d = 350^{\circ}\text{C}$ (c), and P_g -FePt deposited at $T_d = 350^{\circ}\text{C}$ (d).

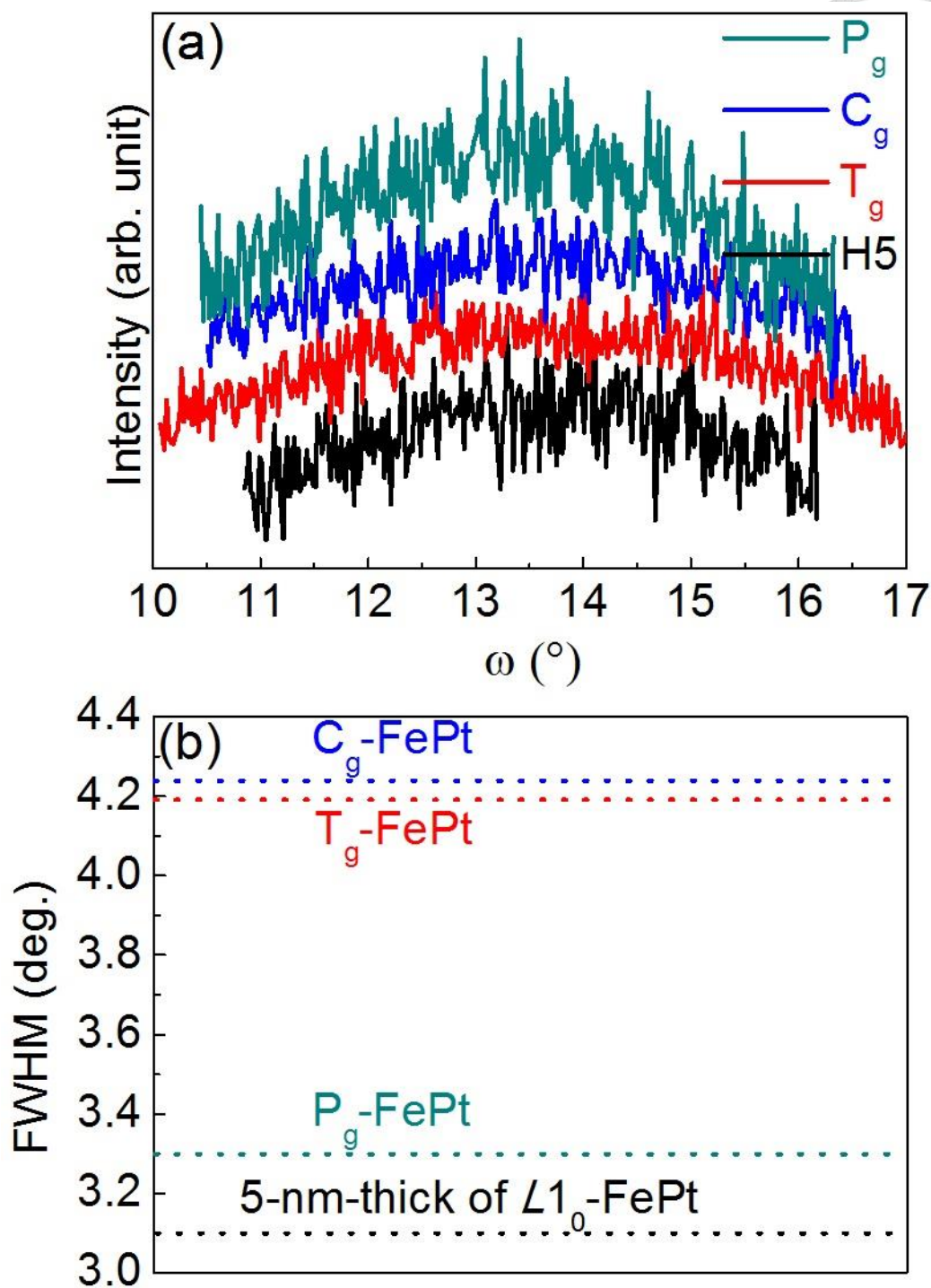


Fig. 4-32 (001)-rocking curves of 5-nm-thick $L1_0$ -FePt hard layer and the T_g -FePt grown at t_g : 5nm, C_g - and P_g -FePt grown at $T_d = 350^\circ\text{C}$ (a); and their corresponding FWHM values as a function of t_g (b).

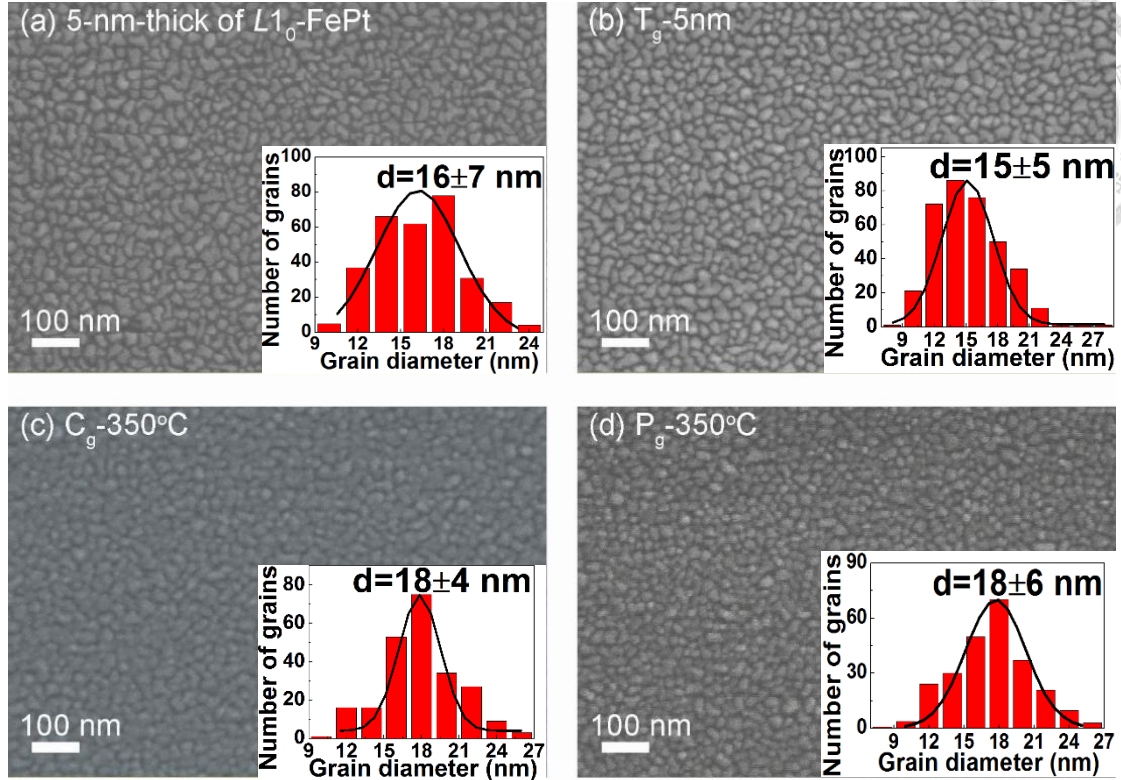


Fig. 4-33 SEM images for the samples of hard layer with thickness of (a) 5 nm, graded films of T_g -FePt with $t_g = 5$ nm (b), C_g -FePt deposited at $T_d = 350^\circ\text{C}$ (c), and P_g -FePt deposited at $T_d = 350^\circ\text{C}$ (d). The corresponding histograms are included in the inset of each figure.

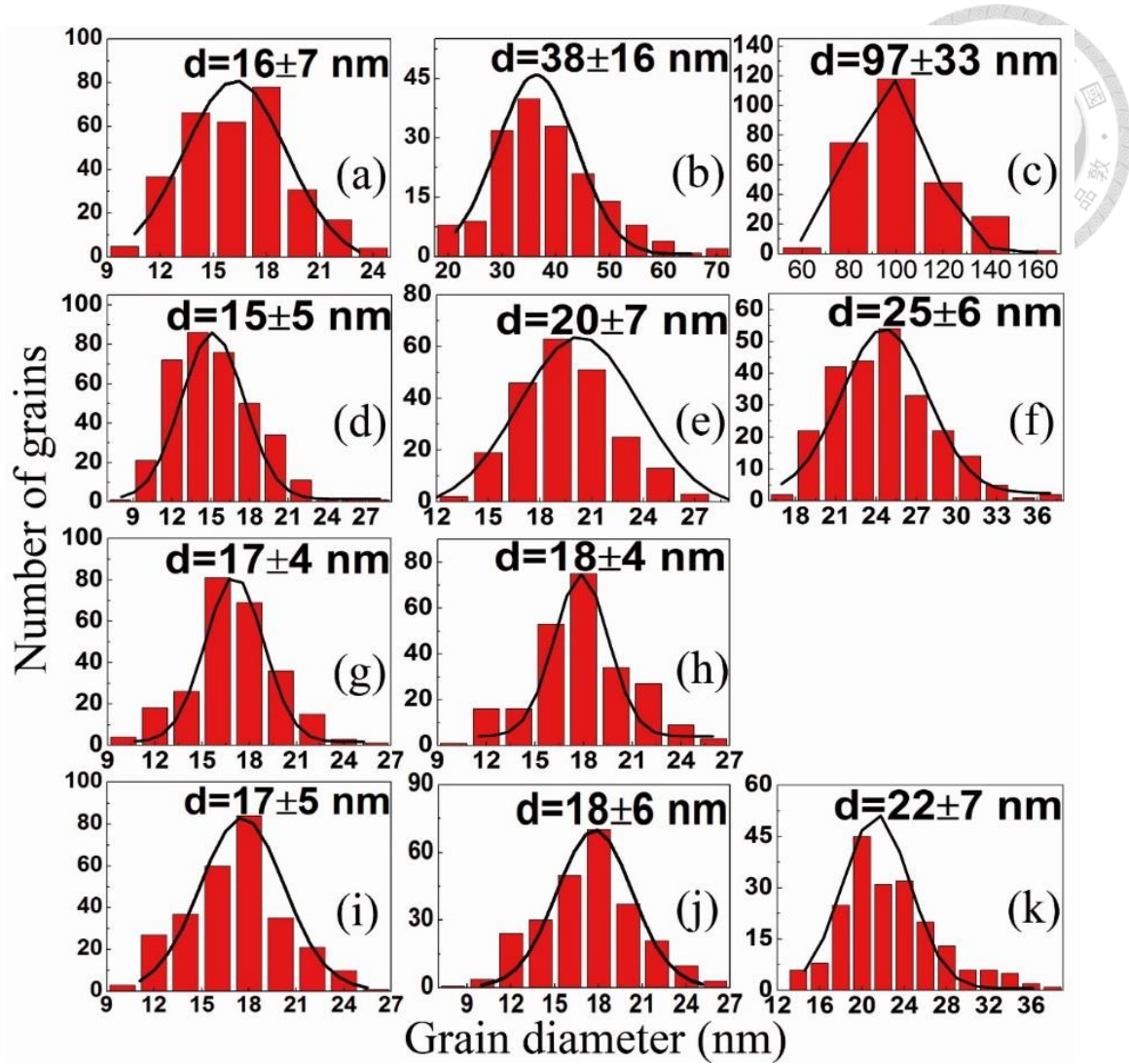


Fig. 4-34 Grain size distribution of $L1_0$ -FePt: 5nm (a), 10nm (b), 20nm (c); temperature graded FePt: $t_g = 5$ nm (d), 10nm (e), 15nm (f); composition graded FePt: $T_d = 300^\circ\text{C}$ (g), 350°C (h); pressure graded FePt: $T_d = 300^\circ\text{C}$ (i), 350°C (j), 400°C (k).

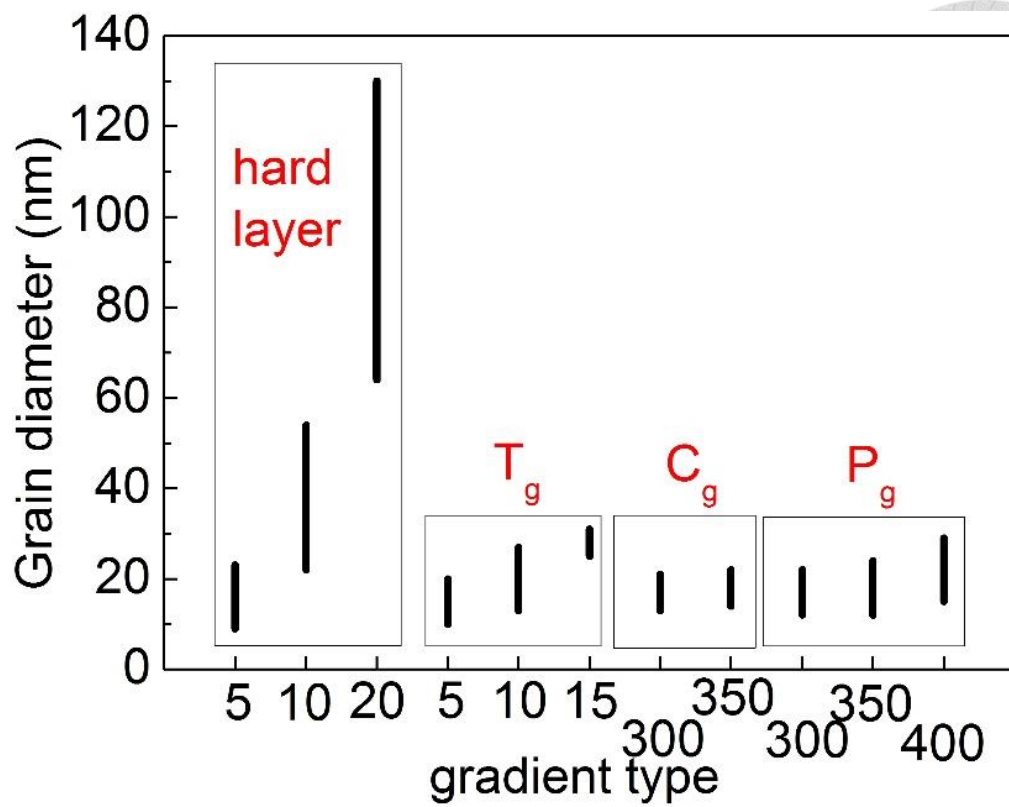


Fig. 4-35 Grain size distribution of island-like structure: $L1_0$ -FePt, temperature graded FePt (T_g), composition graded FePt (C_g), and pressure graded FePt (P_g).

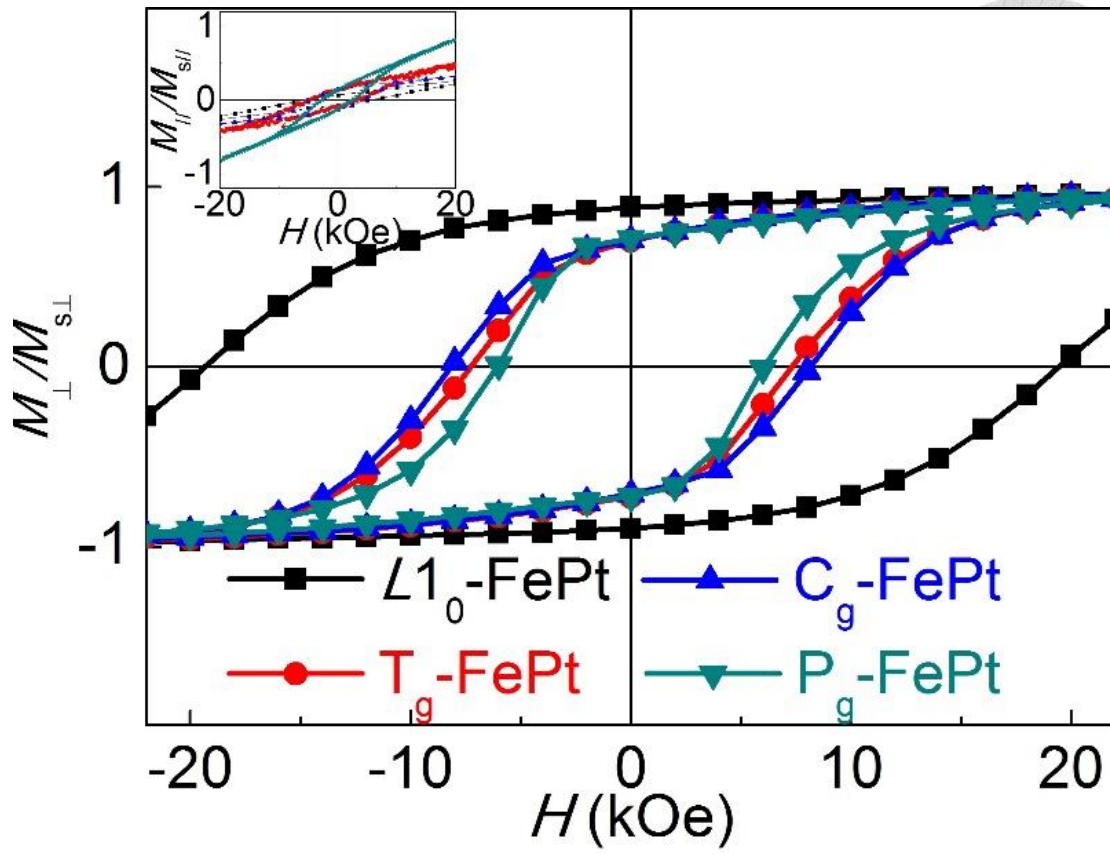


Fig. 4-36 Out-of-plane hysteresis loops for the $L1_0$ -FePt and three graded FePt structures, with an insert shows their corresponding in-plane hysteresis loops.

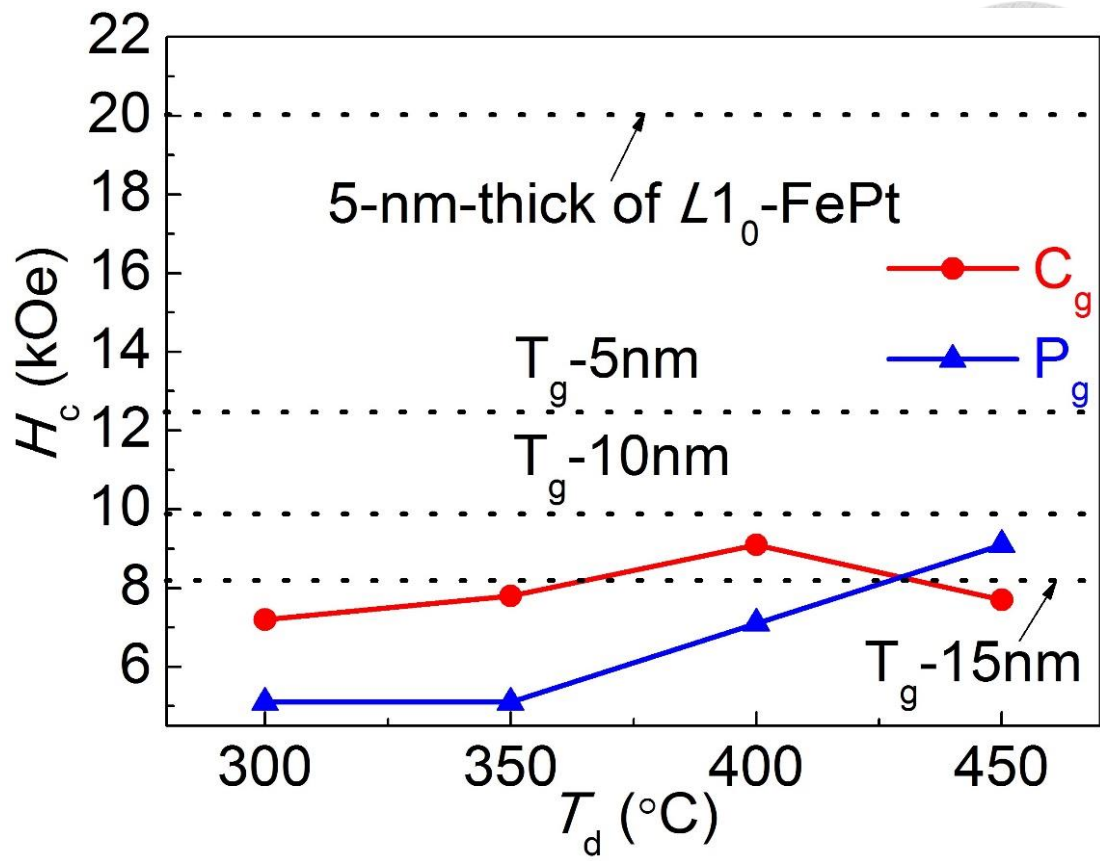


Fig. 4-37 Perpendicular coercivity as a function of T_d (C_g and P_g).

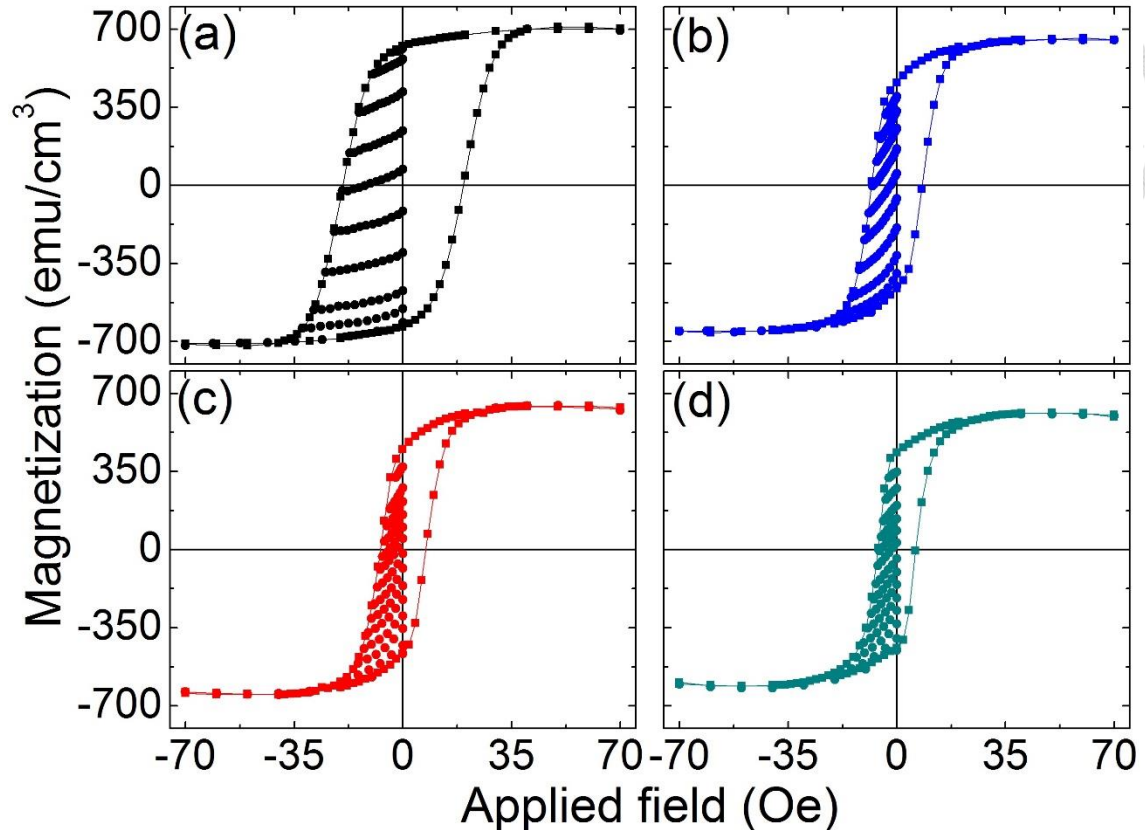


Fig. 4-38 Perpendicular hysteresis loops and recoil curves (measured by SQUID-VSM) of 5-nm-thick $L1_0$ -FePt (a), C_g -FePt (b), T_g -FePt (c), and P_g -FePt (d).

The recoil curves were measured along the demagnetizing portion from $H = -H_{\max}$ to $H = 0$ and back to $H = -H_{\max}$.

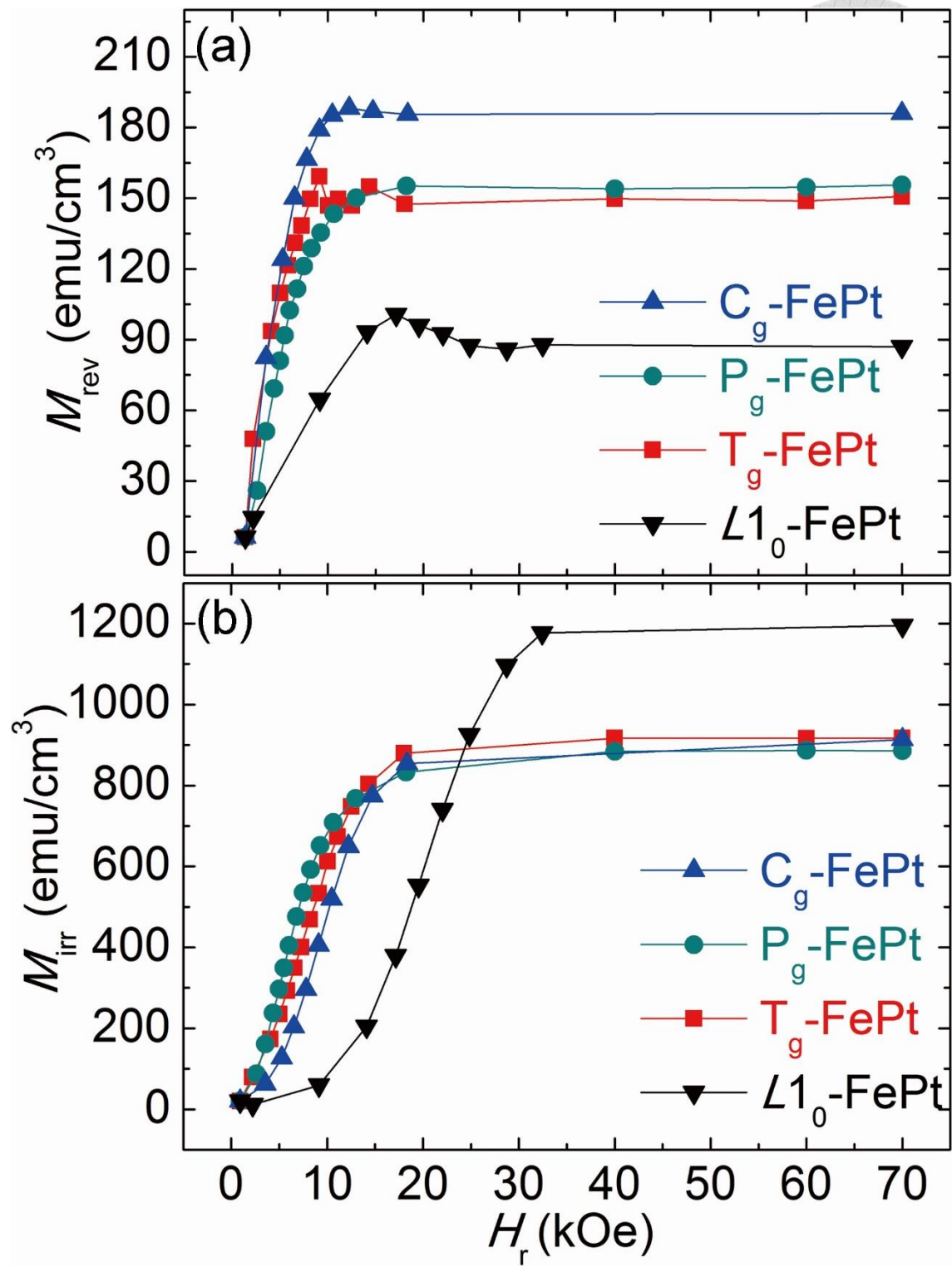


Fig. 4-39 Reversible (a) and irreversible magnetization (b) as a function of the applied reversal field (H_r) for $L1_0$ -FePt, C_g -FePt, T_g -FePt, and P_g -FePt.

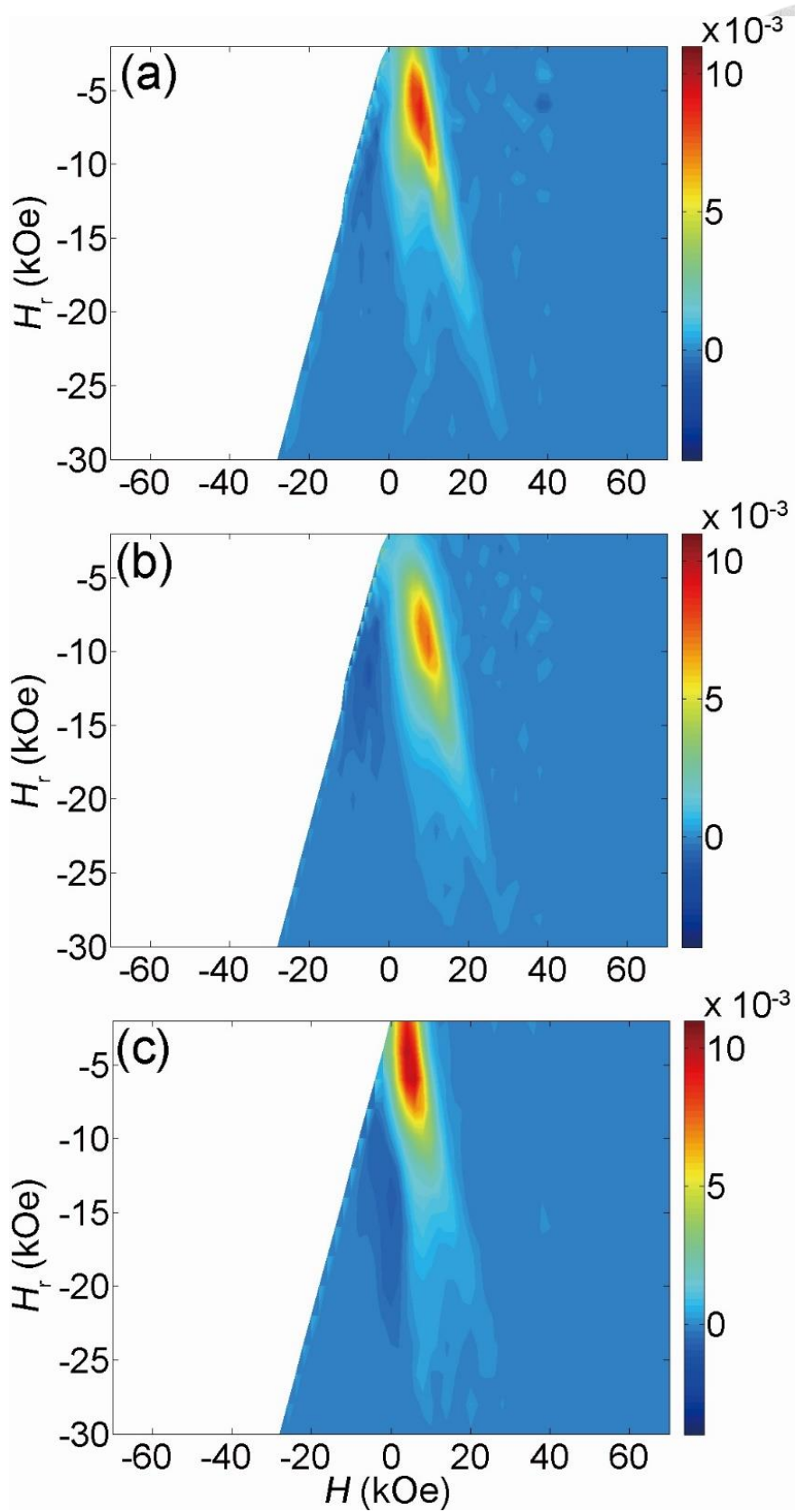


Fig. 4-40 FORC distribution of T_g -FePt (a), C_g -FePt (b), and P_g -FePt (c).

Chapter 5

Conclusions



1. Grain size and separating distance are almost the same between different gradient systems. However, the size distribution of composition graded film is the lowest one than the other two gradient system.
2. In the opinion of switching field, pressure gradient media shows a larger reduction (- 3.3 times), a larger effect than in other two gradient system.
3. Assuming the switching field is acceptable, temperature graded film is the optimum condition due to the maximum ratio of $H_{c\perp}/H_{c\parallel}$.
4. Considering to reduce the switching field and magnetic reversal, P_g-FePt film may has the best gradient performance among these three structures.

References



- [1] 台灣資訊儲存技術協會，vol. 6， p.3 (2005)。
- [2] http://en.wikipedia.org/wiki/Magnetic_tape
- [3] 台灣資訊儲存技術協會，vol. 6， p.5 (2005)。
- [4] http://en.wikipedia.org/wiki/Magnetic_storage
- [5] H. N. Bertram, H. Zhou, and R. Gustafson, *IEEE Trans. Magn.* **34**, 1845 (1998).
- [6] S. H. Charap, P. L. Ku, and Y. He, *IEEE Trans. Magn.* **33**, 978 (1997).
- [7] D. Weller and A. Moser, *IEEE Trans. Magn.* **35**, 4423 (1999).
- [8] 沈智隆，”博士論文：鐵鉑添加陶磁材料之顆粒狀薄膜的磁性質及微結構研究”，國立台灣大學，p.6 (1999)。
- [9] Dieter Weller, Andreas Moser, Liesl Folks, Margaret E. Best, Wen Lee, Mike F. Toney, M. Schwickert, Jan-Ulrich Thiele, and Mary F. Doerner, *IEEE Trans. Magn.* **36** (2000).
- [10] 台灣資訊儲存技術協會， vol. 6， p.33 (2005)。
- [11] S. Khizroev and D. Litvinov, *J. Appl. Phys.* **95**, 4521 (2004).
- [12] S. Iwasaki and K. Takemura, *IEEE Trans. Magn.* **1173** (1975).
- [13] D. Weller, H. Brandle, G. Gorman, C. J. Lin, and H. Notravs, *Appl. Phys. Lett.* **61**, 2726 (1992).
- [14] S. N. Piramanayagam, *J. Appl. Phys.* **102**, 011301 (2007).

[15] http://en.wikipedia.org/wiki/Hard_disk_drive

[16]

http://www.computerworld.com/s/article/9225335/With_tech_breakthrough_Seagate_promises_60TB_drives_this_decade

[17] A. Takeo, Y. Takahashi, Y. Tanaka, K. Miura, H. Muraoka, and Y. Nakamura, *J. Appl. Phys.* **87**, 4987 (2000).

[18] 沈智隆，博士論文：”鐵鉑添加陶瓷材料之顆粒狀薄膜的磁性質及微結構研究”，國立台灣大學，p.2 (2011)。

[19] S. Iwasaki, Y. Nakamura, and K. Ouchi, *IEEE Trans. Magn.* **14**, 436 (1978).

[20] Y. Hirayama, M. Futamoto, K. Kimoto, and K. Usami, *IEEE Trans. Magn.* **32**, 3807 (1996).

[21] Y. Hirayama, Y. Honda, T. Takeuchi, and M. Futamoto, *IEEE Trans. Magn.* **35**, 2766 (1999).

[22] H. Uwazumi, T. Shimatsu, Y. Sakai, A. Otsuki, I. Watanabe, H. Muraoka, and Y. Nakamura, *IEEE Trans. Magn.* **37**, 1595 (2001).

[23] J. Ariake, N. Honda, K. Ouchi, and S. Iwasaki, *IEEE Trans. Magn.* **36**, 2411 (2000).


[24] G. A. Bertero *et al.*, *IEEE Trans. Magn.* **38**, 1627 (2002).

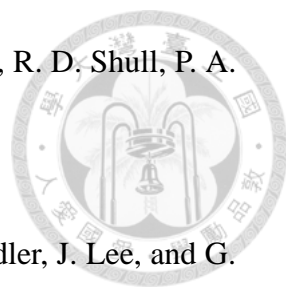
[25] N. Honda, J. Ariake, K. Ouchi, and S. Iwasaki, *IEEE Trans. Magn.* **30**, 4023

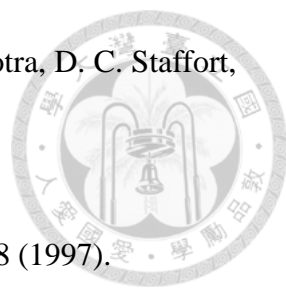


(1994).

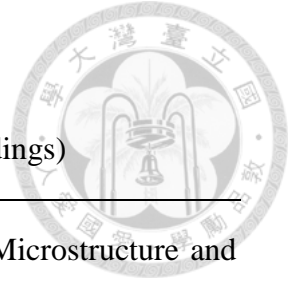
- 
- [26] N. Honda, J. Ariake, and K. Ouchi, *IEEE Trans. Magn.* **34**, 1651 (1998).
- [27] Y. Hirayama, M. Futamoto, K. Ito, Y. Honda, and Y. Maruyama, *IEEE Trans. Magn.* **33**, 996 (1997).
- [28] 金重勳，磁性技術手冊，p.172 (2002)。
- [29] K. Gao and H. N. Bertram, *IEEE Trans. Magn.* **38**, 3675 (2002).
- [30] C. H. Hee, Y. Y. Zou, and J. P. Wang, *J. Appl. Phys.* **91**, 8004 (2002).
- [31] S. Maat, O. Hellwig, G. Zeltzer, Eric E. Fullerton and G. J. Mankey, *Phys. Rev. B* **63**, 134426 (2001).
- [32] E. F. Kneller, and R. Hawing, *IEEE Trans. Magn.* **27**, 3588 (1991).
- [33] R.H. Victora and X. Shen, *IEEE Trans. Magn.* **1**, 537 (2005).
- [34] R.H. Victora and X. Shen, *IEEE Trans. Magn.* **1**, 2828 (2005).
- [35] A. Yu. Dobin and H. J. Richter, *Appl. Phys. Lett.* **89**, 062512 (2006).
- [36] Hao Wang, Weimin Li, M. Tofizur Rahman, Haibao Zhao, Jun Ding, Yunjie Chen, and Jian-Ping Wang, *J. Appl. Phys.* **111**, 07B914 (2012).
- [37] H. Kronmuller and D. Goll, *Physica B* **319**, 122 (2002).
- [38] D. Suess, *Appl. Phys. Lett.* **89**, 113105 (2006).
- [39] Jun Zhang, Yang Liu, Fang Wang, Jing Zhang, Ruiqiang Zhang, Zhenfeng Wang, and Xiaohong Xu, *J. Appl. Phys.* **111**, 073910 (2012).

- 
- [40] A. Dobin and H. J. Richter, e-print cond-mat/0605368.
- [41] F. B. Hagedorn, *J. Appl. Phys.* **41**, 2491 (1970).
- [42] V. Alexandrakis, D. Niarchos, K. Mergia, Jehyun Lee, J. Fidler, and I. Panagiotopoulos, *J. Appl. Phys.* **107**, 013903 (2010).
- [43] B. D. Cullity and S. R. Stock, Elements of X-Ray Diffraction (3rd Edition), 123 (2001).
- [44] D. Goll and A. Breitling, *Appl. Phys. Lett.* **94**, 052502 (2009).
- [45] V. Lomakin, R. Choi, B. Livshitz, S. Li, A. Inomata, and H. N. Bertram, *Appl. Phys. Lett.* **92**, 022502 (2008).
- [46] D. Goll and S. Macke, *Appl. Phys. Lett.* **93**, 152512 (2008).
- [47] Y. K. Takahashi, K. Hono, S. Okamoto, and O. Kitakami, *J. Appl. Phys.* **100**, 074305 (2006).
- [48] D. Goll, A. Breitling, L. Gu, P. A. van Aken, and W. Sigle, *J. Appl. Phys.* **104**, 083903 (2008).
- [49] C. L. Zha, R. K. Dumas, Y. Y. Fang, V. Bonanni, J. Nogues, and J. Akerman, *Appl. Phys. Lett.* **97**, 182504 (2010).
- [50] D. C. Crew, P. G. McCormick, R. Street, *J. Appl. Phys.* **86**, 3278 (1999).
- [51] J. Lyubina, I. Opahle, K. H. Müller, O. Gutfleisch, M. Richter, M. Wolf, *et al.*, *J. Phys.: Condens. Matter* **17**, 4157 (2005).

- 
- [52] B. J. Kirby, J. E. Davis, K. Liu, S. M. Watson, G. T. Zimanyi, R. D. Shull, P. A. Kienzle, and J. A. Borchers, *Phys. Rev. B* **81**, 100405 (2010).
- [53] V. Alexandrakis, Th. Speliotis, E. Manios, D. Niarchos, J. Fidler, J. Lee, and G. Varvaro, *J. Appl. Phys.* **109**, 07B729 (2011).
- [54] F. T. Yuan, Y. H. Lin, J. K. Mei, J. H. Hsu, and P. C. Kuo, *J. Appl. Phys.* **111**, 07B715 (2012).
- [55] B. J. Kirby, S. M. Watson, J. E. Davies, G. T. Zimanyi, Kai Liu, R. D. Shull, and J. A. Borchers, *J. Appl. Phys.* **105**, 07C929 (2009).
- [56] S. Okamoto, N. Kikuchi, O. Kitakami, T. Miyazaki, and Y. Shimada, *Phys. Rev. B* **66**, 024413 (2002).
- [57] H. Sato, T. Shimatsu, Y. Okazaki, H. Muraoka, H. Aoi, S. Okamoto, and O. Kitakami, *J. Appl. Phys.* **103**, 07E114 (2008).
- [58] Yi-Hung Lin, Jen-Hwa Hsu, Fu-Te Yuan, P. C. Kuo, and J. K. Mei, *IEEE Trans. Magn.* **49**, 3679 (2013).
- [59] V. Lomakin, R. Choi, B. Livshitz, S. Li, A. Inomata, and H. N. Bettram, *Appl. Phys. Lett.* **92**, 022502 (2008).
- [60] F. Casoli, F. Albertini, L. Nasi, S. Fabbrici, R. Cabassi, F. Bolzoni, C. Bocchi, P. Luches, *Acta Mater.* **58**, 3594 (2010).
- [61] M. P. Sharrock, *J. Appl. Phys.* **76**, 6413 (1994).

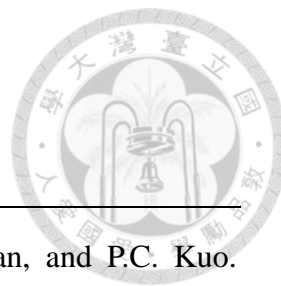
- 
- [62] Z. S. Shan, Yingfan Xu, J. P. Wang, T. C. Chong, S. S. Malhotra, D. C. Stafford, and C. X. Zhu, *IEEE Trans. Magn.* **37**, 1944 (2001).
- [63] S. H. Charap, P.-L. Lu, and Y. He, *IEEE Trans. Magn.* **33**, 978 (1997).
- [64] Erol Girt, A. Yu. Dobin, Bogdan Valcu, H. J. Richter, X. Wu, and Tomas P. Nolan, *IEEE Trans. Magn.* **43**, 2166 (2007).

Publication List



Publications—Journal Articles (Published from Conference Proceedings)

- [1] Y.H. Lin, J.H. Hsu, F.T. Yuan, P.C. Kuo, and J.K. Mei. Microstructure and magnetic performance of perpendicularly magnetic anisotropic $\text{Fe}_3\text{Pt}/\text{Fe}_2\text{Pt}/\text{L}_{10}\text{-FePt}(001)/\text{MgO}(002)$ graded films. *IEEE Transactions on magnetics*, 49, 3679 (2013).
- [2] F.T. Yuan, J.H. Hsu, Y.H. Lin, S.N. Hsiao, and H.Y. Lee. Structural studies of high-Ku metastable CoPt thin films with long-range order. *Journal of Applied Physics*, 111, 07A303 (2012).
- [3] F.T. Yuan, Y.H. Lin, J.K. Mei, J.H. Hsu, and P.C. Kuo. Structure and magnetic properties of FePt(001) graded films deposited on glass substrates. *Journal of Applied Physics*, 111, 07B715 (2012).
- [4] F.T. Yuan, Y.H. Lin, J.K. Mei, J.H. Hsu, and P.C. Kuo. Effect of thickness of MgO, Co-Fe-B, and Ta layers on perpendicular magnetic anisotropy of $[\text{Ta}/\text{Co}_{60}\text{Fe}_{20}\text{B}_{20}/\text{MgO}]_5$ multilayered films. *Journal of Applied Physics*, 111, 07C111 (2012).
- [5] A.C. Sun, F.T. Yuan, J.H. Hsu, Y.H. Lin, and P.C. Kuo. Magnetic Reversal Behaviors of Perpendicular Exchange-Coupled Fe/FePt Bilayer Films. *IEEE Transactions on magnetics*, 45, 2709 (2009).

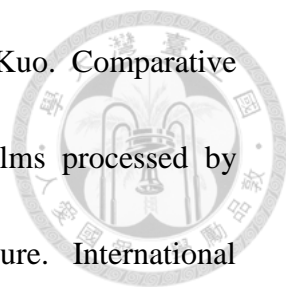


Publications—Journal Articles (Refereed)

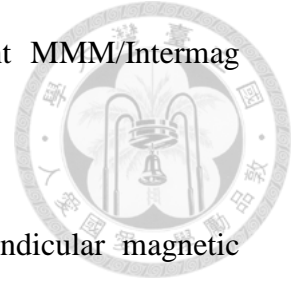
- [1] Y.H. Lin, J.H. Hsu, A.C. Sun, C.F. Huang, P. Saravanan, and P.C. Kuo. Investigation on graded $L1_0$ -FePt(001) magnetic media grown with gradient working pressure. (ready to submit)
- [2] F.T. Yuan, J.H. Hsu, Y.H. Lin, S.N. Hsiao, H.Y. Lee. Study on lattice symmetry of sputtered Co-Cu-Pt metastable ordered thin films. *Journal of Alloys and Compounds*, 530, 18 (2012).
- [3] G.P. Lin, P.C. Kuo, K.T. Huang, C.L. Shen, T.L. Tsai, Y.H. Lin, and M.S. Wu. Self-assembled nano-size FePt islands for ultra-high density magnetic recording media. *Thin Solid Films*, 518, 2167 (2010).
- [4] H.I. Hsiang, L.T. Mei, and Y.H. Lin. Formation and growth of manganese phosphate passivation layers for NTC ceramics. *Journal of Alloys and Compounds*, 484, 723 (2009).

Publications—Conferences Proceedings & Abstracts

- [1] Y.H. Lin, J.H. Hsu, and P.C. Kuo. Comparison between three methods to realize perpendicular graded anisotropy of $L1_0$ -FePt films. Taiwan Association for Magnetic Technology (2014).

- 
- [2] Y.H. Lin, J.H. Hsu, A.C. Sun, C.F. Huang, and P.C. Kuo. Comparative studies on perpendicular graded anisotropy $L1_0$ -FePt Films processed by gradient temperature, composition and working pressure. International Magnetism Conference (2014).
- [3] Y.H. Lin, P. Saravanan, P.C. Kuo, and J.H. Hsu. On the magnetic performance of vertically graded anisotropy $L1_0$ -FePt films processed by gradient temperature, composition and working pressure. Magnetism and Magnetic Materials Conference (2013).
- [4] Y.H. Lin, J.H. Hsu, P. Saravanan, and P.C. Kuo. Investigation on graded $L1_0$ -FePt(001) magnetic media grown by graded working pressures. Magnetism and Magnetic Materials Conference (2013).
- [5] J.H. Hsu, Y.H. Lin, and P.C. Kuo. Approaches to realize (001) FePt graded media. International Symposium on Advanced Magnetic Materials and Applications (2013).
- [6] Y.H. Lin, P.C. Kuo, and J.H. Hsu. Anisotropy-graded $L1_0$ FePt(001) magnetic film obtained by graded working pressures. International Symposium on Advanced Magnetic Materials and Applications (2013).
- [7] Y.H. Lin, J.H. Hsu, F.T. Yuan, P.C. Kuo, and J.K. Mei. Microstructure and magnetic performance of perpendicularly magnetic anisotropic

Fe₃Pt/Fe₂Pt/L₁₀-FePt(001)/MgO(001) graded films. Joint MMM/Intermag Conference (2013).



[8] J.H. Hsu, Y.H. Lin, P.C. Kuo, and F.T. Yuan. Perpendicular magnetic anisotropic FePt graded film. International Conference of AUMS (2012).

[9] F.T. Yuan, Y.H. Lin, J.H. Hsu, J.K. Mei, and P.C. Kuo. Effect of layer thickness (MgO and Ta) on perpendicular magnetic anisotropy of [Ta/Co₆₀Fe₂₀B₂₀/MgO]₅ multilayer films. Magnetism and Magnetic Materials Conference (2011).

[10] F.T. Yuan, J.H. Hsu, Y.H. Lin, P.C. Kuo, and J.K. Mei. Magnetic studies of FePt(001) films with graded anisotropy deposited on glass substrates. Magnetism and Magnetic Materials Conference (2011).

[11] F.T. Yuan, Y.H. Lin, J.H. Hsu, J.K. Mei, and P.C. Kuo. Ordering of thin FePt films assisted by Ar low energy ion-bombardment. Magnetism and Magnetic Materials Conference (2011).

[12] Y.H. Lin, F.T. Yuan, J.H. Hsu, and P.C. Kuo. Effect of Ta and MgO layer thickness on perpendicular magnetic anisotropy of [Ta/Co₆₀Fe₂₀B₂₀/MgO]₅ multilayer films. Taiwan Association for Magnetic Technology (2011).

[13] S.W. Wang, A.C. Sun, Y.H. Lin, J.H. Hsu, P.C. Kuo. Investigatng the influence of sputtering parameters on the formation of CoPt (001) thin films.

Taiwan Association for Magnetic Technology (2009).

